Field Pilot Injection Strategies for CO_2 Foam EOR in a Layered Heterogeneous Carbonate Reservoir

Master Thesis in Reservoir Physics

by

Stine Marie Kristiansen

June 2018

Abstract

Injection of CO_2 foam for enhanced oil recovery (EOR) may provide economic incentives for large-scale industrial CO_2 storage. An international field pilot research program has been initiated to develop and test CO_2 foam systems with mobility control in a heterogeneous carbonate reservoir. Supported by industry and the Norwegian Research Council, a university lead field pilot project applies experimental and numerical efforts to investigate how to improve CO_2 sweep efficiency by foam to enhance the oil recovery and store the injected CO_2 in the reservoir.

This Thesis evaluates foam injection strategies in an inverted 5-spot well pattern to achieve mobility control and increase areal CO_2 sweep efficiency. In a simulation effort, using established models on field pilot geology and foam, Surfactant-Alternating-Gas (SAG) injections are compared to pure CO_2 injection and Water-Alternating-Gas (WAG) to quantify foam performance.

Initially, 11 injection strategies are compared through static performance indicators like cumulative oil production, gas-oil-ratio (GOR), degree of CO_2 recycling and the CO_2 utilization factor. The most favorable strategies are further analyzed through streamline simulation, CO_2 sweep patterns, dynamic gas saturation profiles and quantification of sweep efficiency.

SAG is the optimal injection strategy in terms of CO_2 utilization factor for oil recovery when compared with WAG and CO_2 injection for performance indicators such as reduced GOR, delayed gas breakthrough and reduced CO_2 recycling. SAG also produces more oil at equal pore volumes injected due to reduced CO_2 mobility and increased sweep efficiency.

Three high-permeability layers were identified as thief zones for CO_2 flow through simulation and quantification of CO_2 sweep patterns. Foam generation in high-permeability layers during SAG injection diverted chase water to surrounding flow zones of lower permeability and increased sweep efficiency.

Acknowledgements

I owe a huge gratitude to many people for the help and support during the work of this Thesis.

First, I would like to express my sincere gratitude to my supervisor, Prof. Martin A. Fernø, for the support, guidance and valuable discussions throughout the work of this Thesis. I would also like to thank Associate Prof. Arne Graue for giving me the opportunity to visit the East Seminole Field in Texas, as part of the research project that this Thesis concerns.

I would also like to thank PhD candidates Sunniva B. Fredriksen and Arthur U. Rognmo for your knowledge and discussions. A special acknowledgement goes to PhD candidates Zachary P. Alcorn and Mohan Sharma for providing me the baseline simulation model and valuable information related to the research project. I am sincerely grateful for your patience and discussions. I would also like to thank PhD candidate Tore Føyen, for you knowledge, advice and for always being the good traveling companion that you are.

I would like to thank my fellow master students at Reservoir Physics and Reservoir Chemistry, and of course the very special "PTEK-jentene", that I hope join forces as reservoir engineers in Stavanger someday. I must also thank "The office", and especially Eldri Bratland Skjelsvik. Thank you for our friendship and for all the adventures that we share from the last five years.

Finally, I owe my deepest gratitude to my parents, Lise and Steinar Kristiansen, and my boyfriend, Tobias Tømmerås, for their uplifting mood and great support.

Bergen, June 2018

Stine Marie Kristiansen

Contents

List of Figures

List of Tables

Abbreviations

API	**A**merican **P**etroleum **I**nstitute
atm	**atm**ospheric
bbl	oil barrels
BHP	**B**ottom **H**ole **P**ressure
BPP	**B**ubble **P**oint **P**ressure
CBP	**C**entral **B**asin **P**latform
CCS	**C**arbon **C**apture and **S**equestration
CCUS	**C**arbon **C**apture **U**tilization and **S**equestration
CIERO	**C**entre for **I**nternational **R**esearch **O**slo
CO_2	**C**arbon Dioxide
cP	**c**enti **P**oise
D	**D**arcy
EOR	**E**nhanced **O**il **R**ecovery
EoS	**E**quation **o**f **S**tate
FAWAG	**F**oam **A**ssisted **W**ater-**A**lternating-**G**as
ft	**F**eet
GOR	**G**as-**O**il-**R**atio
GR	**G**amma **R**ay
HCPV	Hydro Carbon Pore Volume
IEA	**I**nternational **E**nergy **A**gency
IFT	**I**nterfacial **T**ension
mD	**m**illi **D**arcy
M	thousand
MM	million
MMP	**M**inimum **M**iscibility **P**ressure
MPC	**M**odified **B**rooks- **C**orey model
MPZ	**M**ain **P**ay **Z**one
NTNU	Norwegian University of Science and Technology
MRF	**M**obility **R**eduction **F**actor
OOIP	**O**riginal **O**il **I**n **P**lace
OWC	**O**il **W**ater **C**ontact
PHIE	**E**ffective **P**orosity
ppm	**p**arts **p**er **m**illion

psia	**P**ounds per **S**quare **I**nch **A**bsolute
PV	**P**ore **V**olume
PVI	**P**ore **V**olume **I**njected
RB	**R**eservoir **B**arrels
ROZ	**R**esidual **O**il **Z**one
ROS	**R**emaining **O**il **S**aturation
SAG	**S**urfactant-**A**lternating-**G**as
SCF	**S**tandard **C**ubic **F**eet
STB	**S**tock **T**ank **B**arrels
Surfactant	Surface active agents
TOF	**T**ime **O**f **F**light
TREFLE	Institute of Mechanics and Engineering in Bordeaux
WAG	**W**ater-**A**lternating-**G**as

Nomenclature

C_f	Foam surfactant concentration
C_f^a	Adsorbed foam surfactant concentration
C_s	Effective surfactant concentration
C_sr	Reference surfactant concentration
E_A	Areal sweep efficiency
E_D	Microscopic displacement efficiency
E_R	Recovery efficiency
E_V	Vertical sweep efficiency
E_{vol}	Volumetric sweep efficiency%
K	Absolute permeability
K_e	Effective permeability
k_r	Relative permeability
$k_{rg,cl}$	Relative permeability of gas at critical liquid saturation
$k_{rog,cg}$	Relative permeability of oil at critical gas saturation
$k_{row,cw}$	Relative permeability of oil at critical water saturation
$k_{rw,iro}$	Relative permeability for water at residual oil saturation
$M_{g,o}$	Mobility ratio between oil and gas
M_r	Reference mobility reduction factor
M_{rf}	Gas mobility reduction factor
N	Original Oil In Place
N_c	Capillary number
N_{c^r}	Reference capillary number
N_p	Oil produced
Q	Volumetric flow rate
R_s	Solution gas-oil-ration
R_v	Vaporized oil-gas-ratio
S_o	Oil saturation
S_g	Gas saturation
S_{gc}	Critical gas saturation
$S_{g,con}$	Connate gas saturation
$S_{o,irg}$	Oil saturation at irreducible gas saturation
$S_{o,irw}$	Oil saturation at irreducible water saturation
S_{om}	Residual oil saturation

S_{org}	Residual oil saturation after gas flood
S_{orw}	Residual oil saturation after water flood
S_w	Water saturation
S_{wc}	Critical water saturation
$S_{wc,con}$	Connate water saturation
UF_{CO2}	CO_2 utilization factor

ϕ	Porosity
λ	Mobility
μ	Viscosity
μ_{app}	Apparent viscosity
ρ	Fluid density
β_g	Gas volume factor
β_o	Oil volume factor

Part I

Introduction and Theory

1. Introduction

To mitigate global warming and regulation policies, carbon capture and sequestration (CCS) was developed in 1989 for carbon emissions mitigation (Saulnier and Varella, 2013). CCS refers to the capture, transport and storage of carbon, typically in the form of carbon dioxide (CO_2), where carbon is injected and stored in deep subsurface saline formations or depleted hydrocarbon reservoirs (Pham and Halland, 2016). Currently, there is a large number of global CCS projects with promising results (IPPC, 2014). However, based on a recent report from the International Energy Agency (IEA), the capacity for CCS must tenfold in order to reach the climate Paris agreement of a two degree scenario before 2025 (OECD/IEA, 2017). The report from IEA also emphasize on the importance of an expanding focus on CCS in long-term climate strategies and targeted support on project development to get on the trajectory to meet the climate goal.

Some of the greatest challenges with CCS are the high costs related to capture, compression and cleaning of CO_2 prior to storage (Irlam, 2017). In a report from the Global CCS Institute from 2017, the costs of CCS plants were estimated to be between 50-200 US$/MWh (Irlam, 2017). In an interview with the Norwegian magazine "Energi og Klima" this year, the senior researcher of the Centre for International Climate and Environmental Research Oslo (CIERO), Glen Peters, expressed his concern for the expensive cost of CCS, especially during up-scaling of CCS (Ursin, 2018). In Peters opinion, the technology must be developed further to gain efficiency and save costs. In an attempt to achieve economic success with CO_2 storage, several countries with access to anthropogenic CO_2 has combined storage of carbon with oil and gas recovery (Pham and Halland, 2016).

CO_2 flooding is a frequently used enhanced oil recovery (CO_2 EOR) method that increase the recovery of oil by 5-20%, while a great portion of CO_2 remains in place of the depleted reservoir (Enick and Olsen, 2012). Carbon utilization for oil recovery, expands the process of CCS to carbon capture, utilization and sequestration (CCUS), which boost the profit of carbon storage (Dai et al., 2017). With over 40 years of American practice in onshore CO_2 EOR and nearly 20 years of Norwegian experience within CO_2 storage in geological formations, the two nations have initiated a collaboration on CCUS with CO_2 EOR (Alcorn et al., 2016). The project involves an onshore field pilot in Texas, with the aim of developing and testing CO_2-foam systems with mobility control at laboratory and field scale to optimize CO_2 integrated EOR and deposition. With focus on improving the CO_2 sweep efficiency, foam is expected to control the mobility of CO_2. Based on laboratory results, the predicted performance of foam for CO_2 EOR and storage, is up-scaled from core scale to field scale, through numerical simulation. The objective of this Thesis is to evaluate the CO_2 foam performance in a heterogeneous carbonate system by numerical simulation.

2. East Seminole Field Pilot Project

2.1 Project Background

Collaborative CCUS research program was initiated in 2015 and is lead by the Dept. of Physics and Technology at the University of Bergen (Alcorn et al., 2016). The aim is to test CO_2-foam for mobility control to optimize CO_2 integrated EOR and deposition. Collaborating partners are Rice University, Texas A&M University, Stanford University, University of Texas at Austin, Imperial College London, the Institute of Mechanics and Engineering in Bordeaux (TREFLE), University of Kansas, New Mexico Institute of Mining and Technology, Delft University of Technology, Norwegian University of Science and Technology (NTNU), University of Bergen, Shell E&P, TOTAL E&P, Statoil ASA, Schlumberger and field operators Tabula Rasa Energy. The project involves analyzing of foam performance on CO_2-EOR and storage through up-scaling of laboratory results to field scale, including an inexpensive onshore field pilot in the East Seminole field in Texas. Currently, the field pilot approaches the stadium of foam implementation. The field pilot preparation work has been assigned to different research institutions and universities, to assist in the design of foam and drainage strategy. The University of Bergen has been responsible for laboratory up-scaling and visualization of EOR by foam.

The specific aim of this project is to generate a moderate foam for CO_2 mobility control to assess the field performance of CO_2 mobility control foam. Improved field performance by foam is verified through four main characteristics:

- Incremental oil production through improved sweep efficiency
- Reduced gas-oil-ratio (GOR)
- Reduced CO_2 recycling
- Mobility control verification through monitoring of pilot wells and injected fluids

In addition to the characteristics mentioned above, the performance of foam is also evaluated in terms of a CO_2 utilization factor (UF_{CO2}), which is commonly used for evaluation of field projects (Kulkarni and Rao, 2004). The CO_2 utilization factor is defined as the CO_2 volume injected under standard conditions, to produce a barrel of oil:

$$UF_{CO_2} = \frac{\text{injected volume of } CO_2}{\text{produced volume of oil}} \tag{2.1}$$

2.2 Pilot Area and Field History

The study area for the field pilot is situated in the East Seminole Field in West Texas (Alcorn et al., 2017). One of the main attributes for selection was the already existing infrastructure for CO_2 distribution. The field consists of two units that are schematically illustrated in Figure 2.1, with their respective timeline of recovery strategy. After production started in 1960, the San Andres field has been introduced to pressure depletion, water flooding, infill drilling and CO_2 flooding. The Lindoss Unit started its primary recovery in 1981, before water flooding and a subsequent CO_2 flooding occurred. The CO_2 injection strategy was initiated in inverted 40 acre 5-spot patterns, limited to the eastern part of the Field. (Gray, 1989)

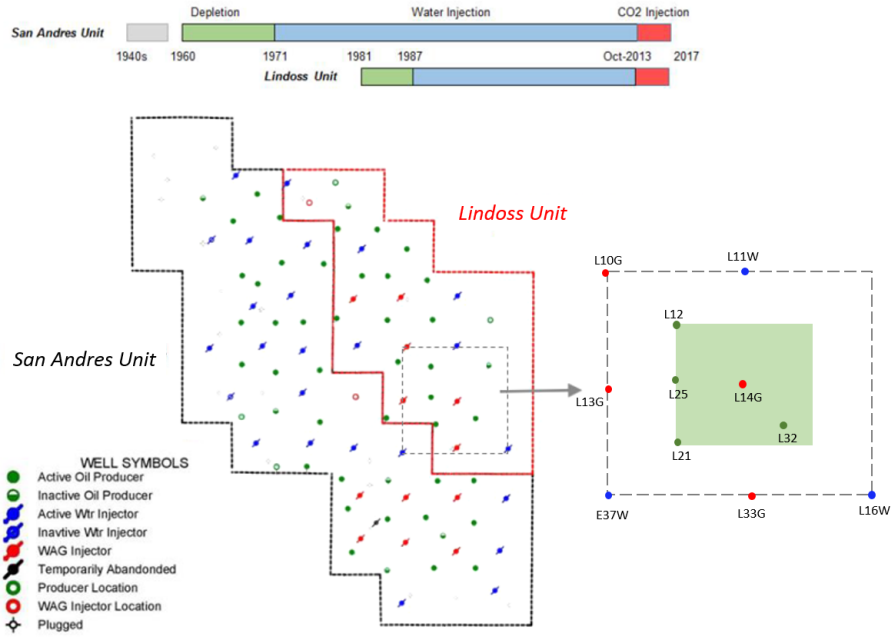

FIGURE 2.1: Well map of selected pilot pattern (green shaded area) and peripheral injection wells, and recovery time line for the field (Alcorn et al., 2017).

During CO_2 flooding, peripheral production wells experienced a rapid breakthrough of CO_2, a high gas-oil-ratio (GOR) and CO_2 channeling (Alcorn et al., 2017). The CO_2 flood most likely suffer due to high CO_2 mobility compared to oil, and large reservoir heterogeneity. These characteristics make the East Seminole Field a promising candidate for CO_2 foam injection, in addition to the advantage of an already existing infrastructure for CO_2 distribution. The foam is expected to improve the recovery performance by diverting flow from high permeability, well swept regions to low permeability, unswept regions. Based on well arrangement, continuity of reservoir flow zones and production history, the green shaded area in Figure 2.1 was selected as the field pilot pattern (Alcorn et al., 2016).

2.3 Geological Setting

The East Seminole Field is located on the northeastern Central Basin Platform (CBP) of the Permian Basin in West Texas, shown in figure 2.2.

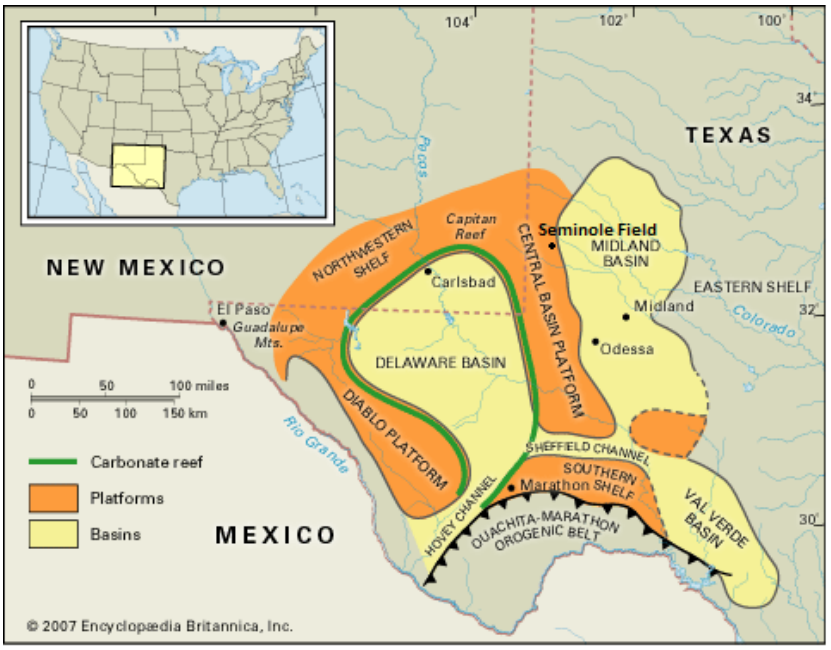

FIGURE 2.2: Structural map of the sub-basins, reefs and platforms of the Permian Basin in West Texas and the location of the Seminole Field (Tang, 2015).

The Field produces from one of the most prolific conventional plays of carbonate character in the Permian Basin; the San Andres formation, illustrated in Figure 2.3 (Alimahomed et al., 2018). San Andres is composed of mudstones, wackestones, packstones, grainstones and dolostones, with a mineralogy consisting of mainly dolomite minerals, moderate amount of anhydrite and occasional stylolites (Honarpou et al., 2010). Depositions origin from uplifting and erosion of the CBP during the Guadalupian epoch of the middle Permian period. Periodic floods have developed a cyclical deposition environment with high quality reservoir intervals and shaley mudstone layers (Alcorn et al., 2016).

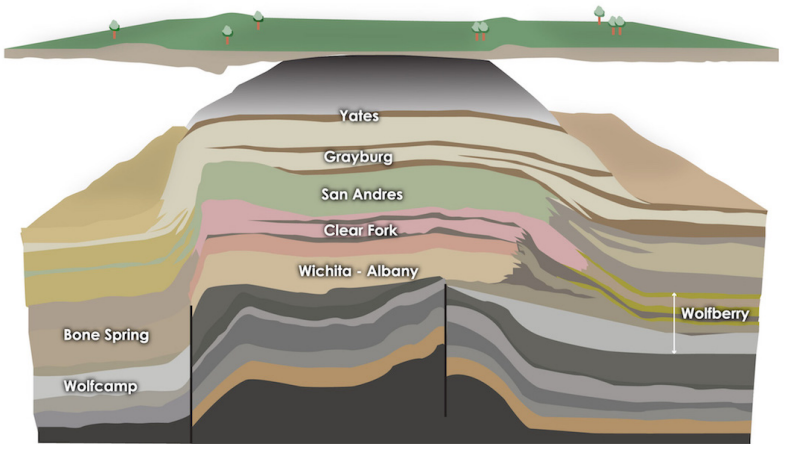

FIGURE 2.3: The San Andres formation and other platform carbonates in the Central Basin Platform Stratigraphy (Camber Energy, 2018).

2.4 Reservoir Characterization

The reservoir characterization builds upon petrophysical analysis and interpretation of well logs, core data and production data (Alcorn et al., 2016). The cyclical sequence of porous, grain dominated units and less porous, mud dominated intervals, is shown in the petrophysical logs for the selected well pair of the Field pilot, see Figure 2.4. The cyclical deposition of intertidal to subtidal facies, has developed a heterogeneous, multi-layered carbonate system with a high range of horizontal and vertical porosity and permeability (Honarpou et al., 2010).

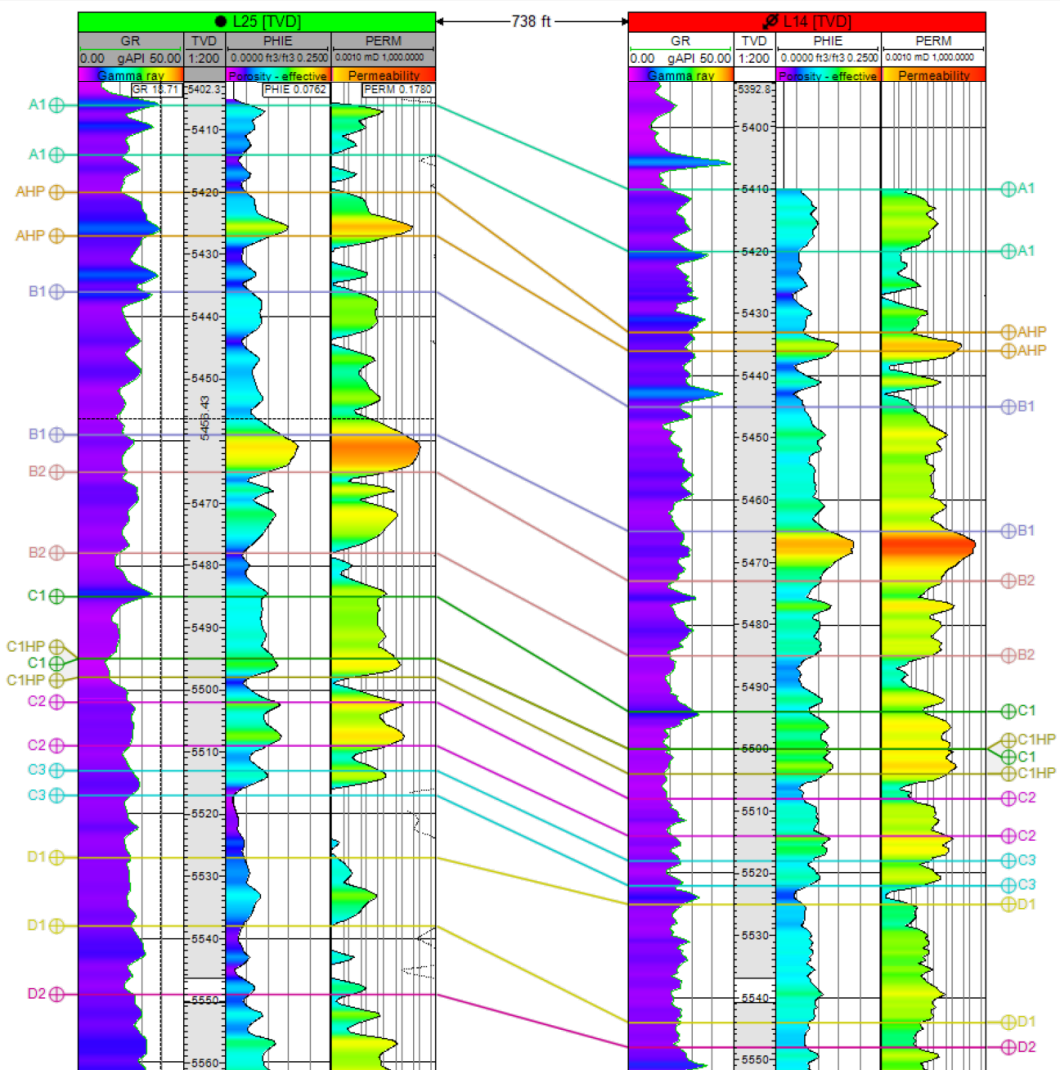

FIGURE 2.4: Petrophysical logs with gamma ray (GR), effective porosity (PHIE) and permeability (PERM) for production well L25 and injection well L14G. The initial flow zone division and correlation between the well pair is also demonstrated (Alcorn, 2017).

Reservoir characteristics and fluid properties are summarized in Table 2.1. Wettability measurements indicate a mixed-wet system with a tendency towards oil-wet conditions (Honarpou et al., 2010). This is supported by a theory of existing meteoric water that may have altered the wettability of the rock, through diagenesis.

TABLE 2.1: Reservoir and fluid properties of the San Andres formation (Alcorn et al., 2017).

Parameter	Value
Average Depth	5200 ft
Average Permeability	13 mD (range: 1-300mD)
Average Porosity	12-15% (range: 3-28%)
Pay Thickness	110 ft
Reservoir Temperature	105° F
Initial Reservoir Pressure (hydrostatic)	2500 psia
Current Reservoir Pressure	3200 psia
Bubble Point Pressure	1805 psia
Minimum Miscibility Pressure	1500 psia
Average Formation Brine Salinity	70,000 ppm
Oil Gravity	31° API
Oil Viscosity (reservoir condition)	1.20 cP

The structure of the San Andres dolomite consists of anticlinal traps, elongated northwest-southeast and underlain by a Devonian fault block (Gray, 1989). Due to a presumed tilting event and a breach of seal, the oil zone of the reservoir is divided into a Main Pay Zone (MPZ) and a Residual Oil Zone (ROZ), where the latter is located below the traditional producing oil-water-contact (OWC) (Honarpou et al., 2010). The uncertainty of the geologic origins of the ROZ, makes it difficult to estimate the remaining oil saturation (ROS) in the residual oil zone. Figure 2.5 shows two examples of the fluid system and the ROS in the San Andres reservoir, after an uplift of the basin and after a breach of seal.

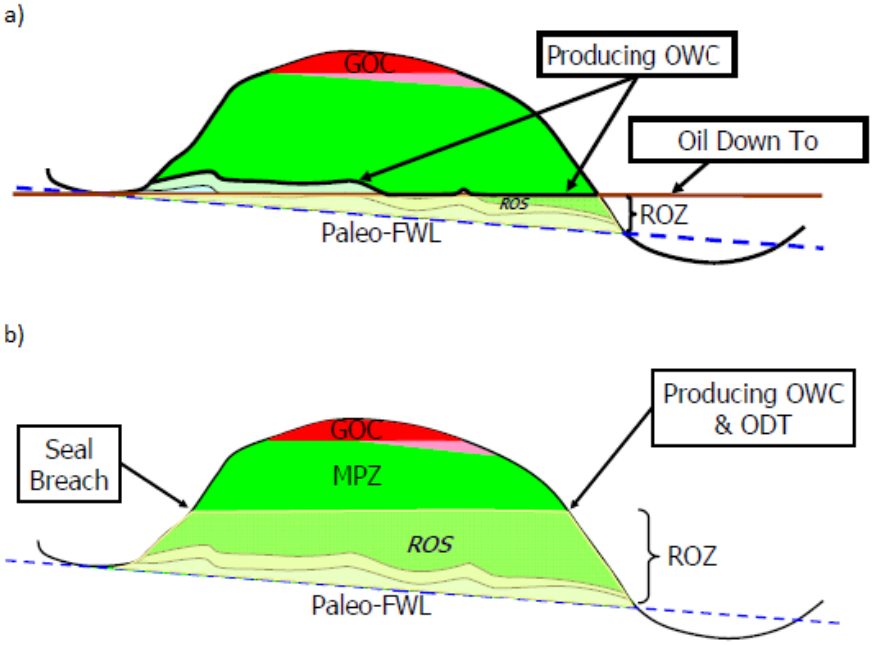

FIGURE 2.5: Representation of the effect of different geologic events on remaining oil saturation; (a) effect of a tilting event, (b) effect of a breach of seal (Honarpou et al., 2010)

While the residual oil saturation in the MPZ has decreased to an average of 25% after water flooding (S_orw) and a subsequent 12% after miscible CO_2 flooding (S_org), the ROZ on the other hand is known to contain a considerable amount of trapped oil (Honarpou et al., 2010). Based on integrated data, the probable average of the remaining oil saturation (ROS) in the ROZ is estimated to lie between 28-32%, after a presumable natural water flood. The trapped oil in the ROZ, is considered to only be technically and economically feasible through tertiary recovery. Figure 2.2, summarize the initial and current saturations in the two reservoir zones.

TABLE 2.2: Initial and current saturations in the MPZ and ROZ (Honarpou et al., 2010).

Saturation	Value
Initial water saturation in MPZ	0.1
Initial water saturation in ROZ	0.68
Average S_{org} in MPZ	0.12
Average S_{orw} in MPZ	0.25
Average oil saturation in ROZ	0.28-0.32

3. CO_2 EOR

In addition to an interest in CO_2-injection for emissions mitigation, there is an interest in CO_2 for enhanced oil recovery (CO_2 EOR). This chapter will demonstrate the advantages and disadvantages of CO_2 EOR.

3.1 CO_2 Properties

Due to a relatively low minimum miscibility pressure (MMP) of CO_2 and a higher fluid density compared to other injection gases, CO_2 often contribute to a higher recovery efficiency of oil. CO_2-EOR may increase the recovery of oil by approximately 5-20% compared to conventional recovery techniques (Enick and Olsen, 2012).

The recovery efficiency for a process is determined by the stock tank barrels (STB) of recovered oil, to the total volume of oil present in the reservoir prior to production. Recovery efficiency (E_R) can also be defined as the microscopic displacement efficiency (E_D) over the volumetric displacement efficiency (E_{vol}):

$$E_R = \frac{N_p}{N} = E_D \cdot E_{vol} \tag{3.1}$$

where N_p represents the oil produced (STB), N is the original oil in place (STB), E_D is the microscopic displacement efficiency and E_{vol} is the volumetric sweep efficiency.

The volumetric sweep efficiency or displacement efficiency can be defined as:

$$E_{vol} = \frac{\text{volume of oil contacted}}{\text{volume of oil in place}} \tag{3.2}$$

The microscopic displacement efficiency is defined as:

$$E_D = \frac{\text{volume of oil displaced}}{\text{volume of oil contacted}} \tag{3.3}$$

E_{vol} can be further divided into the product of vertical sweep efficiency (E_V) and areal sweep efficiency E_A, which are defined below.

$$E_v = \frac{\text{cross-sectional area contacted}}{\text{total cross-sectional area}} \tag{3.4}$$

$$E_A = \frac{\text{area contacted in a pattern}}{\text{total pattern area}} \tag{3.5}$$

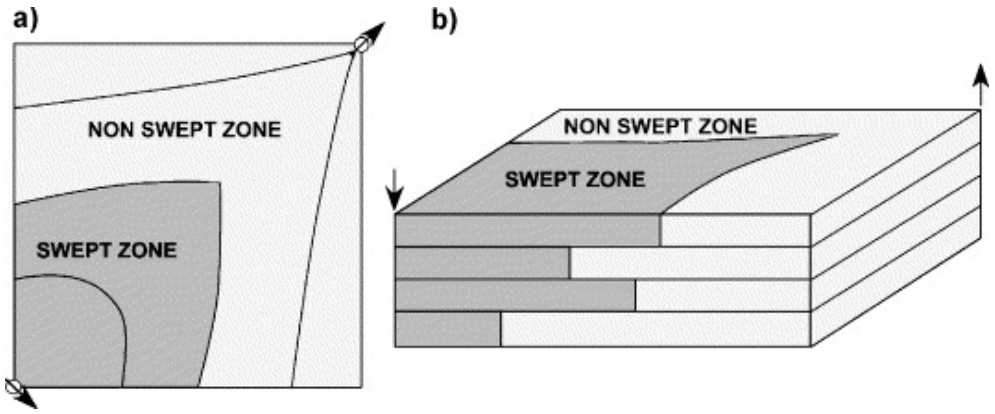

FIGURE 3.1: Schematic representation of the two components of volumetric sweep efficiency: (a) areal sweep; (b) vertical sweep (Martel et al., 2004)

Figure 3.1 illustrates the areal sweep (a) and the vertical sweep efficiency (b) in a layered reservoir. E_V strongly depends on the mobility ratio between the displacing fluid and the displaced fluid, as well as the vertical variations of horizontal permeabilities and the total volume of injected fluid, while E_A depends mainly on the selected well pattern and the mobility ratio. Thus, the volumetric displacement efficiency E_{vol} depends on both the areal and vertical displacement efficiency, it is contingent on the same parameters as the two.

3.1.1 Supercritical CO_2

CO_2 appears as a gaseous phase under atmospheric conditions (15 °C and 1 atm). However, at a relatively low temperature and pressure, the compound attains a supercritical phase. The critical point for this state serves a pressure of 72.81 atm (73.77 bar) and a temperature of 30.98 °C (304.13 Kelvin), which is shown in Figure 3.2. At supercritical state, CO_2 behaves like a gas with the density of a liquid (Dostal et al., 2004). Supercritical, dense CO_2 is favorable to normal gas because the displacement of oil becomes more efficient.

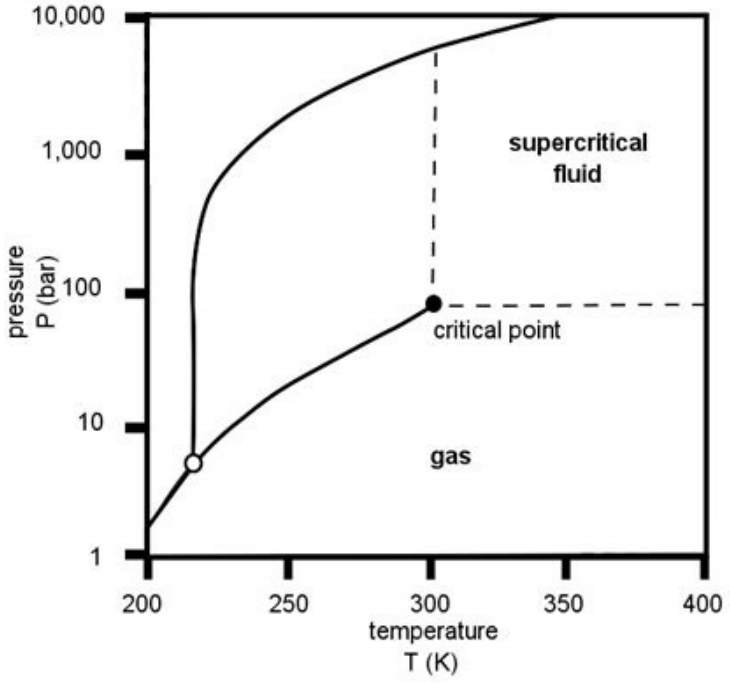

FIGURE 3.2: Pressure and temperature phase diagram for CO_2, with defined phase envelope for supercritical state (Encyclopedia, 2015).

3.1.2 CO_2 Miscibility

In addition to a low boundary point for supercritical behavior, CO_2 also have a relatively low minimum miscibility pressure (MMP) (Rocha et al., 2006). MMP is the lowest pressure at which gas can reach dynamic miscibility with oil at reservoir temperature. At such conditions, the interfacial tension (IFT) between the two phases is significantly reduced or removed completely, which increases the displacement efficiency. Miscibility may increase the recovery factor by up to 18% compared to an immiscible displacement of oil (Kamali et al., 2014). In theory, 100% of the OOIP could potentially be recovered during a miscible displacement. However, there are different phenomena that impede the displacement efficiency of CO_2 flooding.

3.2 CO_2 as a Displacing EOR Fluid

Despite the supercritical density and miscibility, CO_2 flooding still suffer from an unfavourable mobility ratio and a high density contrast between oil and CO_2. This lead to viscous fingering and gravity segregation which is aggravated by reservoir heterogeneity. Ultimately, this lead to a poor sweep efficiency of CO_2 and a modest recovery efficiency potential.

3.2.1 Viscous Fingering

Viscous fingering is a common phenomenon during oil displacement by gas (Martel et al., 2004). This include the development of viscous gas fingers during gas flooding. It occurs due to low gas viscosity compared to the viscosity of oil, which means that the gas has a much higher mobility than oil. The mobility of a fluid is defined as the ratio between the effective permeability of the rock and the viscosity of the fluids. From the definition of effective permeability, the mobility may be expressed as:

$$\lambda_i = \frac{K_{e,i}}{\mu_i} = \frac{K k_{ri}}{\mu_i} \tag{3.6}$$

where λ is the mobility (m^2/Pa·s) of phase i, K_e is the effective permeability (m^2), μ is the viscosity (Pa·s), K is the absolute permeability (Darcy) and k_r is the relative permeability.

For a gas flood, where gas attempts to displace the oil, the mobility ratio can be expressed as follows:

$$M_{g,o} = \frac{\lambda_g}{\lambda_o} = \frac{\left(\frac{k_{r,g}}{\mu_g}\right)}{\left(\frac{k_{r,o}}{\mu_o}\right)} \tag{3.7}$$

where $M_{g,o}$ is the mobility ratio and the prefixes represents gas and oil.

3.2.2 Gravity Segregation

In addition to viscous fingering, gravity segregation is one of the reasons for poor sweep efficiency of gas (Enick and Olsen, 2012). During gas flooding, gravity override will occur as a result of gravity forces and density contrasts between the injected and displaced fluid. Despite the dense nature of supercritical CO_2, the contrast between oil and CO_2 is still affecting the displacement front stability by gravity segregation during CO_2 flooding.

3.2.3 Reservoir Heterogeneity

Reservoir heterogeneity may also influence the sweep efficiency, as it aggravates the effect of gravity override and viscous fingering (Kloet et al., 2009). For multiple-contact miscibility displacements, the gas fronts will often develop instability at locations and in directions that are govern by large permeability variations within the formation (Enick and Olsen, 2012). During viscous fingering, gas establishes preferentially connected pathways, hence in a heterogeneous system, the CO_2 will preferentially sweep high-permeability zones and avoid low-permeability

zones. The high-permeability regions will create channels of gas flow, and lead to rapid gas breakthrough and poor vertical displacement efficiency (Mukherjee et al., 2016).

3.3 CO_2 Mobility Control

The aim for CO_2 mobility control is to attain a more favorable mobility ratio between oil and CO_2, which allows a more stable displacement front to develop. This results in a better sweep efficiency of gas, delay the breakthrough of gas and subsequently lead to higher recovery efficiency and allow storage of more CO_2 in the reservoir. In an attempt to decrease the mobility ratio between oil and CO_2, there are developed different techniques for CO_2 mobility control (Enick and Olsen, 2012). Some of the most successful techniques include a water-alternating-gas (WAG) strategy and foam application. The latter mobility control technique is discussed in detail in the next chapter.

The objective of WAG is to decrease the mobility of gas to a level comparable to that of oil by injecting alternating slugs of water and gas. This improves the near well injectivity and reduces the gas mobility. Specifically, the reduction in gas mobility proceed from the increase in water saturation, and the corresponding decrease in saturation and relative permeability of CO_2. A saturation increase of a wetting phase is described as imbibition, and a decrease in saturation of a wetting phase is described as drainage. For WAG in a water-wet system, imbibition indicates the injection of water, and drainage indicates the injection of gas (Shahverdi et al., 2011). The reduction in CO_2 mobility during imbibition of water, is shown in Figure 3.3.

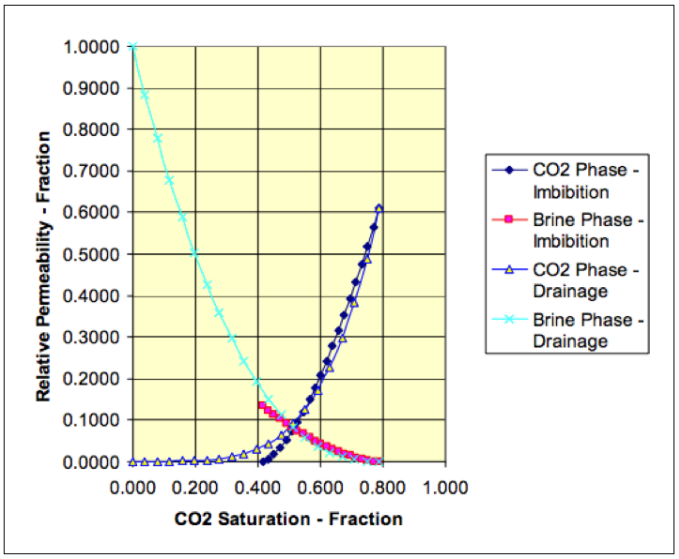

FIGURE 3.3: Relative permeability curve of a CO_2-brine system at reservoir conditions for a water-wet Winniepegosis carbonate core sample. The relative permeability curve shows a rapid decrease in CO_2 relative permeability during brine phase imbibition and CO_2 phase drainage (Bennion and Bachu, 2010).

4. Foam for Mobility Control

4.1 Foam in Porous Media

In addition to WAG, there is an immense body of research on the application of foam for CO_2 mobility control and EOR (Enick and Olsen, 2012). With its ability to reduce the relative permeability of CO_2, and simultaneously increase the apparent viscosity of foam, the chemical application is one of the most promising investigated techniques for CO_2 mobility control. The foam system consists of dispersed gas, discontinuously separated by a continuous water film, called lamellae (Enick and Olsen, 2012). This is shown in Figure 4.1, illustrating a schematic representation of foam. A stabilizing agent, usually in the form of surfactants, is introduced to prevent immediate rupture of the lamellae (Schramm and Wassmuth, 1994). The physics behind gas mobility reduction by foam is linked to lamellae generation and gas discontinuity (Zanganeh and Rossen, 2013). The lamellae blocks the flow channels for gas and causes it to be discontinuous and captured in foam bubbles. Additionally, the mobility is reduced by an increased apparent viscosity resulted by gas disruption and impediment from drag forces, viscous and capillary forces and a surface-tension gradient (Enick and Olsen, 2012).

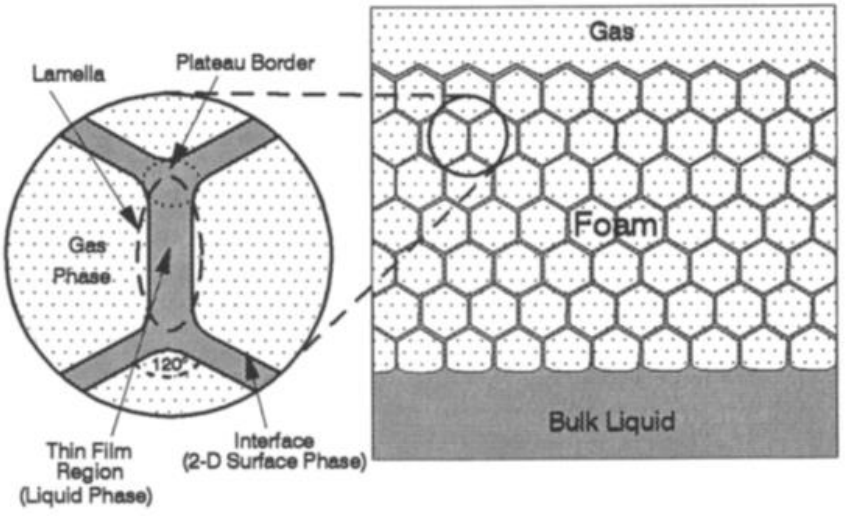

FIGURE 4.1: Schematic representation of a two-dimensional foam system (Schramm and Wassmuth, 1994).

4.2 Sweep Efficiency by Foam

In heterogeneous reservoirs, foam is primarily formed in high-permeability regions, because they are preferentially swept by CO_2 and the presence of CO_2 contribute to rapid foam generation. As the foam reduces the relative permeability of CO_2 in these zones, the CO_2 is gradually diverted to unswept zones of lower permeability and higher oil saturation. This has a detrimental effect on viscous fingering and gravity segregation and a positive impact on the vertical and areal

sweep efficiency. Consequently, the recovery of oil may increase, while the producing GOR decrease. Additional benefits of the CO_2-foam EOR technology, are the treatment reversibility and absence of permanent impact on rock permeability (Mukherjee et al., 2016). Figure 4.2 and 4.3 schematically illustrate the effect of CO_2-foam EOR on vertical and areal sweep efficiency.

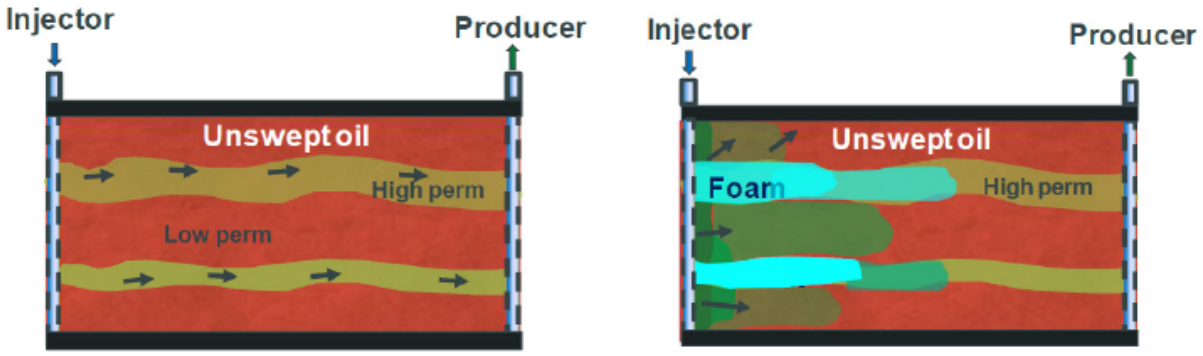

FIGURE 4.2: Effect of CO_2-foam on viscous fingering and sweep efficiency, as the foam diverts CO_2 (green color) from high permeability regions to low permeability regions (Sheng, 2013).

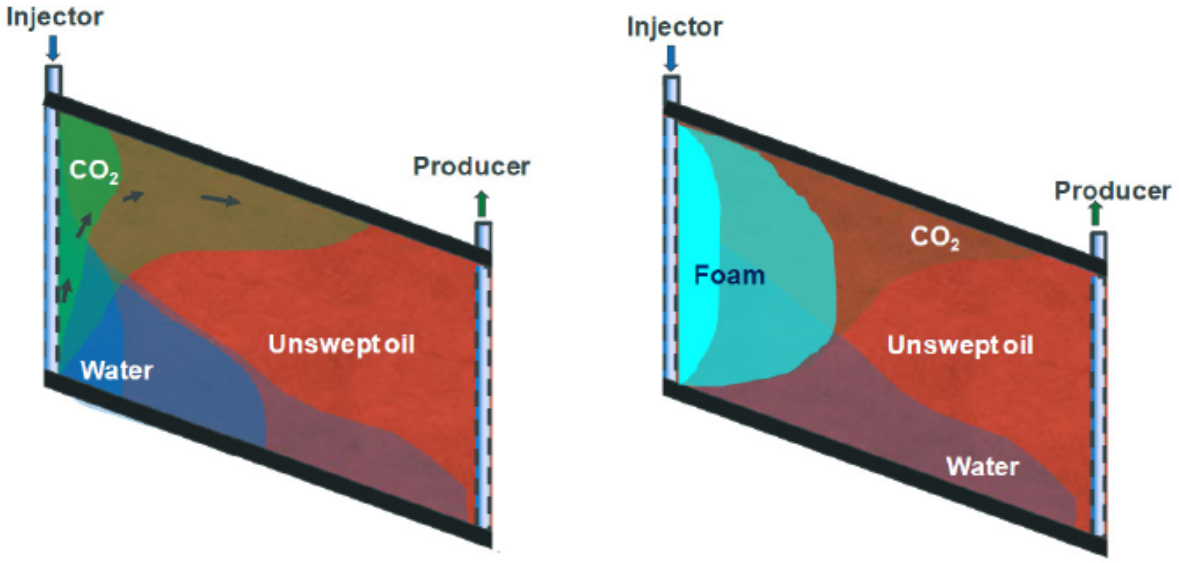

FIGURE 4.3: Effect of CO_2-foam on gravity segregation, as the foam blocks the upward movement of CO_2 (green) and improves the sweep efficiency (Sheng, 2013).

The efficiency of foam may be assessed by a gas mobility reduction factor (MRF) (Chang and Grigg, 1999). Essentially, the factor represents the magnitude of reduction in gas mobility due to foam. It can be defined as the mobility of CO_2 with foam over the mobility of pure CO_2 prior to foam application:

$$MRF = \frac{\lambda_{CO_2 foam}}{\lambda_{CO_2}} \tag{4.1}$$

where $\lambda_{CO2,foam}$ is the mobility of CO_2-foam and λ_{CO2} is the mobility of pure CO_2 before foam is generated.

4.3 Types of Foam

In field application, there are two types of foam; conformance control foam and mobility control foam (Enick and Olsen, 2012). While the former foam type intends to reduce reservoir heterogeneities in the near well bore region, the latter aims to function in depth of the formation. What essentially separates the two foam designs, is the foam strength and efficiency. A conformance control foam is typically strong and effective in order to reduce the mobility of gas significantly over a short distance. Whereas the mobility control foam should not be excessively strong; it must be strong enough to maintain long-term stability, yet weak enough to have a sufficient mobility in order to propagate. This is an ambitious approach and one of the reasons why conformance control field pilots are more prevalent than mobility control field pilots.

4.4 Foam Injection Strategies

Injection strategies for foam generation include co-injection and Surfactant-Alternating-Gas (SAG) (Ren and Nguyen, 2017). The former includes a simultaneous injection of surfactant solution with gas, whereas the latter includes an injection of alternating slugs of surfactant solution and gas. Essentially, SAG represents a foam assisted WAG (FAWAG), where a surfactant is added to a water injection slug and foam is generated during a subsequent gas injection slug. The injection strategy for foam generation either involves a constant surface injection pressure or a constant injection well rate (Norris et al., 2014). If the surfactant solution and gas is injected at a constant injection pressure, generation of foam is often indicated by a reduced injection well rate as a result of gas mobility reduction. If the surfactant solution and gas is injected at a constant injection rate on the other hand, foam generation may be demonstrated by an increase in the injection pressure.

4.5 Foam Characteristics

In order to achieve the desired effect of foam, an appropriate foam design is important (Schramm and Wassmuth, 1994). As mentioned previously, a mobility control foam aims to function in depth of the reservoir, which requires a long-term foam stability without being excessively strong. Hence, the foam design requires a modest concentration of surfactant that allows the foam to be injected for a long time, until the desired mobility ratio is achieved. The degree of stability and mobility reduction depend on several artifacts. Among the most influential factors, are surfactant type, surfactant concentration, foam quality, oil saturation and flow rate (Enick and Olsen, 2012). The effect of these parameters on foam performance will be elaborated further in this section.

4.5.1 Types of surfactant

A foaming agent is one of the most important criteria to form and maintain foam, and is therefore critical for the foam design. Surfactants are one of the most prevalent foaming agents based on their amphilic compound, which allows them to accumulate at the interface of water and gas. They increase foam stability by replacing high energetic bulk molecules and reducing the interfacial tension (Mulligan, 2007). The type of surfactant is important to consider, because surfactants attain multiple different properties that effects the efficiency of foam (Enick and Olsen, 2012). In addition to the ability of effectively generate foam, the property of low adsorption onto the rock surface is also crucial. A high adsorption rate may decelerate the surfactant front and impair the recovery potential. The adsorption is primarily controlled by the electrostatic interactions between surfactants and minerals in the reservoir rock. Anionic surfactants usually encounter low adsorption in sandstone reservoir because of their negatively charged head group and a somewhat negatively charged rock surface. Cationic surfactants on the other hand, carry a positively charged head group, and thus experience a low adsorption factor on the positively charged rock surface of carbonate formations. Based on a low degree of adsorption on dolomite materials under moderate temperatures, the selected foaming agent for the dolomite reservoir in East Seminole, is a water-soluble nonionic $C_{12-14}E_{22}$ Huntsman surfactant (Jian et al., 2016).

4.5.2 Surfactant Concentration Effect

The foam design greatly depends on surfactant concentration due to its effect on CO_2 relative permeability. An increment in concentration leads to a reduction in CO_2 relative permeability. This is shown for a CO_2-brine system in a Berea sandstone core, in Figure 4.4. The relative permeability of water is unaffected by surfactant concentration in a water-wet system, due to its phase continuity along the pore walls. The non-wetting gas is located in the center of the pores and is thus more sensitive to surfactant concentration and discontinuity (Enick and Olsen, 2012).

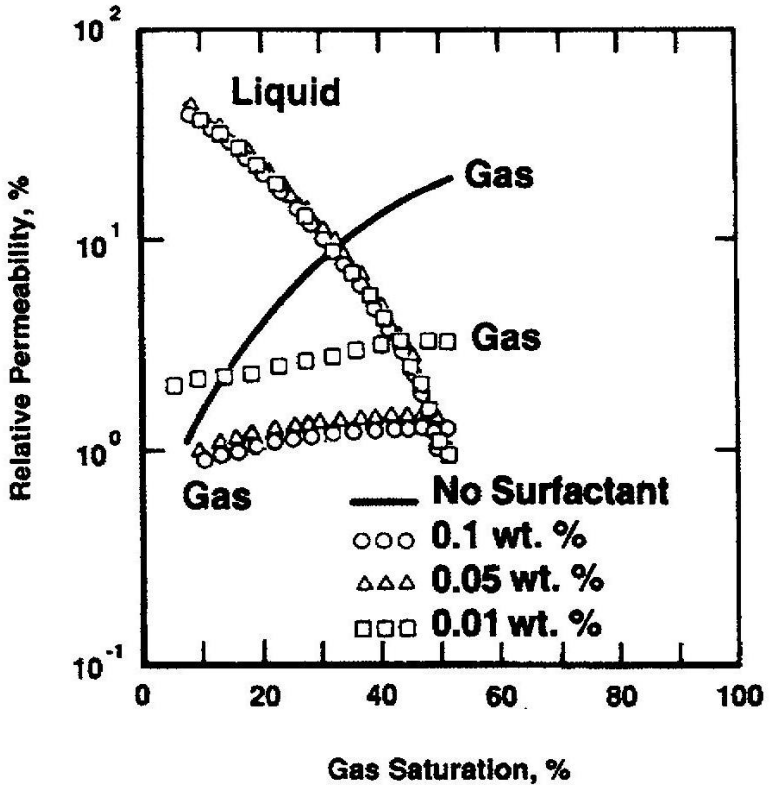

FIGURE 4.4: The effect of surfactant concentration on the gas relative permeability in a water-wet Berea sandstone core (Enick and Olsen, 2012)

4.5.3 Foam Quality

Another parameter that controls the foam stability and influence the foam design, is foam quality. Foam quality indicates the percent volume of gas within the foam, at a specific temperature and pressure. Generally, at a fixed total injection velocity, foam tend to experience two distinct flow characteristics, dependent on the gas fraction (Gajbhiye and Kam, 2011). The flow characteristics are divided into a low quality regime and a high-quality regime, which is illustrated in Figure 4.5. The schematic shows that for $f_g < f_{gth1}$ the apparent viscosity of foam (μ_{app}) increases gradually with foam quality, while for $f_{gth1} < f_g < f_{gth2}$, ($\mu_{app}$) increases rapidly until the maximum foam quality is reached at f_{gth2}.

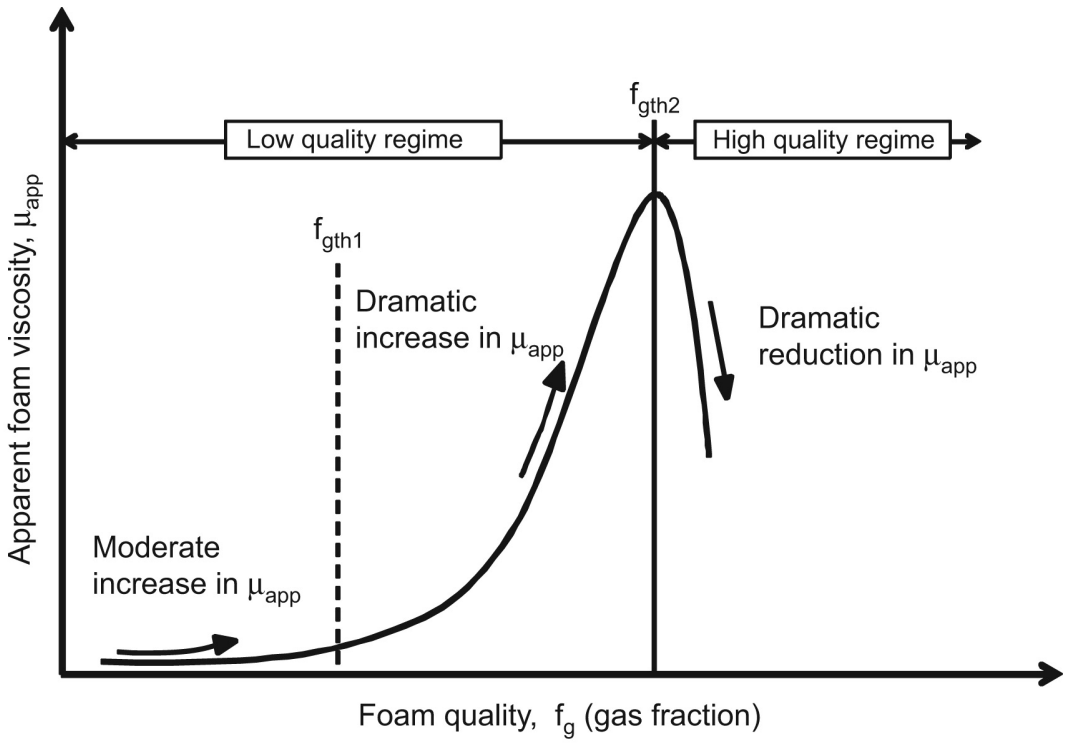

FIGURE 4.5: Changes in apparent foam viscosity as a function of foam quality at a fixed total injection velocity.

(Gajbhiye and Kam, 2011)

As shown in Figure 4.5, a low-quality foam often develop from a low gas fraction and reciprocate a wet foam with a relatively low apparent viscosity and a high mobility. Contrarily, a high-quality foam often require a high gas fraction, which gives a dry foam with a relatively high apparent viscosity and low mobility. However, it is also evident from Figure 4.5, that after reaching a certain gas fraction limit (f_{gth2}), the apparent viscosity rapidly decreases, as for the stability of foam and mobility reduction of gas.

4.5.4 Oil Saturation Effect on Foam

Oil has a detrimental effect on foam stability and efficiency. An increased oil saturation leads to drainage of water in the lamellae (Mukherjee et al., 2016). The drainage destabilizes the lamellae, which in turn weakens the foam and cause an inefficient mobility control performance. This is one of the reasons why the mobility control by foam is more efficient in high-permeability, low-saturated oil zones than in low-permeability, high-saturated oil zones. The feature is advantageous as it allows mobility of CO_2 in low-permeability regions which ultimately improves the sweep efficiency of CO_2.

5. Literature Review of Foam Field Pilots

Despite a substantial collection of promising results of foam for gas mobility control from laboratory studies, the potential of mobility control foam remains to be fully explored on field-scale (Enick and Olsen, 2012). Nonetheless, based on the reviewed field pilots, there is strong evidence in literature that foam may be applicable to effectively improve sweep efficiency of CO_2 and subsequently enhance the oil recovery process without risk of detrimental effect on the reservoir. This chapter provides a review of some of the successful foam field pilots conducted for mobility control.

A CO_2 foam field pilot in a sandstone reservoir in Salt Creek Field, Wyoming, demonstrated in-depth mobility control and improved sweep efficiency (Patil et al., 2018). CO_2 foam application increased the efficiency of CO_2 by reducing the CO_2 utilization factor compared to CO_2 injection. Overall, the foam performance increased oil production by 250,000 bbl and decreased CO_2 injection by 22%.

One of the largest and most successful foam field applications was implemented at the Snorre Field in the North Sea (Aarra et al., 2002). Instead of CO_2, the displacement gas was a hydrocarbon mixture with approximately 70% methane gas. Based on modeling results and material balance, the oil recovery by SAG was 1,600 Mbbl of oil and the displaced volume of oil by methane was 9,900 Mbbl (Sheng, 2013). Based on incremental oil production and a low cost of surfactant treatment, the project represents a technical and economical achievement.

Another successful field pilot using hydrocarbon gas in foam for mobility control, is the Cusiana field foam test in Colombia (Rossen et al., 2014). As nearly 50% of the injected gas flowed in one high-permeability layer before foam implementation, this became a targeted layer for mobility control. After foam injection, reduced injectivity in the targeted layer, and increased injectivity in other layers, indicated a reduced gas mobility by foam in the treated layer. Injection logs also indicated a continued mobility reduction of gas by foam after long-term injection of gas.

Additionally, there are multiple foam pilots designed in recognition that foam can provide both conformance and mobility control simultaneously (Grigg et al., 2002). One example is a successful field test in the Slaughter Field in Texas, where a reduction in gas injectivity indicated generation of foam. Further, a completely diversion of fluids from a thief zone was evidenced from injection profile logs. After foam implementation, one of the producers in the pilot pattern experienced a 50% decrease in gas production, and the cumulative oil production in the pattern increased by approximately 26%.

6. Reservoir Simulation

This chapter describes fundamental principles of reservoir simulation, governing equation solved for simulation, numerical solution methods and the reservoir modeling approach of prediction, history matching and sensitivity analysis. The basis of streamline simulation is also presented.

6.1 Fundamental Principles

Reservoir simulation permits quantification and interpretation of physical phenomena in a reservoir by numerical modeling, with adequacy to extend the phenomena to project future performance (Schlumberger, 2014). The fundamental principle of reservoir simulation is based on mathematical models with a set of equations and assumptions that enables calculation of the fluid flow in the reservoir (Ertekin et al., 2001). The purpose of reservoir simulation is to estimate field performance such as oil recovery to assist engineers in decision making (Holstein, 2007). It is an important tool for petroleum engineering as it enables simulation of a real reservoir without the cost of real life trial and error (Schlumberger, 2016). Reservoir simulation allow for example testing of different production scenarios to evaluate optimal well placing and drainage strategy (Holstein, 2007). It also enables reserves estimation, cost estimations and uncertainty analysis. The Eclipse compositional simulator by Schlumberger is applied for numerical modeling in this Thesis.

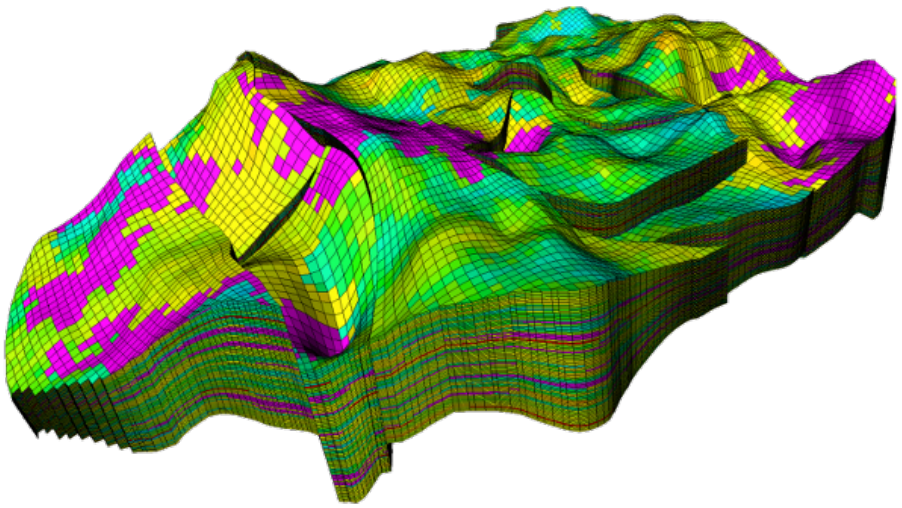

FIGURE 6.1: An illustrative example of a mathematical 3D reservoir model created by Correia et al. (2015).

The basics of reservoir simulation consist of numerical calculation of differential equations to attain fluid saturations and pressures that describes the flow of the reservoir fluids (Schlumberger, 2016). In order to calculate the reservoir and fluid properties of the entire reservoir, the model is divided into multiple discrete cell units in three dimensions (x, y, z) (Schlumberger,

2014). The progression of the properties of each cell unit is further modeled through time and space in a series of discrete steps.

6.2 Governing Equations

The governing equations that are common for all reservoir simulators are Darcy's Law and the material balance equation (Schlumberger, 2014). Darcy's law is an empirical equation that describes the fluid flow in a porous media. The validity of Darcy's law depends on the assumptions of having a laminar flow of an incompressible fluid. For a horizontal, one-dimensional, linear, one-phase flow, Darcy's law can be written as:

$$u = -\frac{K}{\mu}\frac{\partial P}{\partial x} \tag{6.1}$$

where u is the Darcy velocity, K is the absolute permeability, μ is the viscosity of the fluid and P is the fluid pressure.

For a multiphase flow, the Darcy velocity for a fluid is defined as:

$$u_l = -\frac{K k_{rl}}{\mu_l}\left(\nabla P_l - \rho_l \frac{g}{g_c}\right) \tag{6.2}$$

where l denotes the fluid phase, k_{r_l} is the relative permeability of the respective phase, ρ_l is the fluid density, g is the gravity acceleration and g_c is a conversion constant.

In a Cartesian coordinate system, the vector gradient operator is defined by:

$$\nabla = i\frac{\partial}{\partial x} + j\frac{\partial}{\partial y} + k\frac{\partial}{\partial z} \tag{6.3}$$

While Darcy's law describes the fluid flow in the reservoir, the material balance equation assure that the mass flux in the reservoir, is exactly balanced by mass accumulation in the reservoir plus the cumulative contribution or loss from injectors or producers. With the assumption of a stationary flow and constant fluid density and viscosity, the material balance equation can be expressed as:

$$-\nabla \cdot M = \frac{\partial}{\partial t}(\rho\phi) + Q \tag{6.4}$$

where M is the mass flux, ρ is the density, ϕ is the porosity and Q is the cumulative flow contribution or loss from injectors or producers.

The combination of Darcy's law and the material balance equation creates a simulator flow equation that is solved for each cell unit at each time step:

$$\bigtriangledown \cdot [(\frac{k_r}{\mu\beta})(\bigtriangledown P - \rho\frac{g}{g_c})] = \frac{\partial}{\partial t}(\frac{\phi}{\beta}) + \frac{Q}{\rho} \tag{6.5}$$

The term in brackets represents the mobility of a fluid phase, where k_r is the relative permeability of that phase and β is the volume factor.

Additionally, a well model is required to calculate the flow from injectors and towards producers:

$$q_{p,j} = T_{wj} M_{p,j} (P_j - P_w - H_{wj}) \tag{6.6}$$

$q_{p,j}$ represents the volumetric flow rate of phase p in connection j. The flow is defined as positive from the formation into the well and negative from the well into the formation. T represents the transmissibility factor, M is the mobility, P_j is the nodal pressure in the grid block containing the connection, P_w is bottom hole pressure (BHP) of the well and H_{wj} is the well pore pressure head between the connection and the well's BHP datum depth.

T_{wj} represents the transmissibility factor in connection j, which is the representative permeability between two cell centres (averaged permeability). The transmissibility include geometric factors and reservoir properties, and in some cases also fluid properties (Schlumberger, 2016). The transmissibility factor in a connection can mathematically be defined as:

$$T_{wj} = \frac{c\theta \cdot Kh}{ln(r_o/r_w) + S} \tag{6.7}$$

where c is a unit conversion factor, θ is the angle of the segment connecting with the well, Kh is the effective permeability times the net thickness of the connection, r_o is the pressure equivalent radius of the grid block, r_w is the well bore radius and S is the skin factor.

The phase mobility of connection j, is defined as:

$$M_{p,j} = \frac{k_{p,j}}{\beta_{p,j} \cdot \mu_{p,j}} + R_i \frac{k_{p,j}}{\beta_{p,j} \cdot \mu_{p,j}} \tag{6.8}$$

R_i represents the solution gas ratio (R_s) for gas phase and the vaporized oil ratio (R_v) for oil phase.

6.3 Numerical Solution of the Flow Equations

6.3.1 Finite difference discretization

The simulation equations may be solved by different numerical methods (Schlumberger, 2014). By default, Eclipse uses a finite difference approach where the governing equations are discretized on a fixed grid. By finite difference discretization, all derivatives in differential equations are approximated by finite differences (Nguyen et al., 2014). The finite differences are linear combinations of function values from different grid points. Thus, the analytic and continuous representation of differential equations is altered to discrete problems that enables numerical computation. There are three various approximations for derivatives; forward, backward and central difference approximation, which of all are represented in Figure 6.2.

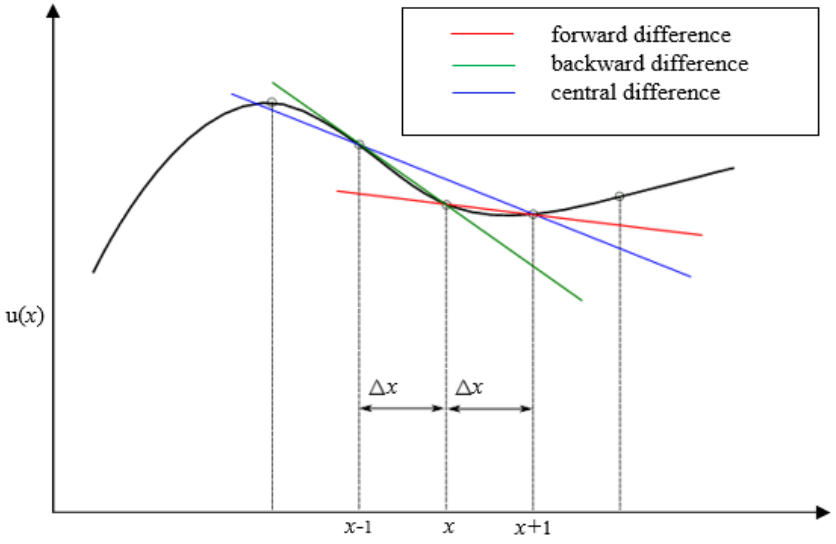

FIGURE 6.2: Example of the three finite difference approximations; forward, backward and central approximation (Nguyen et al., 2014).

Forward difference approximation follows the equation:

$$\left(\frac{\partial u}{\partial x}\right)_i \approx \frac{u_{i+1} - u_i}{\Delta x} \tag{6.9}$$

Backward difference approximation follows the equation:

$$\left(\frac{\partial u}{\partial x}\right)_i \approx \frac{u_i - u_{i-1}}{\Delta x} \tag{6.10}$$

Central difference approximation follows the equation:

$$\left(\frac{\partial u}{\partial x}\right)_i \approx \frac{u_{i+1} - u_{i-1}}{\Delta x} \tag{6.11}$$

For reservoir simulation, the finite difference method also includes two different solving techniques; Fully Implicit formulation and Implicit Pressure-Explicit Saturation (IMPES) formulation (Schlumberger, 2014). The Fully Implicit methodology solves both pressure and saturation simultaneously, while IMPES is based on saturation and pressure from a previous time level (Marcondes et al., 2009). As the IMPES procedure only calculates the pressure, not saturation, it substantially reduces the size of the linear system of equations to be solved compared to Fully Implicit procedure (Franc et al., 2016). Further, this leads to less computational effort per time time step, for the IMPES formulation. However, the IMPES approach is impaired by critical numerical stability restrictions on the size of the time step.

6.3.2 Nonlinear Iteration

The simulation equations are nonlinear and solved by an iterative process based on Newton's method (Schlumberger, 2016). The iterative process progress as follows:

- Nonlinear equations are linearized
- Linear equations are solved
- Linear solution is inserted into the nonlinear equation
- If the solution is good enough, the simulation advance to the next time step
- If the solution is not good enough, the change required to improve the solution is computed and the process is restarted

Step 1 to 3 of the iterative convergence process is a single nonlinear iteration, represented by the green box in figure 6.3. An increasingly number of nonlinear iterations for a time step, indicates an increasingly difficulty to converge (Schlumberger, 2014). In order to decide when a solution is "good enough", a convergence test is required (Schlumberger, 2009). The test decides the adequate number of iterations before the process advance to the next time step. The basic convergence test in the compositional model in Eclipse, is based on the change of solution. Initially, one also define a limit on the number of nonlinear iterations. If the number of iterations exceeds the limit, the simulator attempt to iterate on a shorter time step.

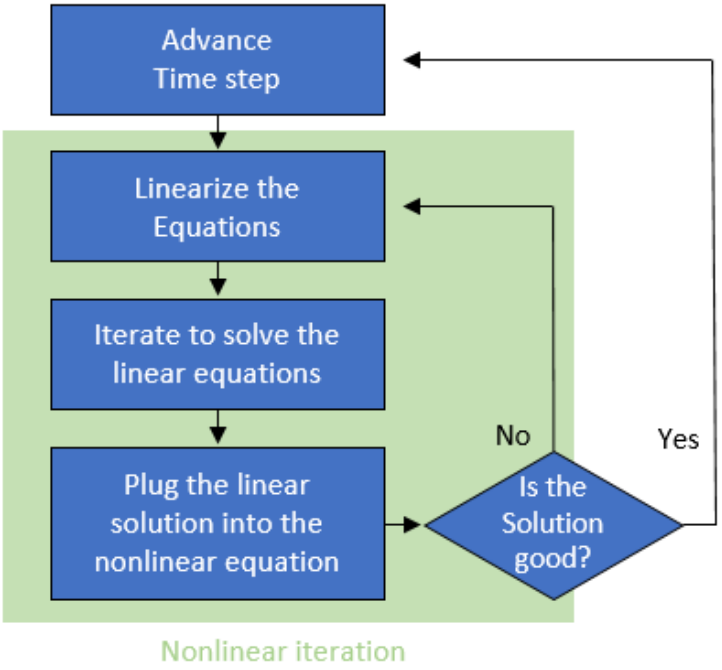

FIGURE 6.3: Iterative convergence process during nonlinear flow equation calculation (Schlumberger, 2014).

6.3.3 Input Data and Computation Order

The simulated flow is often influenced by three main parts (Schlumberger, 2016):

- The flow from one grid cell to another
- The flow from one grid cell to a well completion
- The flow in the wells and surface networks

These parts are considered in the flow equations that Eclipse is solving, which is essentially the product of transmissibility, mobility and potential difference (Schlumberger, 2014). The respective terms are calculated based on a reservoir characterization model built by reservoir descriptive input data. Common input data include petrophysical data and rock data from special core analysis (SCAL) experiments for geometry and reservoir properties and PVT data for fluid properties (Ertekin et al., 2001). Additionally, it is necessary to determine initial conditions for pressure and saturation and well data of location and affiliated rates. The latter is important for the model to be able to mimic historical production rates. The relation between the input data and the calculation of transmissibility, mobility and potential difference, is illustrated below.

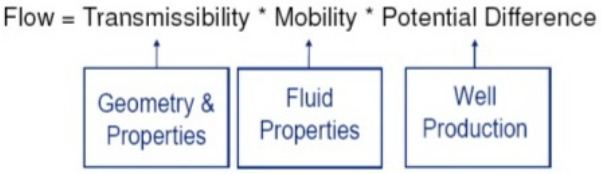

FIGURE 6.4: Overview of the Eclipse flow equation with associated properties and data (Schlumberger, 2016)

Eclipse runs the reservoir characterization model and calculates the flow equations based on a data file created by the engineer (Schlumberger, 2014). The data file contains an arrangement of sections with general model characteristics, grid data, fluid and rock data, regions, solution, output summary and time dependent data for well performance. The structure of these sections is as follows:

1. GRID section
2. EDIT section
3. PROPS section
4. REGIONS section
5. SOLUTION section
6. SUMMARY section
7. SCHEDULE section

The sections are organized in a specific order contingent of what the simulator solves first. The first section allocates the memory for input data, while the next sections processes the grid geometry, fluid and rock properties, initial conditions, output data and finally the well production and injection data. Figure 6.5 illustrates which sections that are related to the different terms in the flow equation.

FIGURE 6.5: Illustration of the how the sections in Eclipse is related to the flow equation (Schlumberger, 2016)

6.4 Reservoir Modeling Approach

The essential purpose of reservoir modeling it to predict field performance and ultimate recovery to evaluate recovery efficiency and economics of different recovery strategies. The reservoir modeling approach include (Holstein, 2007):

- Collection and interpretation of reservoir data
- Construction of a representative reservoir model
- Validation of model against historical production data
- Prediction of future performance
- Cost estimation and comparison of production scenarios

The reservoir modeling process include inevitable errors linked to reservoir input data, model approximation and observable history data (Ertekin et al., 2001). For proper decision making at the end of the modeling process, uncertainties must be thoroughly assessed. History matching is a part of uncertainty quantification, where a level of confidence in the validity of the model may be established by achieving a reasonable agreement between simulated results and historical field data.

In figure 6.6, a history matching is examined in terms of a general reservoir modeling workflow. As the geological model is constructed with an analytic reservoir description, it creates a basis for a fluid flow model Ertekin et al. (2001). After simulation, the pressure and production data from the fluid flow model is matched against observed production data. Through sensitivity runs and tuning runs, the most sensitive model parameters are identified and modified to achieve a refined model and improved match of data. If the model obtain a good match, and the modifications of data are reasonable, the model is ready for production forecasts and revenue estimates.

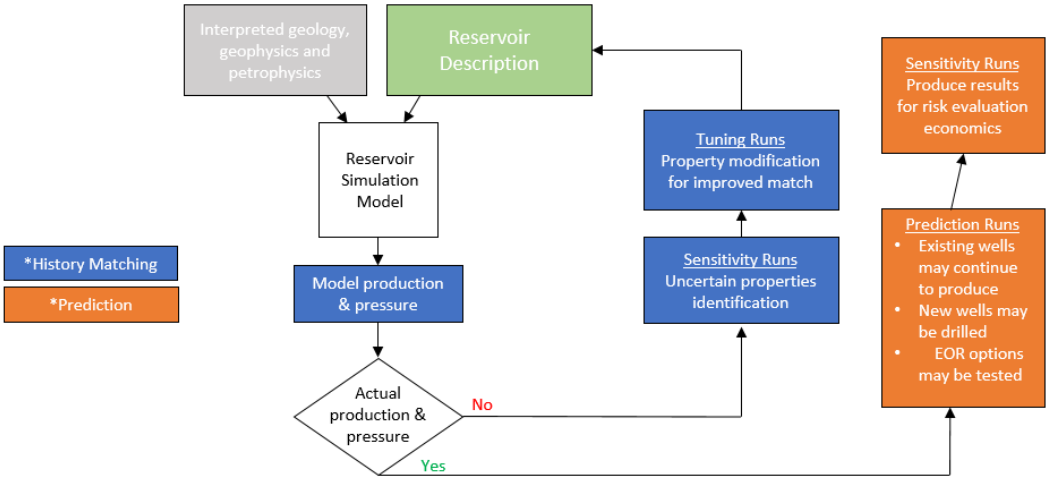

FIGURE 6.6: Workflow of history matching and prediction during reservoir modeling (Schlumberger, 2014).

The history matching process may be seen as a screening process to select a model that best match static and dynamic reservoir data (Schlumberger, 2014). However, history matching should be undertaken for the purpose of decision making, and serves no purpose on its own. Ultimately, it is only a tool that assist the model with an uncertainty management used for decision making (Schlumberger, 2014). Thus, it is important that the selection of model follows a fit for purpose approach and that the parameter modifications are consistent with underlying geological data and complies to physical validity (Holstein, 2007). To ensure modification consistency and physical validity, a comprehensive understanding and professional interpretation of reservoir data is required.

6.5 Streamline Simulation

A small part of the simulation work in this thesis, include the use of Eclipse FrontSim streamline simulator to identify the injection pattern of CO_2. Streamlines are tangential lines to an instantaneous, local velocity field, which essentially represent the flow from injectors and aquifers, to producers (Batycky and Thiele, 2016). This technique offer an effective solution to define injector patterns, which is schematically shown in the figure below.

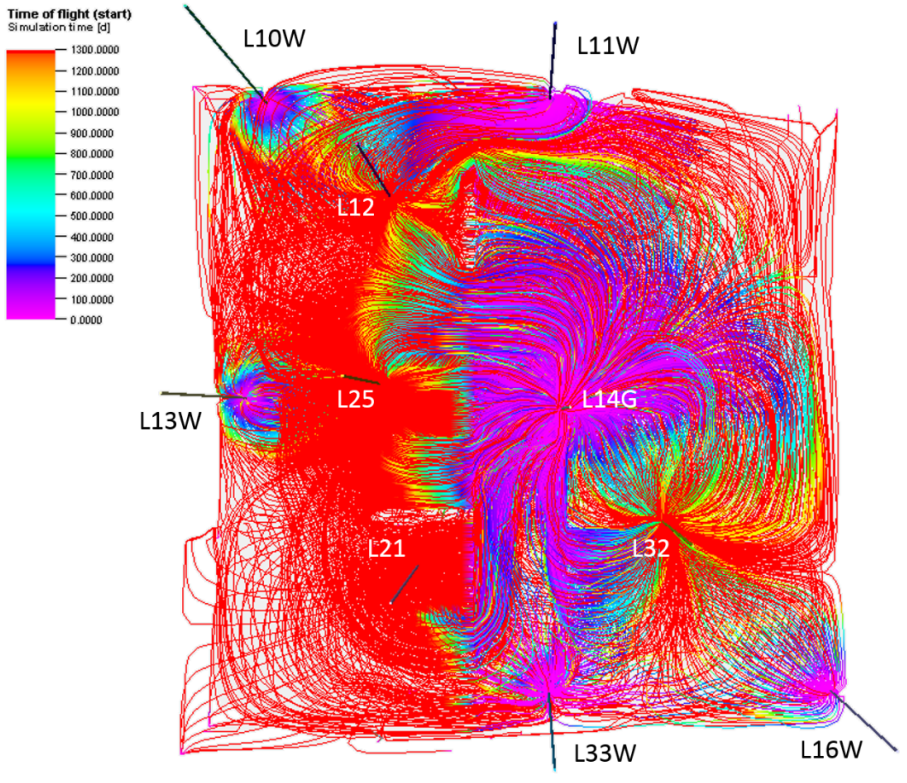

FIGURE 6.7: An example of flow pattern as streamlines from the reservoir simulation in this Thesis, which will be presented in chapter 9.

In contrast to conventional cell-based simulation such as finite-differences, streamline-based flow enables transport of phase saturations and components along a flow-based grid (Thiele et al.,

2010). This leads to a significant efficiency in solving a large number of cells in heterogeneous models, when the physical simulation system meet the key assumptions of the formulation. One of the key assumption of streamlines simulation involve an approximate incompressible system (Batycky and Thiele, 2016). This lead to a decoupling of saturations from the underlying pressure field and allow each streamline to be independent. Since CO_2 attain liquid properties during injection, this is a reasonable assumption for CO_2 floods.

For surveillance purposes, such as injection pattern identification, the main target is to determine current well pairs and allocation, instead of forecasting (Batycky and Thiele, 2016). Hence, simplifications can be made when calculating the total velocity field required to trace the streamlines. Specifically, the solution of the velocity field is determined by:

- Observed total volumes in injectors and producers
- Geology description with potential faults and flow barriers
- An assumption of fluid distribution in the reservoir

For Thesis, streamlines are used to illustrate the time-of-flight (TOF) and to calculate injection fractions and production fractions. The TOF is the time required for a neutral tracer to travel along a streamline, from the injector to the producer and is calculated from the following equation (Hægland et al., 2007):

$$TOF = \frac{PV}{Q} \tag{6.12}$$

where PV represents the total pore volume that the fluid fills and Q represents the injection rate into the streamline.

The TOF's are proportionally related to the breakthrough time of a tracer, as breakthrough times are based on the local velocity of a tracer between the injector and producer, along a streamline. This means that streamlines with shorter TOF's will have faster breakthrough times.

The streamline simulation is used to calculate injection fractions for the pilot injector and production fractions for each producer in the pilot area. This is production and injection allocation amounts that are calculated at particular time steps and depend on production rates and injection rates. The injection fractions represent the fraction of the total volume injected in an injection, that supports the reservoir volume production in each producer (Schlumberger, 2016). The production fractions for a producer, represent the fraction of reservoir volume production, that is compensated by injection from each injector, included support from aquifers present.

6.6 Empirical Models for Relative Permeability Calculations

One of the most important parameters to consider when simulating the flow of water, oil and gas in a reservoir, is the two-phase and three-phase relative permeabilities (Sorbie and Van Dijke, 2005). Some of the most prevalent models used to simulate relative permeabilities are described below.

6.6.1 Two-phase Relative Permeability

Two-phase relative permeabilities can be calculated based on a Modified Brooks-Corey (MBC) model (Brooks and Corey, 1964). The model depends on parameters obtained from experimental core flood data. The model is compounded by the following relations:

$$k_{ro} = k_{ro,max}(\frac{S_o - S_{or}}{1 - S_{or} - S_{wc} - S_{gc}})^{n_o} \tag{6.13}$$

$$k_{rw} = k_{rw,max}(\frac{S_w - S_{wc}}{1 - S_{or} - S_{wc} - S_{gc}})^{n_w} \tag{6.14}$$

$$k_{rg} = k_{rg,max}(\frac{S_g - S_{gc}}{1 - S_{or} - S_{wc} - S_{gc}})^{n_g} \tag{6.15}$$

where k_{ri} is the relative permeability, $k_{ri,max}$ is the maximum relative permeability by the modified Brooks-Corey functions, S_i, S_{ic} and S_{ir} is the initial, critical and residual saturation, and n_i is the exponent of phase i, when i= o, w or g for oil, water and gas.

6.6.2 Three-phase Relative Permeability

Three-phase flow differ from two-phase flow, and should not be straightforwardly derived from a combination of two-phase parameters (Sorbie and Van Dijke, 2005). The behavior of multiphase flow is complex, especially at heterogeneous wettability conditions. Several empirical models are derived to express three-phase relative permeability from two-phase data, as it is difficult and time-consuming to directly measure three-phase relative permeabilities. The empirical models include Stone I and Stone II.

Based on the three-phase pore occupancy in a strongly water-wet porous medium and the two-phase relative permeabilities for such a system, Stone (1970) was able to define an empirical model for three-phase relative permeabilities. The Stone I model defines the following normalized fluid saturation functions (Sorbie and Van Dijke, 2005):

$$S_o^* = \frac{S_o - S_{om}}{1 - S_{wc} - S_{om}} \text{ for } S_{om} \leq S_o \leq 1 - S_{wc} \tag{6.16}$$

$$S_w^* = \frac{S_w - S_{wc}}{1 - S_{wc} - S_{om}} \text{ for } S_{wc} \leq S_w \leq 1 - S_{om} \tag{6.17}$$

$$S_g^* = \frac{S_g}{1 - S_{wc} - S_{om}} \text{ for } 0 \leq S_g \leq 1 - S_{wc} - S_{om} \tag{6.18}$$

where S_o^*+ S_w^* + S_g^*=1.

Stone (1970) also defined two factors $\beta_w(S_w^*)$ and $\beta_g(S_g^*)$, to account for the reduction in three-phase oil relative permeability due to the presence of water and gas:

$$k_{ro}(S_w^*, S_g^*) = So^* \cdot \beta_w(S_w^*) \cdot \beta_g(S_g^*) \tag{6.19}$$

The defined factors $\beta_w(S_w^*)$ and $\beta_g(S_g^*)$ are functions of their own normalized saturations S_w^* and S_g^* and the two-phase relative permeabilities of oil:

$$\beta_w = \frac{k_{row}}{1 - S_w^*} \tag{6.20}$$

$$\beta_w = \frac{k_{row}}{1 - S_w^*} \tag{6.21}$$

From this, the Stone I model for k_{ro} becomes:

$$k_{ro}(S_w^*, S_g^*) = S_o^* \cdot (\frac{k_{row}}{1 - S_w^*}) \cdot (\frac{k_{rog}}{1 - S_g^*}) \tag{6.22}$$

The Stone II model was introduced by Batycky and Thiele (1973) to improve the relative permeability prediction in high oil saturation regions. The Stone II model interpolates the oil relative permeability and predicts the residual oil saturation (S_{om}) from the normalized water and gas saturations from the Stone I model. In normalized form, the model may be written as:

$$k_{ro}(S_w^*, S_g^*) = k_{rocw} \left[\left(\frac{k_{row}}{k_{rocw}} + k_{rw} \right) \left(\frac{k_{rog}}{k_{rocw}} + k_{rg} \right) - \left(k_{rw+k_{rg}} \right) \right] \tag{6.23}$$

The two-phase relative permeabilities are considered at the same saturation values as in Stone I model.

Part II

Method

7. Tools and methods for numerical simulation

The macroscopic foam behavior on field scale is simulated in this Thesis to evaluate the CO_2 foam application for mobility control and evaluate sweep efficiency during foam injection. ECLIPSE has been the main tool for numerical simulation of foam, but additional software for data reprocessing and data evaluation has been used, including FrontSim and Petrel E&P. This section elaborates on the techniques used by the software to assist in simulation, data reprocessing and visualization of simulation results.

7.1 Modeling of Foam by Eclipse

The Eclipse compositional simulator (ECLIPSE 300) is used in this Thesis for numerical simulation of the field pilot performance. A compositional model was preferred over a blackoil model (ECLIPSE 100), as the latter does not allow compositional change of oil and gas components. The compositional model allow tracking of each component and modeling of fluids near critical points such as bubble point pressure and minimum miscibility pressure. This is an important element to include for CO_2 injection and CO_2-foam injection, as the component system and fluid behavior are sensitive to changes in temperature and pressure. The Eclipse compositional fluid model assumes an arbitrary number of components in oil and gas, that can change in composition relative to pressure and time, based on an equation of state (EoS). The EoS establishes a relationship between pressure, molar volume and temperature data to calculate the phase behavior.

The compositional foam model consider foam as an effective surfactant concentration in the aqueous phase, which make the concentration of foam proportional to the concentration of surfactants (Schlumberger, 2016). To capture the effect of foam on CO_2 mobility, the distribution of foam and the gas mobility reduction by foam must be modeled.

The distribution of foam is modeled by a conservation equation for foam:

$$\begin{aligned} &\frac{d}{dt}\left(\frac{VS_wC_f}{B_rB_w}\right)+\frac{d}{dt}\left(V\rho_rC_f^a\frac{1-\phi}{\phi}\right)= \\ &\sum\left[\frac{Tk_{rw}}{B_w\mu_w}M_{rf}\left(\delta P_w-\rho_w g D_z\right)\right]C_f+Q_wC_f-\lambda(S_w,S_o)VC_f \end{aligned} \tag{7.1}$$

V is the block pore volume [m^3], S_w and S_o are saturations of water and oil, C_f denotes foam concentration, C_f^a adsorbed foam concentration, B_r and B_w formation volume factor of the rock and water, ρ_r , ρ_w denotes the density of the rock and water, $\sum$ is the sum over neighbouring cells, ϕ is porosity, T is transmissibility, k_{r_w} is relative permeability of water, μ_w is viscosity

of water, M_{rf} is gas mobility reduction factor, P_w is water pressure, g is acceleration due to gravity, Q_w is production rate of water and λ is the rate decay parameter function of oil and water saturation.

The gas mobility reduction by foam is numerically estimated based on experimental data, and in Eclipse it can either be modeled by a population balance model or local equilibrium model. The former explicitly models foam texture and flow in porous media by including pore level mechanisms of foam generation and transport (Kovscek, 2010). For this Thesis, the local equilibrium model is selected for foam modeling, as this offers a more simplified approach to reduce computational effort. The model assumes local equilibrium of foam generation and coalescence of gas bubbles, and is an efficient tool for accurate prediction of foam flow at field scale, for the purpose of evaluating foam application.

With the local equilibrium model, foam application for the field pilot was modeled in a functional form, where the modification of gas relative permeability due to foam ($k_{r,foam}$), where estimated based on the relative permeability of pure CO_2 ($k_{r,g}$) without foam and a mobility reduction factor (M_{rf}):

$$k_{r,foam} = k_{r,g} \cdot M_{rf} \tag{7.2}$$

The mobility reduction factor can be expressed as:

$$M_{rf} = \frac{1}{1 + (M_r \cdot F_s \cdot F_w \cdot F_o \cdot F_c)} \tag{7.3}$$

where M_r is the reference mobility reduction factor, which corresponds to the normalized resistance to flow for minimum bubble size in the absence of factors that increase bubble size. F_s, F_w, F_o and F_c is the mobility reduction component from surfactant concentration, water saturation, oil saturation and capillary number respectively, all derived from laboratory experiments.

The individual reduction factor by surfactant concentration is expressed in equation (7.4). The equation indicates that a low surfactant concentration and a correspondingly weak foam contributes to a low F_s, whereas a high surfactant concentration and strong foam gives a higher individual mobility reduction.

$$F_s = \left(\frac{C_s}{C_s^r}\right)^{e_s} \tag{7.4}$$

where C_s is the effective surfactant concentration, C_sr is the reference surfactant concentration and e_s is an exponent that indicates the rate of change about the point $C_s = C_sr$.

The gas mobility reduction due to water is defined as:

$$F_w = 0.5 + \frac{a \tan\left[f_w\left(S_w - S_w^1\right)\right]}{\pi} \tag{7.5}$$

where S_w is the water saturation, S_w^1 is the minimum water saturation for the foam to be effective and f_w is the weighting factor that govern the sharpness of the mobility change.

The effect of oil on gas mobility reduction can be expressed as:

$$F_o = \begin{cases} \left(\dfrac{S_o^m - S_o}{S_o^m} \right)^{e_o}, & \text{if } S_o \leq S_o^m \\ 0\ , & \text{if } S_o > S_o^m \end{cases}$$

when S_o is the oil saturation, S_o^m is the maximum oil saturation for foam to be effective and e_o is an exponent that determines the steepness of the transition about the point $S_o = S_{o^m}$. The modeling of foam in this Thesis, exclude the effect of oil on gas mobility reduction, due to absent experimental data.

The gas mobility reduction component due to the capillary number is expressed in equation (7.6), where the capillary number is the ratio between viscous and capillary forces. The individual component F_c, governs the gas mobility for shear-thinning in the region of low foam quality.

$$F_c = \left(\frac{N_c^r}{N_c} \right)^{e_c} \tag{7.6}$$

where N_c is the capillary number, N_{c^r} is the reference capillary number and e_c is an exponent that control the degree of transition about the point $N_c = N_c^r$.

The gas-water surface tension versus foam surfactant concentration F_{sc} is also considered by including the foam surfactant concentration and the corresponding gas-water surface tension F_{st}.

7.2 Data Reprocessing and Visualization by Petrel E&P

In addition to Eclipse, an important tool for this Thesis work was Petrel E&P software platform, to visualize and reprocess simulation results. For digital reproduction of simulation results and data visualization, a detailed description of the procedures is included in Appendix A.3.

For data visualization purposes, Petrel has been imperative to evaluate the foam performance. Summary data from Eclipse such as injection and production rates, reservoir pressures and cumulative production has been visualized and evaluated by line plots in Petrel. The 3D result analysis was also performed by visualizing output of grid properties, such as permeability, porosity, transmissibility and saturations.

For data reprocessing purposes, Petrel has been used for streamline simulation via Frontsim and quantification of sweep efficiency. Petrel generated flow patterns as streamlines using simulation

results containing 3D flow properties at reservoir conditions. Injection and production fractions were also extracted after streamlines were generated.

Quantification of sweep efficiency during foam injection, CO_2 injection and WAG, was performed by the use of pseudo tracers in Eclipse and 3D simulation result conversion to grid properties in Petrel. Based on the equation 3.4 and equation 3.5 in section 3.1, the principal idea for calculating volumetric sweep efficiency (E_v) of injected CO_2 and subsequently for injected water, was based on the following equation:

$$E_v = \frac{\text{grid cells contacted by tracer in the reservoir}}{\text{total number of grid cells in the reservoir}} \tag{7.7}$$

7.3 East Seminole Field Pilot Model

7.3.1 Simulation Grid Properties

The applied field pilot model used for reservoir simulation in this Thesis, was created by the PhD candidates Zachary Paul Alcorn from University of Bergen, and Mohan Sharma from the National IOR Centre of Norway at the University of Stavanger. Sharma and Alcorn developed the field pilot model by creating a history matched water flood model and CO_2 flood model for the East Seminole Field. Historical well data, core data, petrophysical logs and the reservoir characterization performed by Honarpou et al. (2010), presented in chapter 2, was used to establish the geological framework of the model. The field model is shown in Figure 7.1, where it represents the pilot area and peripheral water injectors and CO_2 injectors in the East Seminole Field.

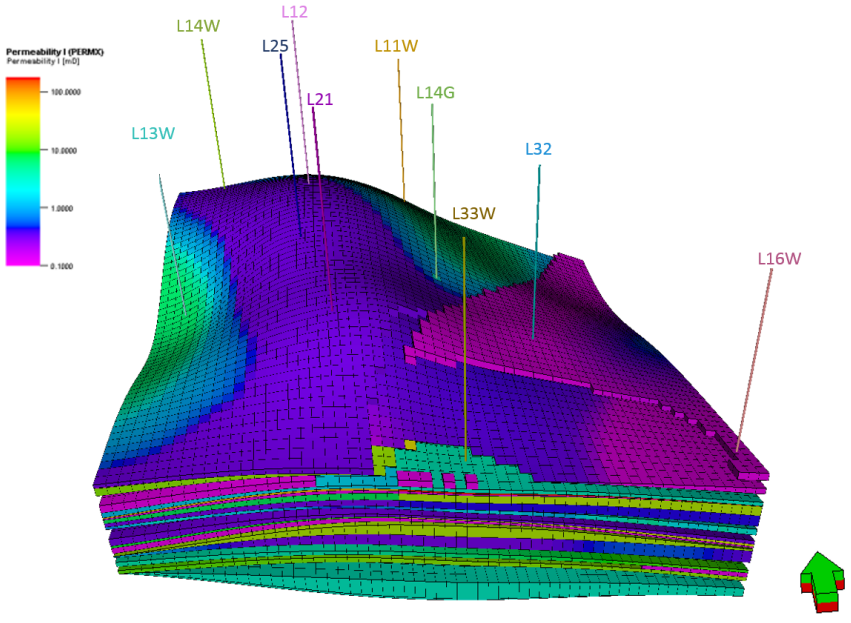

FIGURE 7.1: The East Seminole field pilot model created by Alcorn (2017) and Sharma (2017).

The entire model covers a 1.5 km^2 area of the East Seminole Field and includes the inverted five spot pattern of the pilot area and the surrounding injectors that is assumed to affect the pilot pattern. The model is defined by 95,816 cells in a cartesian, corner point grid system. Stratigraphic layers were established by Alcorn (2017), based on reservoir flow intervals with comparable properties in rock type, porosity, absolute permeability and averaged layer-permeability ratio (K_{vh}). Reservoir heterogeneity was represented by enhanced permeability and porosity layers, correlated to measured intervals. To balance the impact of heterogeneity on reservoir behavior with computational effort, 28 layers were used. Additionally, the model was divided into a Main pay Zone (MPZ) and a Residual Oil Zone (ROZ), based on the reservoir characterization by Honarpou et al. (2010). The simulation grid geometry and the range of different cell properties are summarized in table 6.1.

TABLE 7.1: Simulation grid parameters

Parameter	Value
Total number of grid cells (x, y, z)	96,000 (59 x 58 x 28)
Number of active cells	62,000
Total grid dimensions	370 acres (1.5 km^2)
Total grid thickness	150 ft
Individual grid dimensions (x, y)	2500 ft^2 (50x50 ft)
Average individual grid thickness (z)	6 ft (1-30 ft)
Average porosity	0.075
Average permeability (x, y, z)	11 mD, 8 mD, 6 mD

7.3.2 Model Verification

Sharma (2017) and Alcorn (2017) has performed sensitivity analysis and history matching to assess the uncertainties and the level of validity of the CO2 flood model, which the foam model is initialized from. The water flood model was built to simulate the historical field performance from January 1971 to October 2013, and the CO_2 flood model was built to simulate the continuous historical CO_2 flood from October 2013 to June 2017.

For the water flood model, the simulation was run on liquid rate control with the blackoil simulator. Oil-water relative permeabilities were obtained from the Modified Brooks-Corey (MBC) model, presented in chapter 6, which were tuned to relative permeability data from drainage and imbibition experiments conducted by the PhD candidate Sunniva Brudvik Fredriksen at the Dept. of Physics and Technology, University of Bergen (Rognmo et al., 2018). Through history matching and sensitivity analysis, the water flood model was modified. Pore volume, permeability and oil-water relative permeabilities was identified by Sharma (2017) as the most sensitive uncertainty parameters for the water flood model. Four regions for local transmissibility modifications were implemented to improve the match on liquid rate, by using transmissibility barriers

around producer L12, L21 and L25, which is illustrated in Figure 7.2. Additional modifications of transmissibility barriers have been made during history matching of the CO_2 flood model, which is described below.

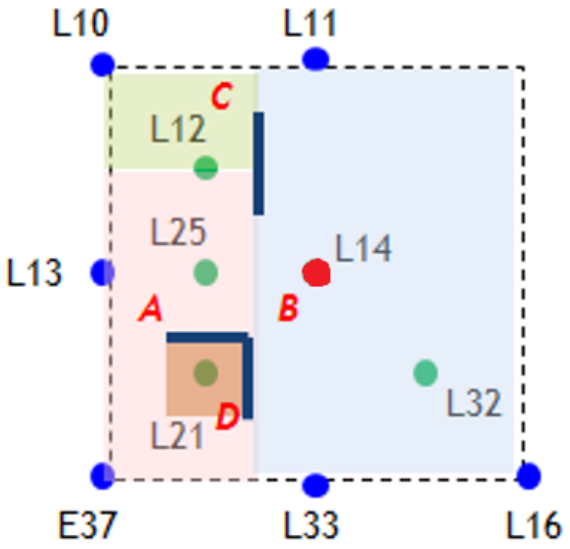

FIGURE 7.2: Areal regions identified for transmissibility modification (A, B, C, D) and transmissibility barrier (black lines) incorporated by Sharma (2017) and Alcorn (2017) during history matching (Sharma, 2017).

The CO_2 flood was initiated from the last step of the water flood model, and was simulated on liquid rate control using the compositional simulator. The two-phase oil-water relative permeability curves from the history matched water flood model was used in addition to gas-oil relative permeability endpoints. The oil-water and gas-oil relative permeability where both were obtained from the Modified Brooks-Corey (MBC) model, presented in section 6.6.1. The MBC model required tuning of MBC model parameters, to available experimental data, which are included in Table 7.2.

TABLE 7.2: Oil-water (left image) and gas-oil (right image) relative permeability data used in the CO_2 flood model(Rognmo et al., 2018).

Oil-water parameter	Value	CO_2-water parameter	Value
ROS	0.32	ROS	0.32
$S_{w,con}$	0.15	$S_{g,con}$	0
S_{wc}	0.15	S_{gc}	0.05
S_{orw}	0.38	$S_{or,g}$	0.12
$S_{o,irw}$	0.25	$S_{o,irg}$	0.12
$k_{rw,iro}$	1.00	$k_{rg,cl}$	1.00
$k_{row,cw}$	1.00	$k_{rog,cg}$	1.00
n_w	2.30	n_g	1.00
$n_{o,w}$	3.20	$n_{o,g}$	1.00

The ROS is the remaining oil saturation in the reservoir after the natural flooding which was described in section 2.4. The $S_{wc,con}$ is the connate water saturation and the S_{wc} is the critical water saturation. S_{orw} is the residual oil saturation after the water flood and the $S_{o,irw}$ is the oil saturation at irreducible water saturation. $k_{rw,iro}$ is the relative permeability for water at residual oil saturation and $k_{row,cw}$ is the relative permeability of oil at critical water saturation. $S_{g,con}$ is the connate gas saturation, S_{gc} is the critical gas saturation and $S_{o,irg}$ is the oil saturation at irreducible gas saturation. $k_{rg,cl}$ is the relative permeability of gas at critical liquid saturation, $k_{rog,cg}$ is the relative permeability of oil at critical gas saturation and n_w, n_o and n_g is the corey exponents for water, oil and gas.

The relative permeability curves from the MBC model and the experimental data from Table 7.2, are shown in Figure 7.3.

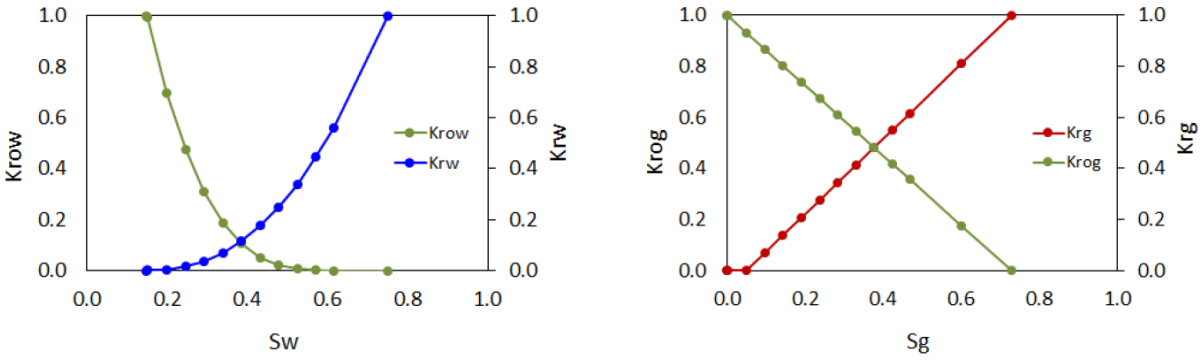

FIGURE 7.3: Oil-water relative permeabilities (left image) and CO_2-water relative permeabilities (right image) from the MBC model and experimental data (Sharma, 2017).

The two-phase relative permeability curves represent an oil-wet system and were used to estimate three-phase relative permeabilities by the Stone II model presented in section 6.6.2.

The CO_2 flood model was history matched on liquid production volume. It was desirable to history match the CO_2 flood model with historical gas production, but due to the absence of a recycling facility at the East Seminole Field, measurements of produced gas was not available until January 2016. Thus, the model was modified to history match liquid production volume. The history match of the liquid production is shown in Figure 7.4.

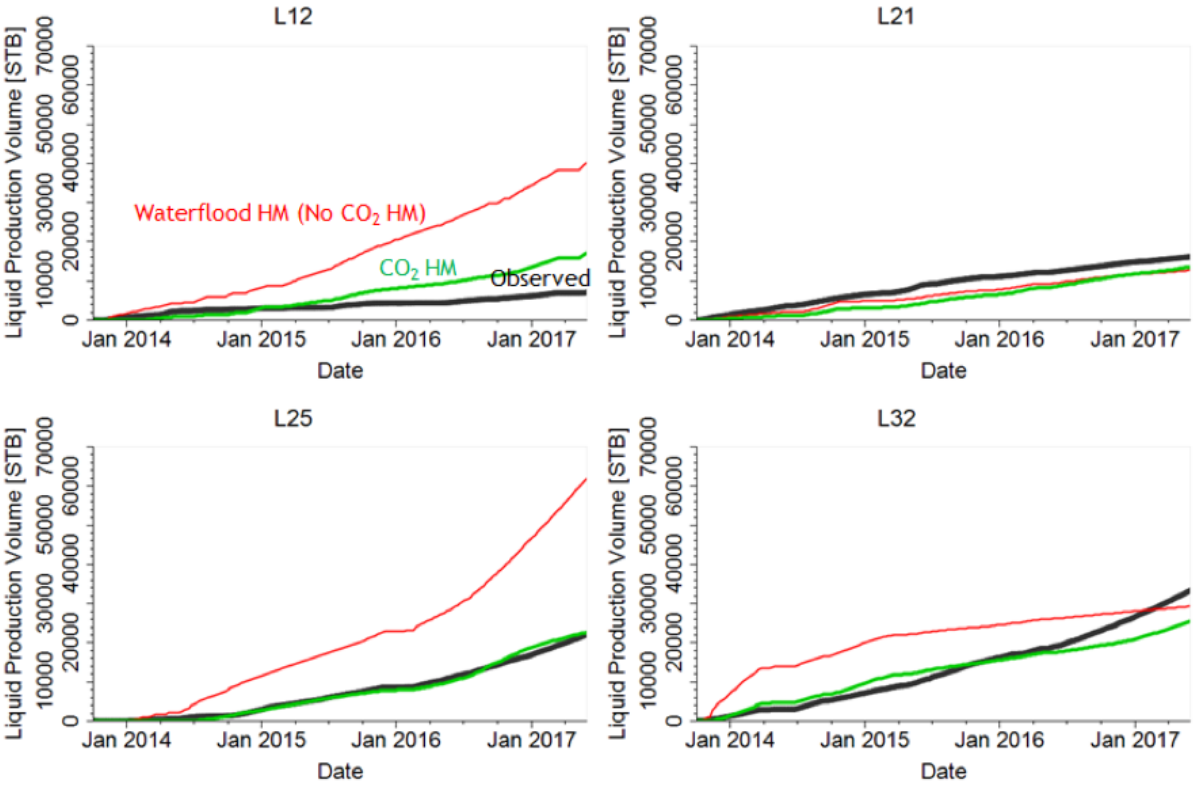

FIGURE 7.4: History match of the liquid production volume in producer L12, L21, L25 and L32 shows a relatively good match between the liquid production volume for historical data and simulated data for the CO_2 history match (Sharma, 2017).

The history match of the CO_2 flood model showed a good match between historical and simulated production volume in producer L25 and some deviation in L12, L21 and L32. During history matching of the CO_2 flood model, additional pore volume and transmissibility modifications were made to the near well bore area of the four producers, in addition to an introduced aquifer to obtain a match between historical and simulated liquid production volume. Ultimately, the model contained transmissibility barrier from L14G to each producer, from L33G to L32, from L13G to L25 and from L10G to L12, in addition to the area around L25, L12, L32. With regards to computational effort, the modifications in pore volume and permeability did not provide detailed distribution of grid properties, which unfortunately resulted in large contrasts pore volume and permeability in the modified layers. The location of transmissibility and pore volume modifications is described in the included data file for the pilot model, in Appendix A.2. Sensitivity analysis considered the pore volume and transmissibility modifications around inter-well regions, and relative permeabilities as the most sensitive uncertainty parameters.

Despite a relatively good match on liquid production volume, the history match of gas to liquid ratio was not good.

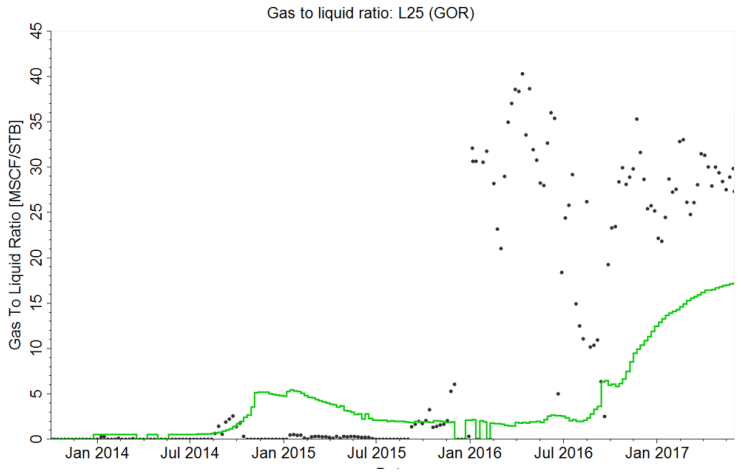

FIGURE 7.5: History match of the gas to liquid ratio for producer L25 shows a poor match from January 2016, when gas production started to be measured Sharma (2017).

Due to the locally incorporated transmissibility barriers between L14G and the producers, the flow between the well pairs was underestimated which resulted in a poor match between simulated and historical gas production data (Figure 7.5. This is a weakness that will affect the gas flow in the field pilot model. The gas production in the field pilot model is expected to be underestimated and the gas breakthrough is expected to be delayed.

Due to large changes in saturation from small to large grid cells around the pore volume modifications, Eclipse experienced convergence error for the modified pore volumes. As mentioned in section 6.3.2, Eclipse performs an iterative convergence to solve the nonlinear flow equations. The converge failure resulted in time step chopping, which resulted in a residual error in the estimated flow. To reduce convergence issues, the memory required for a run was increased. This was done my increasing the linear solver stack size with keyword NSTACK. Additionally, the maximum number of linear iteration in a Newton iteration was increased. This was done by increasing the TUNING.

7.3.3 Reservoir Fluid Model

The foam reservoir model, built by Sharma (2017) and Alcorn (2017), was initialized explicitly based on the pressures, saturations and compositions of gas and water, from the last step of the history matched CO_2 flood. The model was set to calculate phase behavior based on a Peng-Robinson EoS model, with a Peneloux molar volume correction for an appropriate prediction of liquid densities and saturations. The EoS model was tuned to available PVT data, with 6 components, including a separate CO_2 component. The compositions are assumed to be uniform in all of the cells, with values based on the EoS at the start of the CO_2 simulation. A parachor was associated with each component to calculate surface tensions for assessing miscibility. Viscosity calculations are performed in the model by the Pedersen method, which is based on a modification of the corresponding states principle, whereas the viscosity is related

to a reference viscosity, involving critical temperature and pressure, molecular weight and a rotational coupling factor (Ali, 1991). Three-phase relative permeabilities were estimated by the Stone II model presented in section 6.6.2, which was applied to the two-phase relative permeabilities in Figure 7.3. The reservoir fluid model does not include the effect of hysteresis, which is a major weakness for the model.

In addition to oil-water relative permeability measurements, experimental laboratory work has been performed at the University of Bergen, to find optimum foam quality and rate for mobility control by CO_2 foam (Rognmo et al., 2018). Based on foam quality and rate scans with reservoir cores and fluids, tested at reservoir conditions, foam model parameters were established and optimal foam strategies for mobility control were evaluated. Experimental foam model parameters for mobility reduction factor (M_rf) calculation in Eclipse, from section 7.1 were tuned to an empirical foam model and are summarized in the table below.

Table 7.3: Foam model parameters from laboratory experiments

Parameter	Value
Reference M_rf	192
C_s^r	1E-3
e_s	0
C_s	1E-6
S_w^1	0.304
f_w	84.3
N_c^r	9E-7
N_c	0.6
F_{sc}	2E-3
F_{st}	4E-3

For repetition, the reference M_rf is the gas mobility reduction dependence upon reference mobility reduction. The C_s^r is the reference foam surfactant concentration above which a strong foam can form, e_s is the exponent for the rate of change of M_rf due to surfactant concentration and C_s is the minimum surfactant concentration for which gas mobility reduction due to the presence of foam will be calculated. The S_w^1 is the limiting water saturation below which foam is effective and f_w is the weighting factor which controls the sharpness in change of mobility. N_c^r is the reference capillary number and N_c is the exponent for the rate of change of M_rf according to the ratio of reference to calculated capillary number. Ultimately the F_{sc} and F_{st} is the surfactant concentration with the corresponding gas-water surface tension.

Due to absence of experimental data for the maximum oil saturation above which foam ceases to be effective and the rate of change of mobility reduction due to oil saturation, the foam model does not include the gas mobility reduction dependence upon oil saturation. This may overestimate the strength of foam performance in the presence of oil. As low-permeable layers

generally contains more residual oil compared to high-permeable layers, the foam performance is expected to be most affected by oil in low-permeability layers realistically. Because the foam model of the field pilot model does not include this effect of oil on foam, foam performance will be overestimated in low-permeability, high saturated layers.

7.4 Baseline Model Modifications

Changes have been made to the baseline field pilot model and injection strategies established by Sharma (2017) and Alcorn (2017), to evaluate CO_2 foam performance and sweep efficiency at field scale. A detailed description of the well control and foam injection strategies in the baseline field pilot model are included in Appendix A.1. This section presents a description of the modifications made on the baseline field pilot model and the simulation cases by Sharma (2017) and Alcorn (2017). The model was modified with formation of fluid-in-place regions for quantification of sweep efficiency. Local grid refinement was also performed on the model for sensitivity analysis on grid resolution. To track CO_2 and water during field pilot injection and evaluate sweep efficiency, pseudo tracers were implemented. Additionally, well controls and base injection strategies were altered to create comparable relation between foam injection strategies, CO_2 injection and WAG. The complete data file of the field pilot model is shown in Appendix A.2.

As mentioned in chapter 6, the simulation data file that is run by Eclipse to simulate reservoir performance comprise of the following structure:

1. 1) GRID section
2. 2) EDIT section
3. 3) PROPS section
4. 4) REGIONS section
5. 5) SOLUTION section
6. 6) SUMMARY section
7. 7) SCHEDULE section

The time dependent modeling data in the SCHEDULE section of the simulation data file, has been the most frequently modified data for reservoir simulation in this Thesis.

7.4.1 well control and injection strategy adjustments

The well control adjustment in the SCHEDULE section, included a change of the control mode for injection from liquid rate target to BHP target, a replacement of peripheral gas injectors to water injectors, a change of chase fluid for chase fluid injection after foam injection and WAG and a change of injection time for different injection slugs in the pilot injector L14G.

The field pressure development varies in the reservoir, for different injection strategies applied in pilot injector L14G. Because of different pressure conditions for each scenario and because of a liquid rate target for all injection wells, the injected volume from the surrounding peripheral injection wells varied for each scenario. This affected total field performance for each scenario and made it difficult to compare the effect of foam injection in L14G on field performance. To be able to appropriately compare the field performance effect of different injection strategies in L14G, the peripheral injectors in the pilot pattern had to inject the same volume for all scenarios, while the pilot injector was the only injector that changed for different scenarios. Thus, the peripheral injectors were set to inject at a constant BHP target of 4400 psia, instead of a preset liquid rate target. This was done by changing item 4 and 7 for each injection well in the WCONINJE keyword, in the SCHEDULE section of the data file for each simulation case. The WCOINJE keyword was responsible for the control data for the injection wells, and was applied with the WELOPEN keyword, which control the opening and shutting of the wells. In item 4 for of the WCONINJE keyword, the control mode for the respective injector was changed from liquid rate target control to BHP target control and in item 7, the BHP pressure target was set to 4400 psia.

An important consideration when evaluating the sweep efficiency for different injection strategies, was gas saturation increase in the reservoir and gas breakthrough. To be able to only consider the effect of gas saturation increase and gas breakthrough for different injection strategies in L14G, all injectors except L14G were set to inject water. This involved changing L10G, L13G and L33G from gas injectors to water injectors for all scenarios. This was done by changing item 1 and 2 in the WCONINJE keyword in the SCHEDULE section. In item 1, the injection name was changed from G to W, indicating a change of injection type from gas to water injector. In item 2, the injection type was specified to water injector.

In addition to the control mode change and injection type change in the WCONINJE keyword, the injection times for different injection slugs in L14G were changed for different simulation cases. Dependent on the injection strategy, the TSTEP keyword that associates to the WCONINJE keyword, was set to the desired injection time for each injection slug and a corresponding report timestep. For each timestep value, the simulator would advance to a new report time. To remain consistency, the timesteps for all the injection strategies, were set to request a report for every tenth timestep. Consequently, for 1 cycle with a 30 days duration, the timestep would was 3*10. During the chase fluid injection, the timesteps were changed to request a report for every month, corresponding to 12*30.

7.4.2 Fluid-in-place Region Formation

To be able to investigate which parts of the reservoir that are injected by foam, CO_2 and water during different injection strategies, and also quantify the amount of injected volume into different parts, the reservoir is divided into regions. That way, it is possible to report the amount of injected volume into each region and report the amount of produced volume from each region. In total, the reservoir model was divided into 14 horizontal regions and 32 vertical regions.

The horizontal regions were primarily introduced to divide the reservoir model into distinct flow zones, to investigate the injection volume into each flow zone in the reservoir, which in turn could identify an injection pattern and sweep efficiency of foam. Based on the average permeability and pore volume of each of the 28 stratigraphic layers in the model and limiting values for flow potential, layers were separated into flow units and flow barriers. A layer was defined as a flow unit if the average layer permeability was over 0.015 mD and if the average layer pore volume was over 50 Mrb. Layers that were in vertical contact with each other, were further defined as a flow zone. Figure 9.2 shows the division of layers into 6 flow zones. and Based on these criteria, the following layers were defined as flow units, and the remaining layers were defined as flow barriers.

Layer	Average horizontal K (mD)	Average PV (Mrb)	
1	0.2	36	
2	0.9	621	Flow zone 1
3	0.5	520	
4	22.8	618	
5	0.9	182	
6	0.1	282	
7	1.3	981	Flow zone 2
8	126.9	1128	
9	0.4	229	
10	12.4	1.2	
11	1.2	914	
12	3.1	67	
13	0.5	573	
14	0.1	102	
15	1.8	677	Flow zone 3
16	14.8	431	
17	0.1	534	
18	2.0	1202	
19	10.8	1448	
20	0.1	803	
21	0	0	
22	2.4	1514	Flow zone 4
23	0.1	265	
24	6.7	2121	Flow zone 5
25	0	0	
26	1.6	47	
27	0.1	0	
28	1.4	468	Flow zone 6

FIGURE 7.6: Division of layers into 6 flow zones with 7 separating flow barriers in between.

Table 7.4 illustrates the average properties of permeability in x-direction (K), pore volume (PV), hydrocarbon volume (HCPV) and porosity (ϕ) for the 6 flow zones.

TABLE 7.4: Properties of the defined flow zones in the foam model

Flow zone	K (mD)	PV (Mrb)	HCPV (Mrb)	ϕ
1	3.5	539	404	0.07
2	13.4	1286	801	0.09
3	3.9	2730	1192	0.08
4	2.1	1114	426	0.07
5	5.8	2161	1093	0.10
6	1.3	90	39	0.03

After the flow zones and flow barriers were defined, they were introduces as separate fluid-in-place regions in the simulation data file. This was done by adding the EQUALS and FIPNUM keywords in the REGIONS section and the TABDIMS keyword in the GRID section. The EQUALS keyword assigned the value of a property for a region within the grid, whereas the FIPNUM keyword specified the number of fluid-in-place regions. 6 horizontal flow zones regions and 7 horizontal flow barrier regions were specified by the lower and upper x-, y- and z-coordinates of the grid cells included in each FIPNUM, in addition to an extra region (region 1), to assign a region for the grid blocks not included in the 13 regions. To request output of total gas injection volume in each region, the keyword RGIR was added in the SUMMARY section, in addition to the keyword RWIT for the total water injection volume in each region. The 6 flow zones are schematically shown for the cross-section L25-L14G-L32, in Figure 7.7.

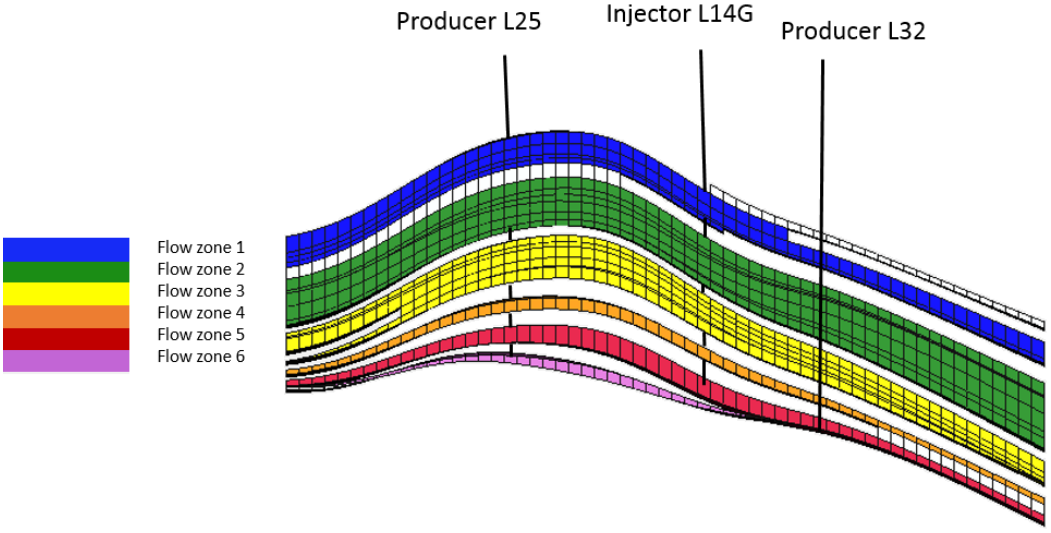

FIGURE 7.7: The 6 identified flow zones in the model, which was based on average permeability and pore volume for each layer.

In addition to horizontal regions, each flow zone is divided into 32 vertical regions to quantify the the gas saturation in each flow zone as a function of distance from injector L14G, to producer

L25 and L32. 14 vertical fluid-in-place regions were specified between L14G and L25, and 14 vertical fluid-in-place regions were specified between L14G and L32. The length (x-direction) was constant for all the regions and represented by one cell dimension in x-direction (50 ft), the width of each region (y-direction) was restricted to the width of the pilot pattern, which is approximately 1500 ft and the thickness of each region (z-direction) corresponded to the thickness of the flow zone. In addition to the 14 regions between each well pair, one region was specified along the well trajectory for L14G, and an extra region (region 1) was specified to assign a region for the grid blocks not included in the 32 regions. The flow zones are schematically shown from above, in Figure 7.8 with the pilot pattern demonstrated by the green shaded area.

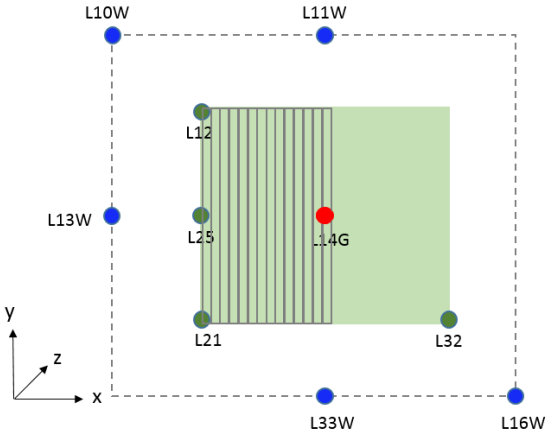

FIGURE 7.8: Vertical regions established between L14G and L25, and between L14G and L32, in the pilot pattern (green shaded area). The length of each region is 50 ft (x-direction), the width is 1500 ft (y-direction) and the thickness (z-direction) depends on the thickness of the respective flow zone.

7.4.3 Tracer Implementation

Pseudo tracers were set up in Eclipse to evaluate the breakthrough of CO_2 in the producers and the recycled volume of CO_2 and to quantify the sweep efficiency of CO_2 and water. By adding the keyword TRACER in the PROPS section of the data file, tracer associated with water (WT1) and CO_2 (GT1) was enabled. The units for the tracer amount correspond to the field unit of the model, (Mscf and STB). Additionally, the keyword TBLK was added in the SOLUTION section, to specify the initial tracer concentration for each grid block, which was zero. To request output of cumulative tracer production for each well, the keyword WTPT was added to the SUMMARY section, concatenated with the name for each tracer.

7.4.4 Grid Refinement for Sensitivity Analysis

To test the sensitivity of grid resolution on sweep development and gas gravity segregation, the model grid was refined in the z-direction, corresponding to a refinement of the thickness of each layers. This was done by selecting the local grid refinement (LGR) option in Eclipse,

which included adding the CARFIN and NZFIN keywords in the GRID section. The CARFIN specified a cartesian LGR in the foam model, with lower and upper x-, y- and z-coordinates to specify the grid cells included in the LGR. The NZFIN keyword specified the number of local cells in each global cell (each layer) of an LGR in Z-direction. It was determined that the new layer thickness in the refined grid should be approximately 5 ft. Because the layers varied in thickness, the division of each original layer depended on the original thickness of each layer. Based on the number of local cells in each layer, the grid refinement created a total of 84 horizontal layers. Table 7.5 shows the number of local cells in each layer of the LGR in Z direction.

TABLE 7.5: Number of local cells in each of the 28 layers in the z-direction.

Layer	1	2	3	4	5	6	7	8	9	10	11	12	13	14	15	16	17	18	19	20	21	22	23	24	25	26	27	28
Local cells	1	4	4	2	2	8	9	2	1	4	4	1	2	1	4	2	4	4	2	4	1	6	1	7	1	1	1	1

Because the foam model was initialized with pressures, saturations and compositions for each cell from the history matched CO_2 flood model, the new local cells in the foam model was assigned with values for pressure, saturations and compositions. Hence, to assign initial properties for all the cells in the LGR in the foam model, the same LGR had to be performed on the history matched CO_2 flood model first. After the CO_2 flood model was run with the LGR, the foam model with the LGR was subsequently initialized from the CO_2 flood model with LGR. The results of the grid resolution is presented in Appendix D.1.

Part III

Results & Discussion

8. Foam Performance

A model for the East Seminole field, built by Alcorn (2017) and Sharma (2017), has been used to simulate the performance of the foam field pilot L14. The main objective is to evaluate the CO_2 foam application for mobility control at the field scale and further evaluate sweep efficiency during foam injection.

The current chapter presents an evaluation of foam performance, compared to scenarios without foam. Screening of 11 different drainage strategies is performed to evaluate different recovery methods, and how they compared to foam. The screening identifies an optimal foam injection strategy in terms of CO_2 utilization for oil recovery, which is compared to a similar injection strategy without foam and pure CO_2 injection. Furthermore, foam performance is evaluated for two different scenarios: 1) an operation-time-limited scenario and 2) a CO_2-limited scenario. Because the mobility control by foam performance is assumed to influence sweep efficiency, this is evaluated thoroughly in chapter 9.

8.1 Screening of Injection Strategies

A range of different drainage strategies are evaluated in a screening process, to compare the performance of foam injection, CO_2 injection and WAG. Based on CO_2 utilization for oil recovery, the screening identified 3 cycle SAG with chase water as the optimal foam injection strategy. A response in BHP and injection rate during 3 cycle SAG compared to CO_2 injection and WAG, verified foam generation during 3 cycle SAG injection.

As mentioned in section 2.1, foam application for mobility control is expected to provide incremental oil recovery and reduced gas-oil-ratio (GOR), reduced CO_2 recycling and reduced CO_2 utilization compared to pure CO_2 injection and WAG. Thus, to evaluate different recovery methods, and how they compare to foam, a screening is conducted where the cumulative oil production, GOR, recycled CO_2 volume and CO_2 utilization factor are estimated for each of the evaluated strategies. The recycled CO_2 volume is defined as the produced volume of CO_2, from the start of injection. The CO_2 utilization factor is defined as the CO_2 volume injected under standard conditions, to produce a barrel of oil:

$$UF_{CO_2} = \frac{\text{injected volume of } CO_2}{\text{produced volume of oil}} \tag{8.1}$$

As a low CO_2 utilization factor corresponds to a high oil recovery, combined with a low consumption of CO_2, this is determined as the criteria for the optimal foam injection strategy.

As mentioned in chapter 7, the foam field pilot is scheduled for an operation period of 18 months, consisting of 6 months of foam injection, followed by 12 months of chase fluid injection.

Because the pilot injector L14G has injected CO_2 up until the start of foam implementation, a continuation of CO_2 injection is a representative base line for further evaluation. Based on the previous simulation cases created by Sharma (2017) and Alcorn (2017), there are three different injection strategies evaluated to achieve optimum mobility control foam: 3 cycle SAG, 6 cycle rapid SAG and co-injection. For the 3 cycle SAG, each cycle consists of a surfactant solution injection slug of 1 month, followed by a CO_2 injection slug of 1 month. For the 6 cycle SAG, each cycle consists of a surfactant solution slug of 15 days, followed by a CO_2 slug of 15 days. Because the latter SAG case requires a more rapid alternation of surfactant and CO_2 slugs, it is referred to as a rapid SAG.

The three foam injection strategies; 3 cycle SAG, rapid SAG and co-injection are compared to the base line continuous CO_2 injection. As the 3 cycle SAG and rapid SAG represents foam assisted WAG, these are also compared to two identical injection strategies of traditional WAG with water and CO_2. Additionally, to include a comparison of the chase fluid effect on SAG and WAG, each scenario is tested with chase CO_2 and chase water, which provides a total of 11 different simulation cases. To illustrate the injection strategy of the different cases that are evaluated, these are schematically presented with chase water, in Figure 8.1.

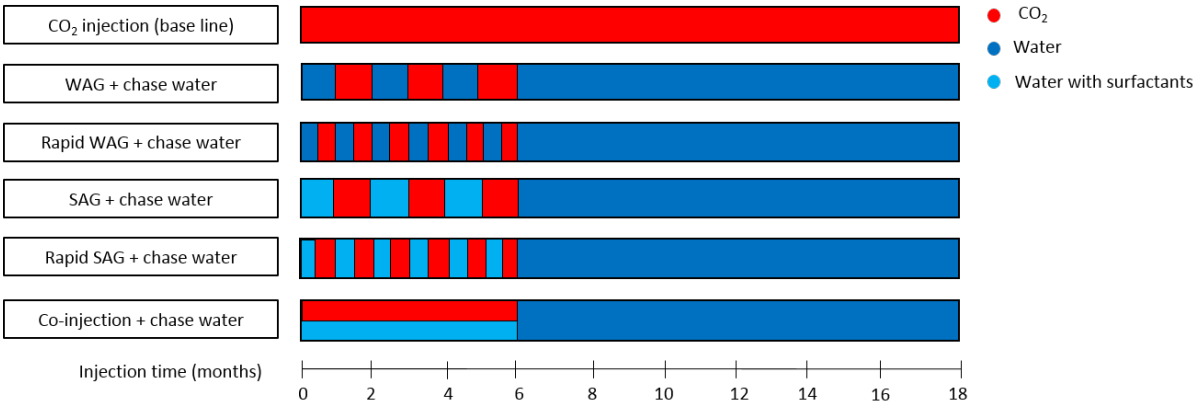

FIGURE 8.1: The timetable demonstrates the injection time of each water injection slug (blue), water injection slug with surfactant (light blue) and CO_2 injection slug (red color) for each injection strategy. In addition to the 5 strategies demonstrated with chase water injection, there are 5 similar strategies with chase CO_2 injection.

The screening of the different drainage strategies are shown in Table 8.1, with cumulative oil production, final GOR, recycled CO_2 volume and CO_2 utilization factor.

TABLE 8.1: Screening of different drainage strategies with chase CO_2 and chase water

Drainage strategy	Cumulative oil production (STB)	Final GOR (Mscf/STB)	Recycled CO_2 volume (Mscf)	CO_2 utilization factor (Mscf/STB)
CO_2 injection (base line)	35,800	16.3	129,209	30.2
WAG with chase CO_2	32,000	10.7	28,182	28.4
WAG with chase water	26,800	6.6	231	6.9
Rapid WAG with chase CO_2	38,600	14.5	143,719	25.0
Rapid WAG with chase water	30,100	6.1	5,947	8.0
SAG with chase CO_2	22,300	4.1	3,531	11.7
SAG with chase water	21,100	3.6	89	2.5
Rapid SAG with chase CO_2	23,100	4.3	4,830	12.3
Rapid SAG with chase water	21,800	3.6	219	3.3
Co-injection with chase CO_2	23,900	4.9	4,611	13.5
Co-injection with chase water	22,500	3.7	333	4.1

Based on the lowest CO_2 utilization factor (2.5 Mscf/STB), SAG with chase water was the most optimal foam injection strategy of the considered foam cases in Table 8.1. SAG with chase water also achieved the lowest GOR (3.6 Mscf/STB) and recycled CO_2 volume (89 Mscf) of all injection strategies. Compared to the base line, SAG with chase water reduced the CO_2 utilization factor by 27.7 Mscf/STB, reduced the GOR by 12.7 Mscf/STB and the recycled CO_2 volume by 129,120 Mscf. Compared to the identical injection strategy without surfactants (WAG with chase water), SAG reduced the CO_2 utilization factor by 4.4 Mscf/STB, the GOR by 3.0 Mscf/STB and the recycled CO_2 volume by 142 Mscf. However, SAG did not exceed the oil recovery for any of the injection strategies. The highest oil recovery by foam (23,900 STB) was achieved by co-injection with chase CO_2. Of all the 11 injection strategies with and without foam, the highest oil recovery (38,600 STB) was obtained by a rapid WAG with chase CO_2. None of the foam injection strategies were able to exceed the oil recovery of CO_2 injection or WAG. However, all the foam injection strategies achieved a reduced GOR compared to CO_2 injection and WAG. In terms of chase fluid, the oil production was higher for all cases with chase CO_2 relative to chase water. Correspondingly, the GOR, the recycled CO_2 volume and the CO_2 utilization factor was also higher for the cases with chase CO_2. It is apparent that the amount of injected CO_2 volume determines the production of oil, gas and CO_2 gas to a large extent. Of the cases using chase CO_2, SAG with chase CO_2 was the injection strategy that obtained the lowest GOR, lowest recycled volume CO_2 and lowest CO_2 utilization factor.

As mentioned in Chapter 4, foam generation is often demonstrated through an increase of injection pressure and/or decrease in injection rate, dependent of the control mode for injection. To verify foam generation during SAG with chase water, the BHP and injection rates for SAG are compared to CO_2 injection and WAG. The pilot injector L14G/W, was preset with a target

water volume rate (for L14W) and a target gas volume rate (for L14G) as primary control mode for injection. Additionally, the injector had a secondary control mode with a target BHP, in case the BHP limit was reached for the volume rate. The injection rates during SAG, WAG and CO_2 injection in L14W/G, are shown in Figure 8.2 and the corresponding BHP is shown in Figure 8.3.

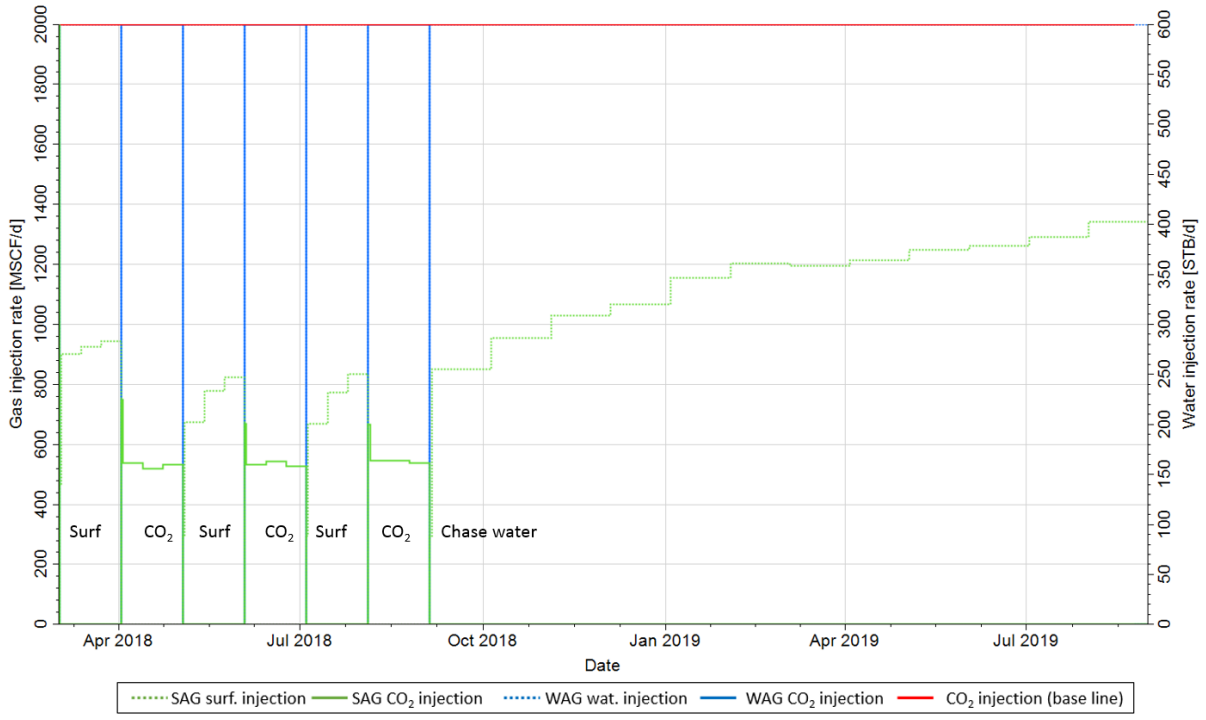

FIGURE 8.2: Injection rates in L14G/W for SAG during injection of surfactant solution (green dotted line) and gas (green solid line), for WAG during injection of water (blue dotted line) and gas (blue solid line) and for CO_2 injection base line (red solid line). The surfactant solution injection slugs (Surf) and CO_2 injection slugs (CO_2) for SAG are demonstrated in the figure, in addition to chase water injection. CO_2 injection and WAG had a constant injection rate, whereas SAG had a fluctuating injection rate.

The gas injection rate during the CO_2 injection base line and WAG (red and blue solid lines, Figure 8.2) held the target gas volume rate of 2000 Mscf/day. The water injection rate for WAG (blue line) maintained the target water volume rate of 600 STB/day during the water injection slugs and chase water injection. The surfactant solution injection slugs and CO_2 injection slugs during SAG showed a fluctuating injection rate. This shows that SAG switched over from constant injection volume rate, to the secondary injection control mode with a constant BHP due to a reached BHP limit. The pressure increase that lead to a control mode switch indicates that foam has been generated during SAG. The increase in water injection rate was higher during the first surfactant solution injection slug compared to the second and third, because the foam increased the resistance to inject water, which required a lower injection rate to maintain the target BHP. During the chase water injection, the injection rate increased from 250-400 STB/day. This is because foam propagated into the formation during chase water injection, which lead to a lower pressure near the injector, which in turn allowed for a higher injection

rate. It is a large difference in the gas injection rate for SAG (520 Mscf/day), compared to WAG and CO_2 injection (2000 Mscf/day), as well is the difference in surfactant injection rate and water injection rate for SAG (400 STB/day) and WAG (600 STB/day). The injectivity issues for SAG due to the pressure increase from foam generation, resulted in a considerably lower amount of injected CO_2 volume, which explains the moderate oil production shown in Table 8.1.

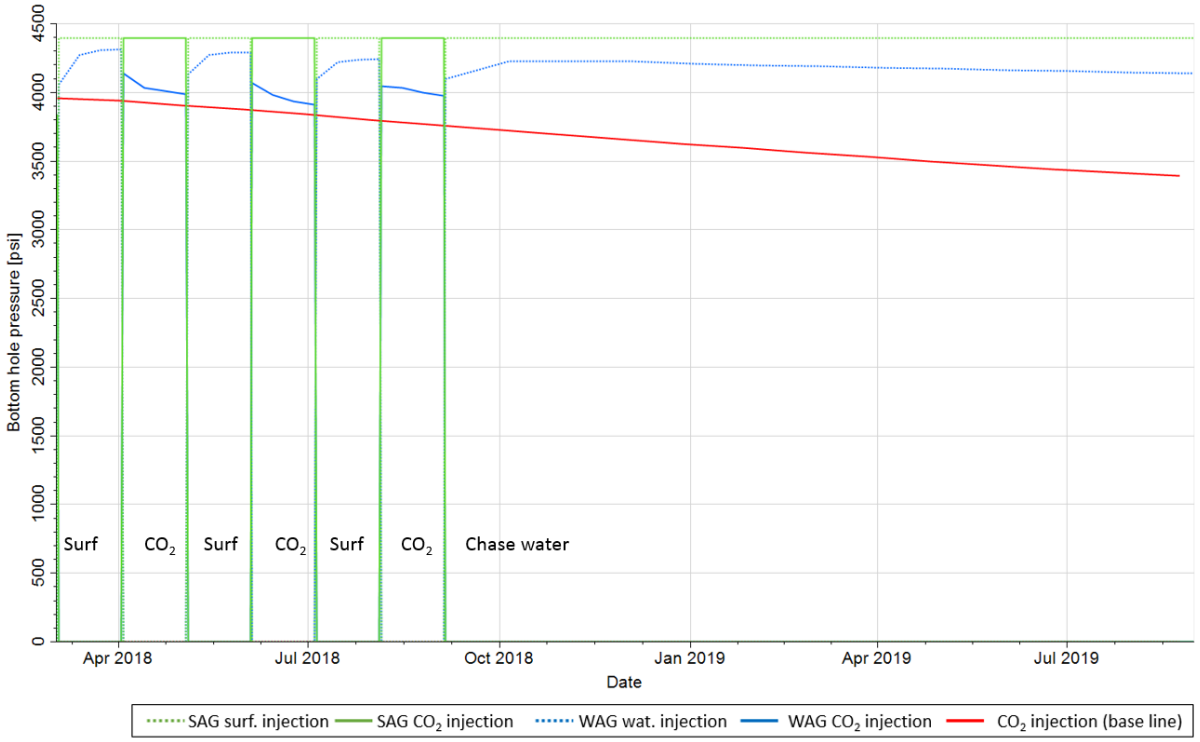

FIGURE 8.3: L14G/W BHP for SAG during injection of surfactant solution (green dotted line) and gas (green solid line), for WAG during injection of water (blue dotted line) and gas (blue solid line) and for CO_2 injection base line (red solid line). Corresponding to the injection rates in Figure 8.2, the BHP was constant during SAG and changed during CO_2 injection and WAG.

The BHP in L14G decreased during CO_2 injection and WAG (red and blue solid lines, Figure 8.3), as a response to the constant gas injection rate showed in Figure 8.2 To remain a constant water volume injection rate during the injection of water for WAG, the BHP in L14W increased and stayed just below the BHP limit of 4400 psia. During chase water injection for WAG, the BHP increased initially, before it started to decrease gradually. The BHP curve for SAG, shows an immediate increase in the BHP during the first surfactant solution injection slug, which indicates that foam was generated immediately and caused the pressure to reach the BHP limit, 4400 psia. SAG injection then held this target BHP, which shows that the injection switched from target rate control to target BHP control, correspondingly to Figure 8.2.

To conclude the main findings of this section, a screening of different drainage strategies showed that all the evaluated foam injection strategies reduced the CO_2 utilization for oil recovery, the GOR and the recycled CO_2 volume relative to pure CO_2 injection and WAG. However, they failed to increase the oil recovery over CO_2 injection and WAG. All cases with chase

water achieved a better performance in CO_2 utilization, GOR and CO_2 recycling, compared to chase CO_2. SAG with chase water was assessed as the most optimal foam injection strategy in terms of CO_2 utilization for oil recovery, in addition to attaining the lowest GOR and recycled CO_2 volume. SAG reduced the CO_2 utilization factor by 27.7 and 4.4 Mscf/STB relative to CO_2 injection and WAG, and in addition to a reduction of 12.7 and 3.0 Mscf/STB in GOR and 129,120 Mscf and 142 Mscf in reduced CO_2 recycling. A low injection rate and a high, constant BHP for SAG, verified that foam was generated immediately during the first surfactant solution injection rate for SAG. The low injection rate for SAG also indicated injectivity issues in achieving the same injected volume as the CO_2 injection and WAG. The foam performance of 3 cycle SAG with chase water is further evaluated, and compared to WAG and CO_2 injection in section 8.2.1.

8.2 Foam Performance

The foam performance of SAG with chase water from section 8.1, is evaluated further in this section, compared to CO_2 injection and WAG. The foam performance is evaluated for two different scenarios: 1) an operation-time-limited scenario and 2) a CO_2-limiting scenario. For an operation-time-limited scenario, production data showed a less cumulative oil production for SAG than for CO_2 injection and WAG at an equal time of injection, due to a significant difference in injected CO_2 and water volume. For an equal pore volume injected, the cumulative oil production for SAG exceeded the oil production for CO_2 injection and WAG. Production data also showed a delayed breakthrough of CO_2 due to mobility control by foam. For a CO_2-limiting scenario, the CO_2 injection base line was limited to 3 months CO_2 injection to obtain an equal CO_2 utilization limit as for WAG, whereas SAG was extended to 10 cycles for a corresponding CO_2 utilization. For this scenario, the oil recovery was lower for CO_2 injection and higher for extended SAG, compared to the previous 3 cycle SAG, as a result of less CO_2 injected for the CO_2 injection and more CO_2 injected, more foam and more effective mobility control for SAG.

8.2.1 Foam Performance During an Operation-time-limited scenario

An operation-time-limited scenario is important for consideration because the foam pilot project is scheduled and supported for a limited operation period of 18 months. The three drainage strategies evaluated for this scenario is SAG, WAG and CO_2 injection base line from section 8.1, which are illustrated in Figure 8.4.

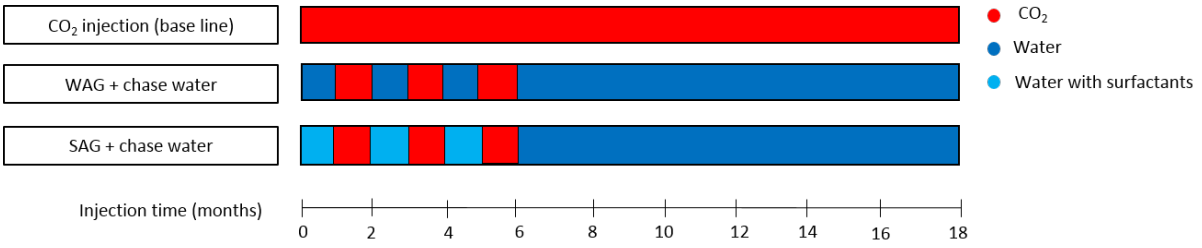

FIGURE 8.4: Injection time of the selected drainage strategies for foam performance comparison during an operation-time-limited scenario, including SAG, WAG and CO_2 injection as base line.

To provide an overview of the considered field pilot area, the pilot pattern and the peripheral water injectors are schematically shown in the figure below.

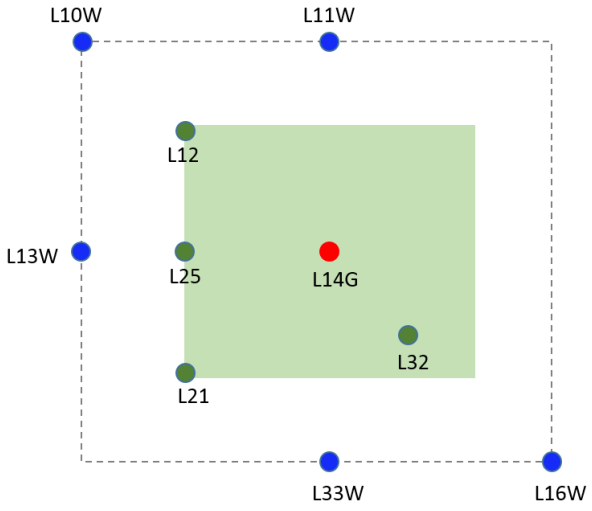

FIGURE 8.5: The considered field pilot area with pilot pattern (green shaded area) consisting of injector L14G and producers L12, L21, L25 and L32, in addition to peripheral water injectors outside of the pilot pattern.

The cumulative oil production, gas injection, reservoir volume injection and GOR for the considered field pilot area during SAG, WAG and CO_2 injection in L14G, are presented to evaluate the oil production and GOR relative to the amount of injected CO_2 and water.

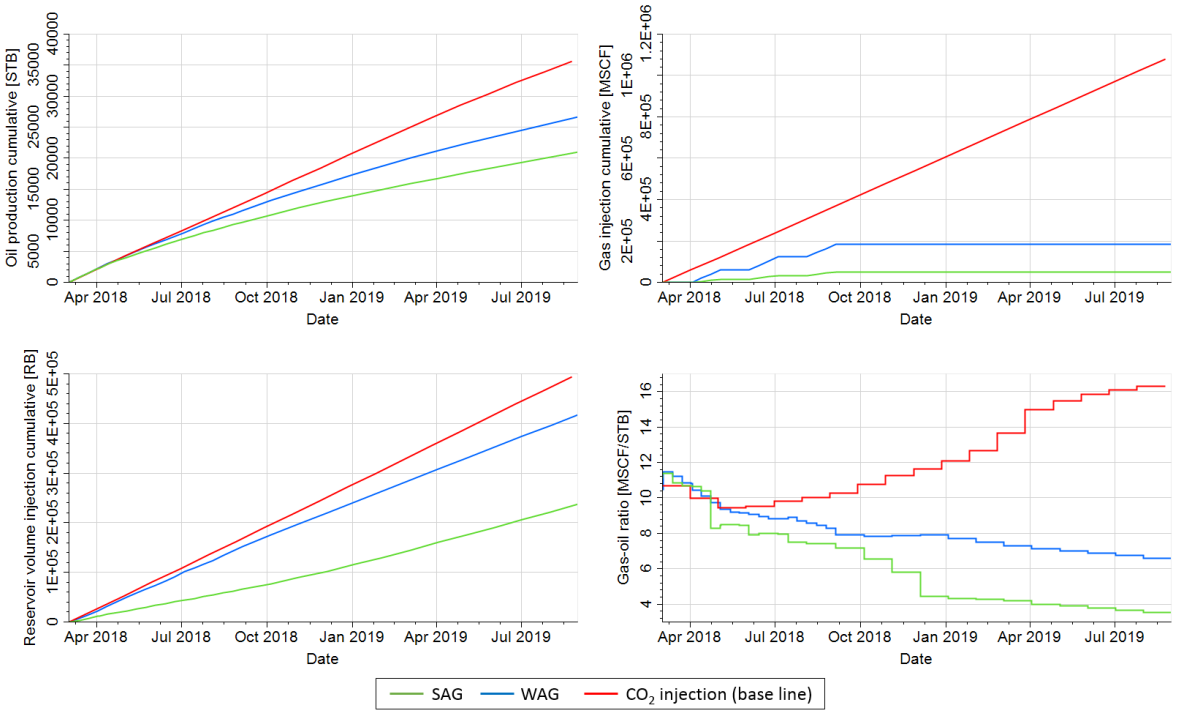

FIGURE 8.6: Cumulative oil production (upper left), cumulative gas injection (upper right), cumulative reservoir volume injection (lower left) and GOR (lower right) for the field during SAG (green), WAG (blue) and CO_2 injection (red). A high injection volume of CO_2 and water with correspondingly high oil production and GOR was demonstrated for base line, whereas SAG had a modest CO_2 and water injection, as well as oil production and GOR.

The cumulative oil production for the field pilot area (upper left image in Figure 8.6) was highest for CO_2 injection (35,800 STB) compared to WAG (26,800 STB) and SAG (21,100 STB). Simultaneously, the cumulative injected CO_2 volume (upper right, Figure 8.6) for CO_2 injection (1200 MMscf) was significantly larger than for WAG (188 MMscf) and especially SAG (53 Mscf). Cumulative CO_2 injection highlighted the injectivity issues with foam due to significant pressure increase during foam generation. The cumulative reservoir volume injection (lower left, Figure 8.6), also demonstrated a large difference in the injected volume of CO_2 and water combined, during the base line (496,260 rb), WAG (419,580 rb) and SAG (239,070 rb), which followed from the difference in injection slugs and injection rates for CO_2 and water. The difference in gas injection and reservoir volume injection for WAG and SAG compared to CO_2 injection, affects the slopes of incline in oil production, but also the slope of decline in GOR (lower right, Figure 8.6). Initially, the GOR was similar for the three scenarios, however, as more CO_2 were injected during base line, the GOR increased (16.6 Mscf/STB) relative to WAG (6.6 Mscf/STB) and SAG (3.6 Mscf/STB). This indicates that the considerable difference in GOR was due to the variation in injected CO_2 volume, which was also discussed in section 8.1 when strategies with chase water reduced the GOR relative to chase CO_2.

It is obvious that there is a connection between high oil production and a large injected volume of CO_2, and because the injected CO_2 volume and reservoir volume differ considerably for the

three injection strategies, it is difficult to separate the effect of foam and the effect of injected CO_2 on oil production. To account for the difference in injection volume, the cumulative oil production is compared as a function of pore volume injected (PVI) by CO_2 and water combined, in Figure 8.7. One pore volume is defined as the total pore volume of the model, corresponding to approximately 19 MMrb.

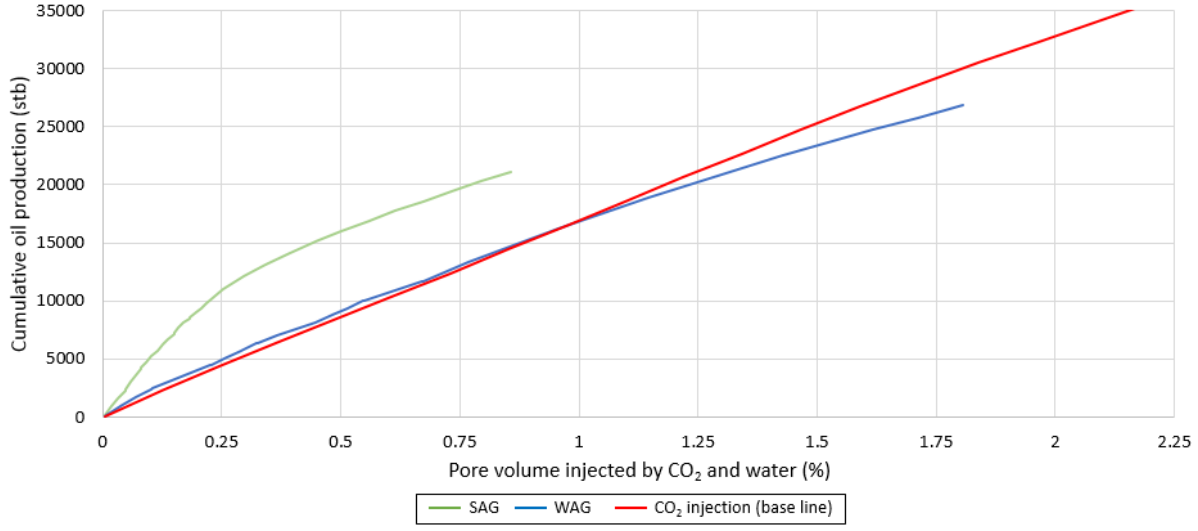

FIGURE 8.7: Cumulative oil production for CO_2 injection (red), WAG (blue) and SAG (green) as a function of the percentage of PVI by CO_2 and water combined, shows that the production of SAG exceeds the production of CO_2 injection and WAG.

Final cumulative oil production by CO_2 injection (red line in Figure 8.7) was higher than for WAG and SAG. However, when comparing oil production for different PVI, it is evident that SAG attained the highest production: for example, at 0.75% PVI, the oil production by SAG was 19,500 STB, compared to 12,700 STB for WAG and 12,600 STB for CO_2 injection. The increase in barrels is lower compared to the foam field pilot in the literature review in chapter 5 due to a considerably shorter injection period. However, the increase corresponds to a 54 and 55% increase compared to CO_2 injection and WAG, which indicates an efficient improvement in oil recovery. SAG maintained a higher recovery than WAG and CO_2 injection throughout the entire injection process. This might be a result of reduced CO_2 mobility and a more favorable mobility ratio between CO_2 foam and displaced oil, that reduced viscous fingering and increased the stability and efficiency of the oil displacement. Furthermore, SAG may have displaced oil in unswept zones of lower permeability, as a result of increased sweep efficiency.

As the CO_2 utilization factor for SAG in section 8.1 was as low 2.5 Mscf/STB compared to 4.4 and 30.2 Mscf/STB for WAG and CO_2 injection, it is interesting to investigate if the reduction is due to the moderate injection volume of CO_2 or due to increased efficiency in oil production by foam. By schematically demonstrating the oil production as a function of PVI by CO_2 alone, one evaluate how much the injected CO_2 in SAG, WAG and CO_2 injection contribute to oil recovery, which is shown in Figure 8.8.

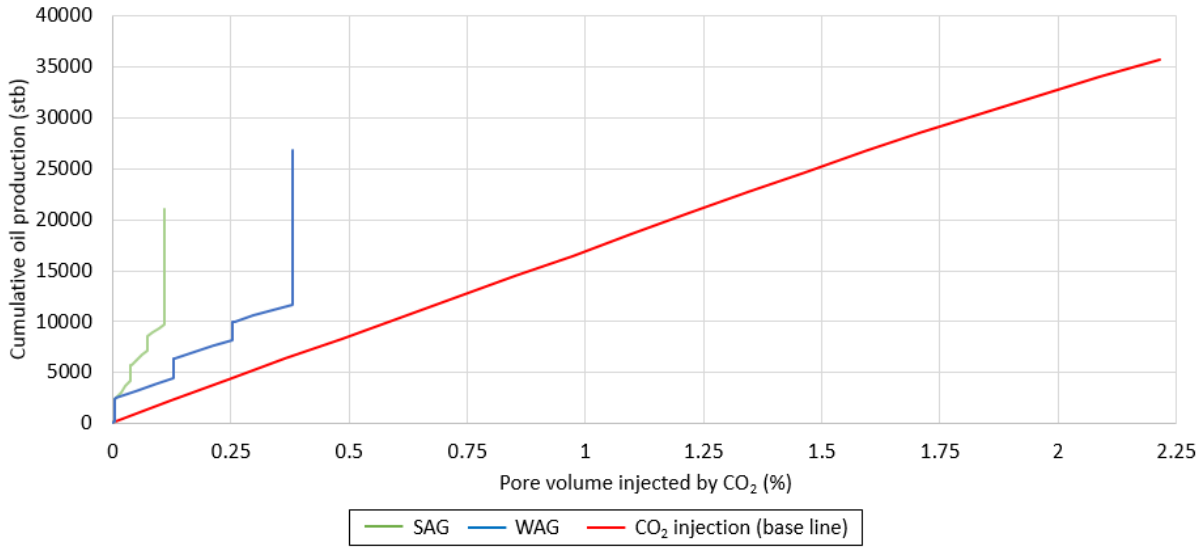

FIGURE 8.8: Cumulative oil production as a function of the percentage of PVI by CO_2 for CO_2 injection (red), WAG (blue) and SAG (green) shows that SAG is most efficient in recovering oil.

The oil production for SAG (green line, Figure 8.8) had the steepest incline compared to CO_2 injection and WAG, when comparing oil recovery for different PVI by CO_2 alone. The increase in oil production was higher for SAG and WAG than for CO_2 injection, due to the alternating cycles of aqueous slugs and CO_2 slugs. The aqueous slugs provided an increased oil production without utilizing as much CO_2 volume as the CO_2 injection base line, which explains the low CO_2 utilization in the calculated CO_2 utilization factor. However, by comparing the increase in oil production for SAG and WAG, it is apparent that SAG was more efficient in recovering oil. SAG injected a considerably less volume of CO_2 and water as WAG due to injectivity issues, yet the oil production was higher for every PVI by CO_2 during SAG. This affirms that mobility control by foam is effective during SAG and that the low CO_2 utilization factor for SAG is due foam performance and not only a moderate injection volume of CO_2.

Incremental oil recovery and reduced GOR for SAG compared to CO_2 injection and WAG verifies mobility control by foam during SAG. A CO_2 tracer was introduced in the model to further evaluate foams efficiency in reducing recycled CO_2 volume and delaying CO_2 breakthrough by mobility control. Breakthrough of CO_2 was only observed in producer L25 and L32, which is shown logarithmic as a function of PVI by CO_2 in Figure 8.9.

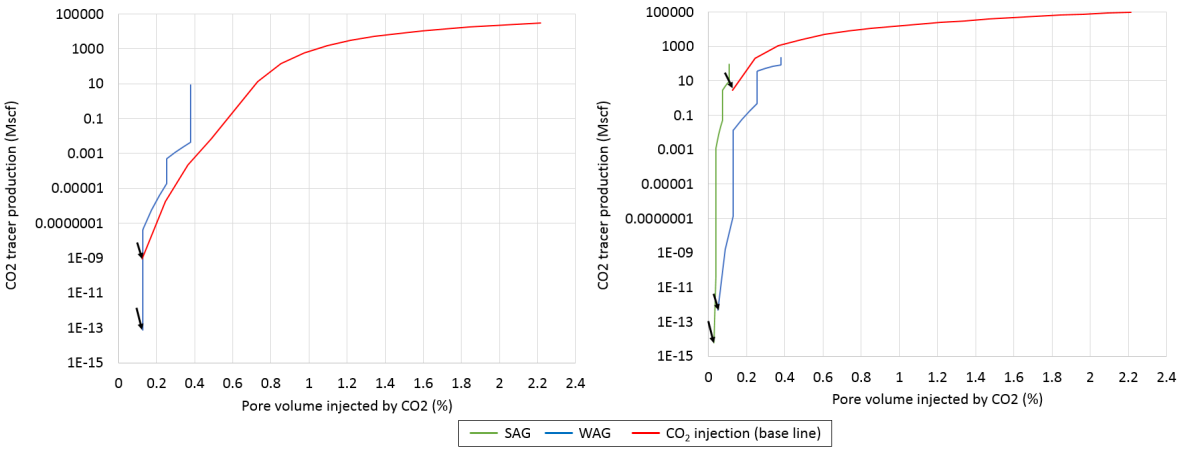

FIGURE 8.9: Cumulative production of CO_2 in producer L25 (left) and L32 (right) and breakthrough time of CO_2 for CO_2 injection (red), WAG (blue) and SAG (green), indicated by black arrows. The highest CO_2 production volume was shown for CO_2 injection and breakthrough in L25 was delayed for SAG.

The breakthrough of CO_2 in producer L25 (left image, Figure 8.9), indicated by black arrows, occurred for the same PVI percentage for WAG and CO_2 injection. CO_2 did not breakthrough in L25 during SAG, which may indicate CO_2 mobility reduction compared to WAG and CO_2 injection. Breakthrough in L32 (right image), occurred first for SAG, which shows that mobility reduction for CO_2 flow towards L32 is not as efficient as for flow towards L25. The difference in produced CO_2 volume during CO_2 injection (100,000 Mscf) and SAG (100 Mscf) shows a significant effect of foam performance on mobility control for flow towards L32. The delayed breakthrough in L25 and the reduced recycled CO_2 volume in L32 may also indicate foam generation in high permeability streaks, and increasing sweep efficiency by diverting chase water to layers of lower permeability with considerable oil saturation.

To conclude the evaluation of foam performance during an operation-time-limited scenario, cumulative oil production, gas injection, reservoir volume injection and GOR was evaluated for the considered field pilot area, in addition to oil production as a function of PVI and PVI by CO_2 alone. The production of CO_2 and breakthrough time was also compared for SAG, WAG and CO_2 injection in producer L25 and L32. Based on the evaluation conducted, foam was observed to produce less oil than CO_2 injection and WAG for an equal time of injection due to a significant difference in injected volume of CO_2. For an equal PVI, cumulative oil production for SAG exceeded the oil production for CO_2 injection and WAG. The comparison of oil production as a function of PVI by CO_2 alone, the low CO_2 utilization factor for SAG, was shown to be a result of an efficient displacement of oil due to foam. Evaluation of breakthrough time and production of CO_2 as a function of PVI by CO_2, showed no breakthrough of CO_2 in L25 for SAG in contrast to CO_2 injection and WAG and a reduced CO_2 volume in producer L32 compared to CO_2 injection and WAG. Conclusively, foam performance by SAG is affirmed to achieve mobility control and a following incremental oil recovery, reduced GOR, reduced CO_2 utilization factor and delayed breakthrough and recycling reduction of CO_2.

8.2.2 Foam Performance During a CO_2-limited scenario

Similarly to the foam evaluation in section 8.2.1, SAG, WAG and CO_2 injection are compared during a CO_2-limited scenario. It is beneficial to evaluate foam performance for two different scenarios because foam application may be relevant from different point of views. As the injected CO_2 for the foam pilot project is purchased, and one of the main targets for CO_2 foam application is a reduced CO_2 utilization, a CO_2-limited scenario is reasonable. For this scenario, an alternative relation between SAG, CO_2 injection and WAG is established, where the injection strategies are modified to have an equal CO_2 utilization limit. Foam performance evaluation in this section showed that the oil recovery was lower for CO_2 injection and higher for extended SAG with equal CO_2 utilization, compared to the CO_2 injection and SAG in the operation-time-limited scenario.

It is important to separate CO_2 utilization from the CO_2 utilization factor, as the former corresponds to injected CO_2 volume and the latter represents injected CO_2 volume over producer oil volume. The injection strategy for the CO_2 injection base line and SAG from section 8.2.1, were modified to have an equal CO_2 utilization as WAG (188 MMscf), which established two new drainage strategies:

- 3 months CO_2 injection
- Extended SAG

The extended SAG comprised of 10 cycles that were similar to the cycles of the previous SAG and also comprised of 12 months of chase water. The extended SAG required a total of 20 months to inject an approximate volume of CO_2, as WAG. With an addition of 12 months of chase water, the extended SAG injection was not relevant for an 18 months operation-time-limited scenario. Nevertheless, it was only introduced to evaluate the performance of SAG with equal CO_2 utilization as CO_2 injection and WAG. To achieve the most comparable relationship between CO_2 injection, WAG and SAG, the 3 months CO_2 injection is followed by 15 months of water injection, which corresponds to the aqueous injection slugs and chase water injection for WAG and SAG. As the 3 months CO_2 injection with 15 months water injection represents a modified base line scenario, it is referred to as the reference case. Furthermore, because the 3 cycle SAG with chase water is assessed as the optimal foam injection strategy in terms of CO_2 utilization for oil recovery, this is continuously compared to the 3 cycle WAG, the 3 months CO_2 reference case and the extended SAG.

The injection strategy of the four scenarios that will be evaluated next, is illustrated in Figure 8.10 as a function of injection time.

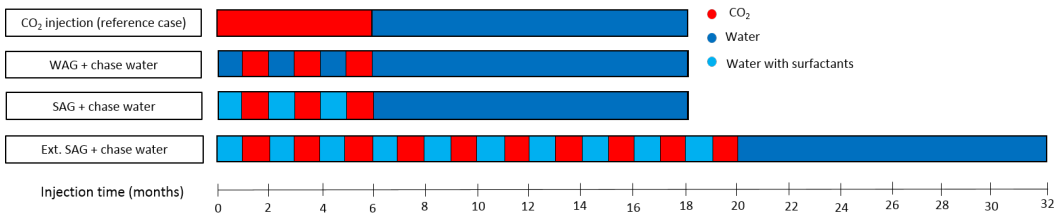

FIGURE 8.10: The timetable demonstrates the injection time of each water injection slug (blue), water injection slug with surfactant (light blue) and CO_2 injection slug (red) during a 3 months CO_2 injection, WAG, SAG and extended SAG.

The cumulative oil production, cumulative gas injection, reservoir volume injection and GOR for the considered field pilot area during the CO_2 reference case, WAG, extended SAG and SAG, are presented in Figure 8.11 to evaluate the oil production and GOR relative to the amount of injected CO_2 and water.

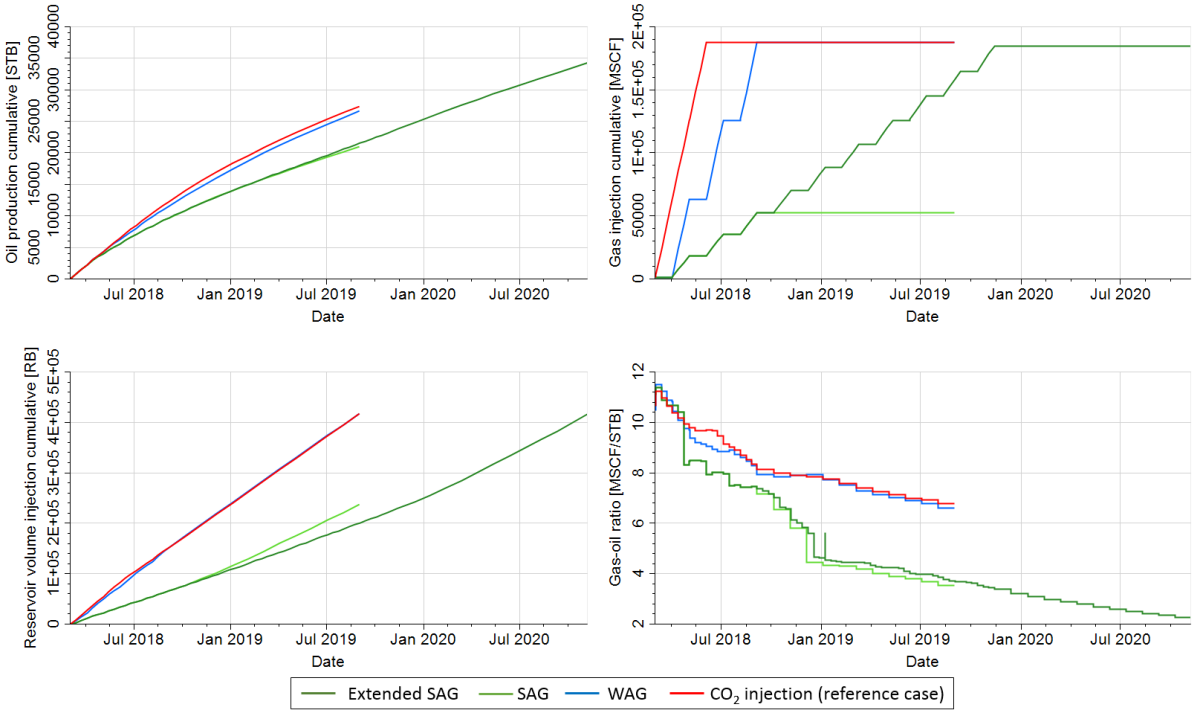

FIGURE 8.11: Cumulative oil production (upper left), cumulative gas injection (upper right), reservoir volume injection (lower left) and GOR (lower right) for SAG (green), extended SAG (dark green), WAG (blue) and CO_2 reference case (red). Production curves show an incremental oil production and reduced GOR for extended SAG, compared to the other injection strategies.

After complete injection of CO_2 cycles and a following chase water injection, the oil production (upper left image in Figure 8.11) was observed to be highest for the extended SAG with total of 34,400 STB (oil production WAG: 26,700 STB, CO_2 reference case: 27,500 STB, SAG: 21,100 STB). The incremental oil production from extended SAG relative to the production for the CO_2 reference case and WAG, was assumed to be a result of improved sweep efficiency, influenced by CO_2 foam mobility control. The reduction in GOR (lower right, Figure 8.11) for extended SAG verify a reduced gas mobility and may indicate blocking of high permeability zones by

foam. The GOR for extended SAG decreased further in time compared to SAG, due to a longer operation period. The GOR for extended SAG and SAG reduced equally at the beginning of injection. SAG and extended SAG had identical GOR development until 6 months of injection, when SAG was introduced to chase water injection, which reduced GOR for SAG additionally. In January, the extended SAG had a rapid jump, before it continued to decrease gradually. The jump was a result of a jump in gas production rate in L32 which occurred simultaneously to a jump in oil production, which may be due to an arrived oil front with a following foam bank with CO_2 behind.

To evaluate and compare the oil recovery of each drainage strategy for different PVI, the cumulative oil production for the CO_2 reference case, WAG, SAG and extended SAG are shown in Figure 8.12. An overview of the number of cycles injected at each pore volume, is shown for each drainage strategy in Appendix B.1, in addition to an overview of the percent of pore volume injected by CO_2 during each CO_2 slug.

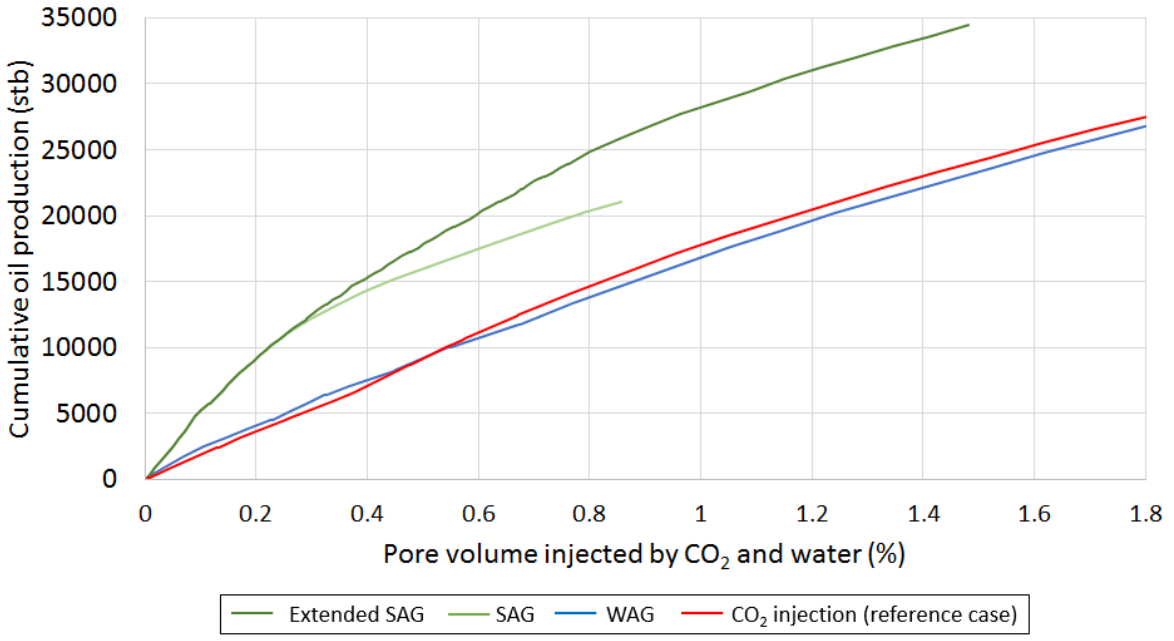

FIGURE 8.12: Cumulative oil production of the CO_2 reference case (red), WAG (blue), SAG (green) and extended SAG (dark green) as a function of percent of PVI by CO_2 and water combined.

When comparing oil recovery for different PVI, the extended SAG had the highest oil recovery for all PVI after 0.3% PVI: for example, at 0.85% PVI, the cumulative oil production by extended SAG was 25,800 STB, compared with 14,800 STB for WAG, 15,600 STB for CO_2 reference case and 21,100 STB for SAG. This corresponds to a Correspondingly, this shows that by applying SAG or extended SAG, one may injected a smaller pore volume than for the CO_2 reference case and WAG, and achieve the same oil recovery, due to reduced CO_2 mobility and perhaps increased sweep efficiency. A smaller injected pore volume may be beneficial in terms of operating costs and CO_2 purchase costs. The increase in oil production for SAG gradually stagnates in contrast

to extended SAG during chase water injection. This might indicate foam destabilization during chase water injection, as a result of increased water saturation and decreased gas saturation and surfactant concentration. As described in section 4.5.3 and section 4.5.1, foam quality and foam stability, which control foam strength and mobility reduction, is expected to decrease with decreasing gas fraction and surfactant concentration. This indicates that the foam performance is weakened during chase water injection, which influences the recovery performance.

To evaluate the CO_2 utilization factor for SAG and extended SAG compared to the CO_2 reference case and WAG, Table 8.2 shows the CO_2 utilization factor for each drainage strategy.

TABLE 8.2: CO_2 utilization factor for the CO_2 reference case, WAG, SAG and extended SAG

Drainage strategy	CO_2 utilization factor (Mscf/STB)
CO_2 injection (reference case)	6.8
WAG	7.0
SAG	2.5
Extended SAG	5.4

The result in Table 8.2, demonstrates that SAG had the lowest CO_2 utilization factor of all four injection strategies. However, SAG did not have the same CO_2 utilization, meaning that the inject CO_2 volume was less than the other strategies. For an equal CO_2 utilization, the extended SAG achieved the lowest CO_2 utilization factor (5.4 Mscf/STB), compared to the reference case (6.8 Mscf/STB) and WAG (7.0 Mscf/STB). This is due to the incremental oil recovery from CO_2 mobility reduction and perhaps due to blocking of high permeability streaks and sweep improvement. Essentially, this demonstrates that foam performance during a CO_2-limited scenario, reduce the CO_2 utilization factor by 1.4 and 1.6 Mscf/STB relative to the CO_2 reference case and WAG.

Similar to the operation-time-limited scenario, the CO_2 production volume is evaluated to investigate how efficient the foam during the extended SAG is in reducing recycled CO_2 volume and possibly delaying CO_2 breakthrough by mobility control. Breakthrough of CO_2 was only observed in producer L25 and L32, which is shown logarithmic as a function of PVI by CO_2 in Figure 8.13.

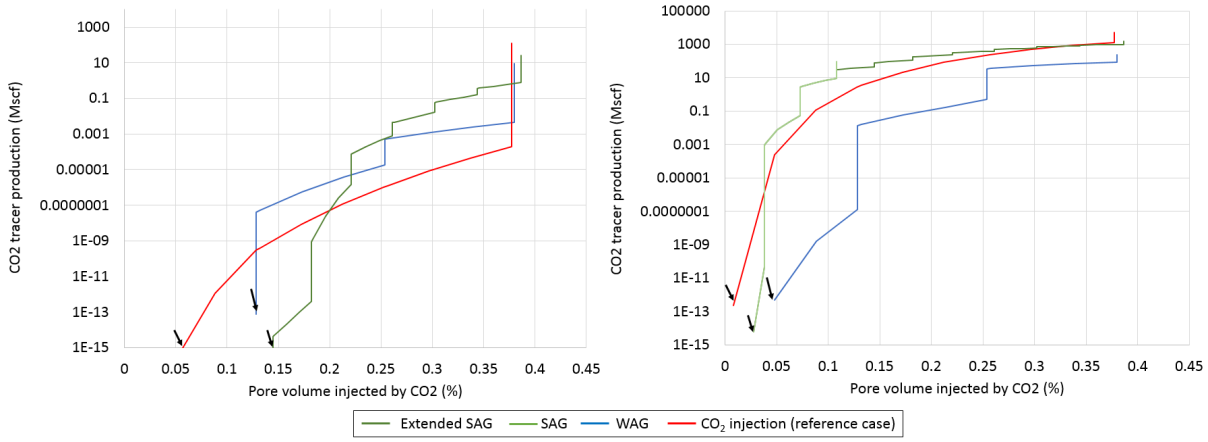

FIGURE 8.13: Cumulative production of CO_2 in producer L25 (left) and L32 (right) and breakthrough time of CO_2 for CO_2 reference case (red), WAG (blue), SAG (green) and extended SAG, indicated by black arrows. The highest CO_2 production volume was shown for CO_2 injection and breakthrough in L25 and L32 was delayed for SAG.

The breakthrough of CO_2 in producer L25 (left image, Figure 8.9) and L32 (right image), occurred first for the CO_2 reference case. The cumulative CO_2 production was also highest for the CO_2 reference case after completed cycles and chase water injection for all cases. Despite a delayed breakthrough of CO_2 in L25 for extended SAG compared to WAG, extended SAG produced slightly more CO_2 than WAG cumulatively. In L32, extended SAG and SAG experienced an earlier breakthrough than WAG, and the extended SAG produced cumulatively more CO_2 than WAG for this producer as well. The reason for this might be the long injection period for the extended SAG (32 months) compared to WAG (18 months). Additionally, the extended SAG injected a larger volume of water during the 10 SAG cycles, compared to the 3 cycles for WAG, which may have displaced the CO_2 and caused a higher production volume.

In conclusion, for foam performance evaluation during a CO_2-limited scenario, two new injection strategies were introduced to obtain the same CO_2 utilization as WAG; the CO_2 reference case (3 months CO_2 injection with 15 months chase water), and the extended SAG (10 cycle SAG with 12 months chase water). As for the operation-time-limited scenario, the foam performance was evaluated in terms of cumulative oil production, gas injection, reservoir volume injection and GOR. Additionally, the oil production was investigated as a function of PVI, in addition to an evaluation of CO_2 utilization factor and recycled CO_2 production. The results showed a higher oil production for extended SAG compared to the CO_2 reference case, WAG and SAG. The final GOR for extended SAG was also lowest relative to the other injection strategies. When comparing oil production for different PVI, the extended SAG and SAG exceeded oil production for CO_2 reference case and WAG, which resulted in a better CO_2 utilization factor for SAG and extended SAG. A stagnation in oil production for SAG during chase water injection compared to extended SAG, indicated foam destabilization due to increased water saturation and decreased gas saturation. Evaluation of CO_2 production showed a delayed breakthrough and reduced recycling of CO_2 for extended SAG in L25 and L32 compared to CO_2 injection. However, the extended SAG produced a higher cumulative CO_2 volume than WAG.

The current chapter has presented an evaluation of foam performance compared to scenarios without foam. Based on a screening of different injection strategies, SAG with chase water was evaluated as the most optimal foam injection strategy in terms of a low CO_2 utilization factor for oil recovery. This was further evaluated by comparisons to WAG and CO_2 injection during an operation-time-limited scenario and by comparisons to WAG, extended SAG and a CO_2 reference case during a CO_2-limited scenario. For both scenarios, mobility control by foam performance was verified through an increased oil recovery compared to CO_2 injection and WAG, for an equal PVI. Additionally, the foam mobility control lead to a reduction in GOR, recycled CO_2 and a reduced CO_2 utilization factor compared to the injection strategies without foam. Because the mobility control is assumed to influence sweep efficiency, the sweep efficiencies for SAG, extended SAG, WAG and the CO_2 reference case are evaluated in chapter 9.

9. Sweep Efficiency

From the evaluation of foam performance in chapter 8, mobility control was verified for SAG and extended SAG by comparisons to a CO_2 reference case and WAG. This chapter presents an evaluation of sweep efficiency during SAG and extended SAG, which are compared to the CO_2 reference case and WAG. Initially, injection patterns for L14G/W are investigated by streamline simulation and production data, with a further evaluation of CO_2 sweep pattern in high-permeable layers. Additionally, sweep efficiency is evaluated by gas saturation profiles and sweep efficiency quantification.

For convenience, injector L14G/W will be referred to as L14G. From the results of this chapter, streamline simulation identified an injection pattern from L14G to all four producers, and indicate an early breakthrough in L32. Injection fractions and production fractions indicated a well established contact and injection pattern between L14G and L25, and between L14G and L32. Evaluation of the 28 layer model, showed large contrasts in permeability and porosity in 6 modified layers, where 3 of these were shown to be primary thief zones for CO_2 flow based on observed channeling in the L25-L14G-L32 cross-section. The three thief zone layers were evaluated in terms of areal sweep pattern, which indicated a relatively similar gas saturation for SAG, extended SAG and the CO_2 reference case after completed injection of CO_2, and a diversion of chase water for SAG and extended SAG due to foam generation. After dividing the reservoir into flow zones and flow barriers, 6 flow zones where identified. 3 main flow zones with high average permeability, were shown to receive a majority of the injected CO_2. These main flow zones were further investigated through gas saturation profiles, where dynamic flow zones showed diversion of chase water from the main flow zones to flow zones of lower permeability. Quantification of sweep efficiency also demonstrated an increased sweep efficiency of water during chase water injection for SAG and extended SAG, as a result of diversion from high-permeability flow zones.

9.1 Injection Pattern Identification

To analyze the sweep of CO_2 and CO_2 foam in the field pilot area, the injection pattern for L14G is identified during SAG, WAG and the CO_2 reference case discussed in chapter 8. In this section, the injection pattern is identified by evaluating time-of-flight (TOF) along streamlines, evaluating injection and production fractions from streamline simulation and by monitoring the response in production of oil, gas and water for each production well.

TOF's from streamline simulation identified an injection pattern from L14G to all four producers, with shortest TOF's along streamlines towards producer L32, which indicate an early breakthrough in L32. Transmissibility modifications from history match of CO_2 flood was also apparent to affect the injection pattern. Injection fractions and production fractions indicated

a well established contact and an injection pattern between L14G and L25, and between L14G and L32. Cumulative production of oil, gas and water corresponded to streamline pattern, injection fraction and production fractions, in that a response to SAG and extended SAG was observed in l25 and L32 during foam injection in L14G.

9.1.1 Injection Pattern by Streamline Simulation

From section 8.2.1 and section 8.2.2, breakthrough of CO_2 in producer L25 and L32 suggested an injection pattern from L14G to producer L25 and L32. This is investigated further by streamline simulation, which was described in section 6.5. The streamlines, which are essentially curves that are locally tangential to a velocity field, represent the direction of flow from the injector. The injection pattern from L14G has been identified by streamlines through computation of TOF's, injection fractions and production fractions.

As explained in section 6.5, the TOF's represent the travel time (in days) of a neutral tracer along streamlines from the injector to producers, and may be related to the breakthrough time of CO_2 tracer in the model: short TOF's near production wells may indicate a more rapid breakthrough of CO_2 and water. Figure 9.1 illustrates the time-of-flight in a network of streamlines, representing the injection pattern for all injectors during a SAG.

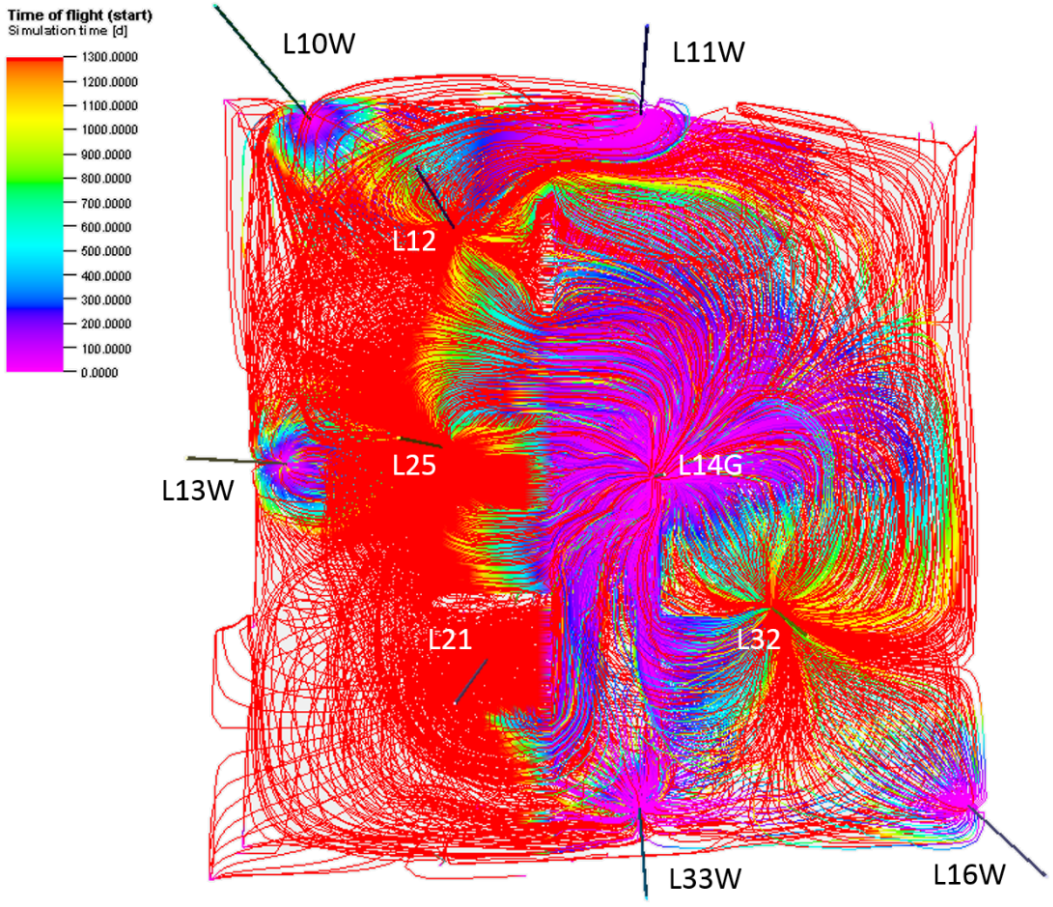

FIGURE 9.1: Injection pattern for injector L10W, L11W, L13W, L14G, L33W and L16W in the field, based on time-of-flight (TOF) along streamlines during a SAG. Short TOF's which may indicate short breakthrough times, are pink and blue, whereas long TOF's are red and yellow.

The injection pattern for L14G (Figure 9.1) approached all four producers. Short TOF's (pink and blue) appear close to L32, which indicate earlier breakthrough in L32. This corresponds to the CO_2 production shown in section 8.2.1 and section 8.2.2, where L32 experienced the earliest breakthrough. Additionally, the injection pattern identified flow from injector L10W and L11W towards producer L12, and from from injector L16W towards L32, from L33W towards L21 and l32 and flow from L13W to L25. The TOF's show how the direction of flow for the injected fluids were affected by the incorporated transmissibility barriers around producer L12, L21 and L25 and between L14G and L32, which were introduced to achieve a good match on liquid production volume for CO_2 history match. The gas production was unfortunately not matched, nevertheless, transmissibility barriers impeded the gas flow from L14G which caused underestimation of gas flow from L14G to the producers. As the injection pattern by TOF's was similar for SAG, extended SAG, WAG and the CO_2 reference case, the flow barriers are expected to affect all cases equally.

Injection fractions for L14G and production fractions for each producer during SAG, WAG and the CO2 reference case was calculated by streamlines. The injection fractions for L14G, represent the fraction of total volume injected, that contributes to reservoir volume production

in each producer. The production fractions represent the fraction of reservoir volume production in a producer, that is compensated by an injector or a present aquifer. Injection fractions and production fractions for SAG, WAG and the CO_2 reference case, were similar to each other. Hence, the fractions are only visualized for SAG in Figure 9.2 and Figure 9.3.

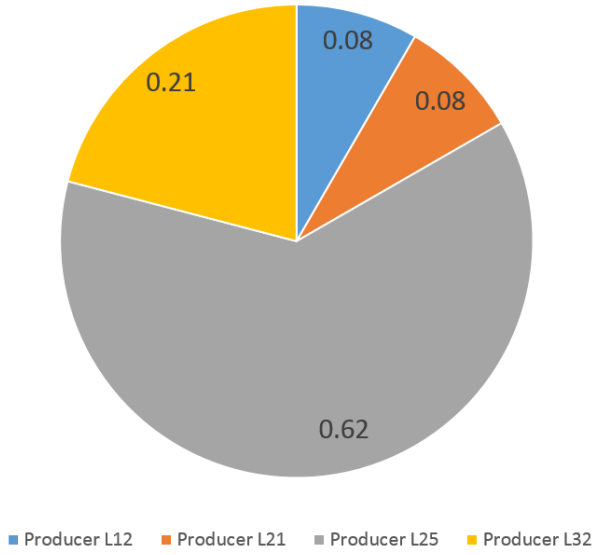

FIGURE 9.2: Injection fractions for L14G to producer L12 (blue), L21 (orange), L25 (grey) and L32 (yellow) during SAG. The fractions indicate a good established contact between L14G and L25 (grey) and between L14G and L32 (yellow).

During SAG, 62% of injected volume in L14G (grey color in Figure 9.2) supported the reservoir volume production in L25, and 21% supported the reservoir volume production in L32 (yellow). This indicates an injection pattern between L14G-L25 and L14G-L32, which correspond to the streamline pattern. For the CO_2 reference case (64.4% to L25 and 22.8% to L32) and WAG (67.4% to L25 and 18.5% to L32), the injection fractions were similar to each other. Distribution of injection fractions for L14G corresponded to the results in section 8.2.1 and section 8.2.2, where CO_2 breakthrough occurred in L25 and L32. The CO_2 production and injection fractions indicate a well established contact between the well pair L14G-L25 and L14G-L32, which in turn suggests a dominant sweep pattern between these well pairs.

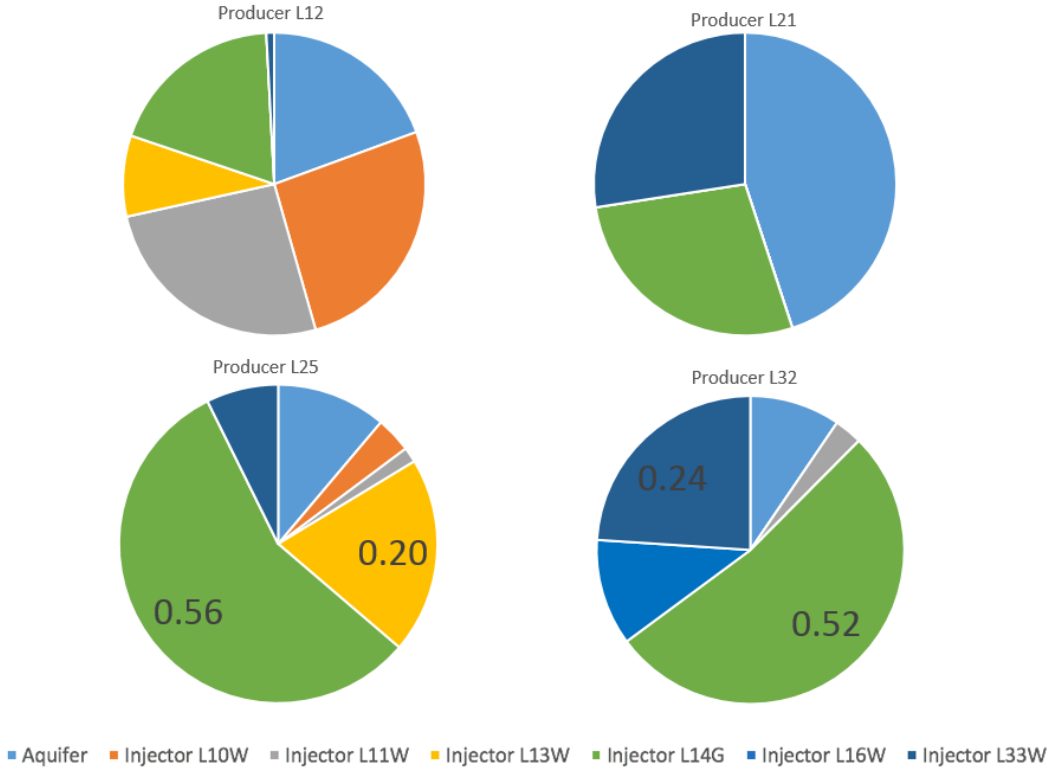

FIGURE 9.3: Production fractions for producer L12 (upper left), L21 (upper right), L25 (lower left) and L32 (lower right) during SAG. The fractions indicate a high production fraction for L14G (green) in producer L25 and L32.

The production fractions correspond to the identified injection pattern from streamlines and injection fraction. The reservoir volume production in producer L25 during SAG (lower left pie chart in Figure 9.3) was shown to be mainly compensated by injection from L14G (56.4%, green color) and also by injected water from L13W (19.9%, yellow color). This was expected as these are the closest injectors to L25. Reservoir volume production in L32 (lower right pie chart) was mainly compensated by injection from L14G (52.4%, green color) and L33W (24.0%, navy color). The production fractions for the CO_2 injection (75.4% from L14G and 6.8% from L33W) and WAG (79.4% from L14G and 5.9% from L33W), were similar to SAG, expect L14G contributed more, and L33W contributed less for CO_2 injection and WAG. This may due to high CO_2 mobility, which increase the injection fraction for L14G compared to CO_2 foam during SAG. Correspondingly, L32 received a higher production from L14G and a lower production from L13W during CO_2 injection (64.7% from L14G and 12.3% from L13W) and WAG (60.1% from L14G and 14.7% from L13W) compared to SAG. Distribution of production fractions was in agreement with the injection fractions for L14G (Figure 9.2 and breakthrough of CO_2 in section 8.2.1 and section 8.2.2.

To confirm the established contact between L14G-L25 and L14G-L32, the production from all producers are investigated in section 9.1.2.

9.1.2 Injection Pattern by Production Well Response

As described in chapter 7, all injectors in the model were set with constant injection rates during SAG, WAG and CO_2 injection, to be able to only observe a change in production as a function of L14G. To evaluate the contact between L14G and each producer, the cumulative production of oil, gas and water were evaluated for L12, L21, L25 and L32 during SAG, extended SAG, WAG and the CO_2 reference case. Due to a similar trend in production for oil, gas and water, the oil production is shown in Figure 9.4, whereas the cumulative production for gas and water are shown in Appendix C.1.

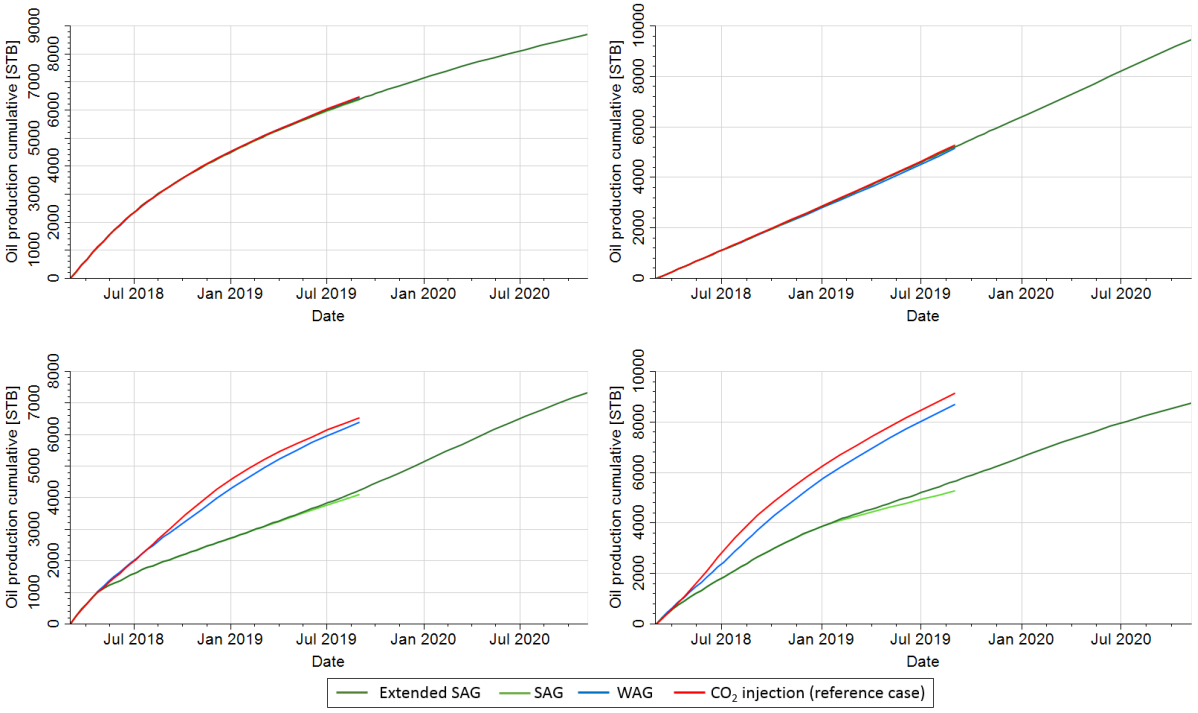

FIGURE 9.4: Cumulative oil production for producer L12 (upper left), L21 (upper right), L25 (lower left) and L32 (lower right), showing a response to different injection strategies in oil production from L25 and L32.

The cumulative oil production in producer L12 and L21 (upper left and upper right image, in Figure 9.4) was unaffected by the different drainage strategies applied in L14G. Producer L25 and 32 (lower left and lower right image, in Figure 9.4), experienced a reduced oil production during SAG and extended SAG, due to the low injectivity during foam injection. The response in L25 and L32 confirms the identified injection pattern between the respective well pairs. The cumulative production of hydrocarbon mixture gas in Appendix C.1 (Figure C.1) followed a similar trend as oil production, whereas production of water (Figure C.2) changed in producer L12, L25 and L32 for SAG and extended SAG compared to the CO_2 reference case and WAG. This may indicate that foam injection in L14G during SAG and extended SAG, altered the sweep pattern for water, which altered the production of water in L12, L25 and L32.

To summarize the results of this section, injection pattern from L14G during SAG extended SAG, WAG and the CO_2 reference case were identified by TOF's along streamlines, injection and production fractions and cumulative well production of oil, gas and water. Streamlines showed an injection pattern from l14G towards all producers. Short TOF's were observed close to L32, indicating an early breakthrough in L32. Injection and production fractions indicated a strong connection between injection in L14G and production in L25 and L32. Cumulative well production of oil and gas, for producer L25 and L32, also demonstrated an injection pattern between L14G-L25 and L14G-L32, based on sensitivity to different injection strategies in L14G. The results corresponded to CO_2 production from section 8.2.1 and section 8.2.2, where L25 and L32 experienced breakthrough.

To evaluate the sweep development by foam injection further, the vertical and areal sweep patterns are visualized in section 9.2.

9.2 Visualization of CO_2 Sweep Efficiency

This section evaluated the properties of the 28 layers in the reservoir model and visualizes the CO_2 sweep to evaluate vertical and areal CO_2 sweep development during foam injection, compared to the CO_2 reference case and WAG.

Evaluation of the layer properties, showed large contrasts in permeability and porosity in 6 modified layers, where high-permeability layers 4, 8 and 16 were observed as main thief zones for CO_2 flow, based on gas channeling in the L25-L14G-L32 cross-section. The high-permeability layers were also evaluated in terms of areal sweep pattern, which indicated a relatively similar gas saturation for SAG, extended SAG and the CO_2 reference case after completed injection of CO_2, whereas WAG achieved a lower gas saturation. Based on a low reduction in gas saturation after chase water injection for SAG and extended SAG, chase water was assumed to be diverted to layers of lower permeability due to foam generation.

The reservoir model represents an extremely heterogeneous reservoir system and the vertical and areal CO_2 sweep will differ for each defined layer in the model. To emphasize the effect of heterogeneity on the gas sweep, the 28 layers of the model are discussed below. The degree of heterogeneity in permeability and porosity of each layer is shown in Figure 9.5 and Figure 9.6 for all active layers. Layers 21, 25 and 27 are inactive layers based on a minimum pore volume of 1 Mrb and a minimum vertical permeability of 0.05 mD defined in the model.

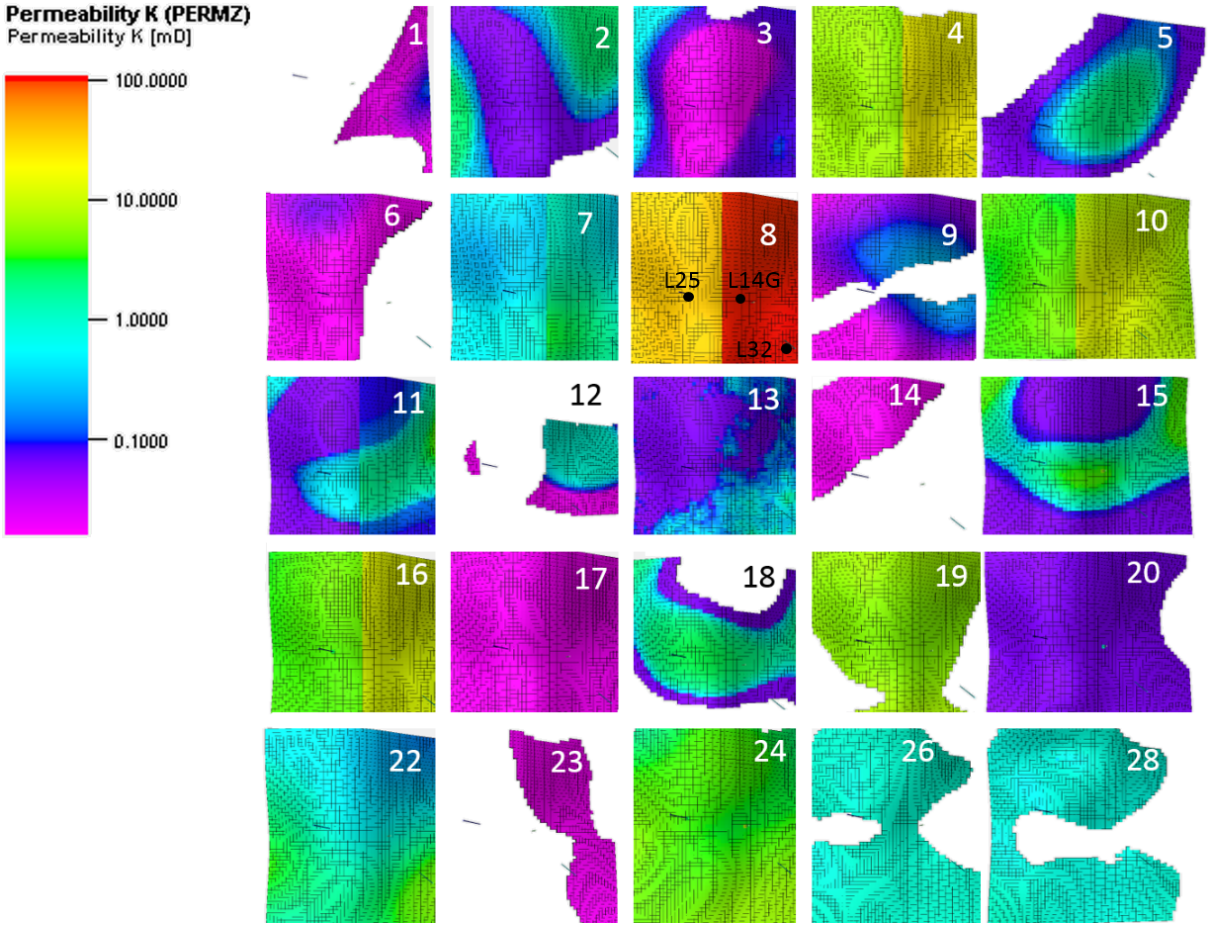

FIGURE 9.5: Permeability contrasts of the layers in the field pilot model. The white area indicates inactive cells due to values below minimum vertical permeability (0.05 mD) and porosity (1 Mrb). The location of injector L14G, producer L25 and L32, is demonstrated in permeability layer 8.

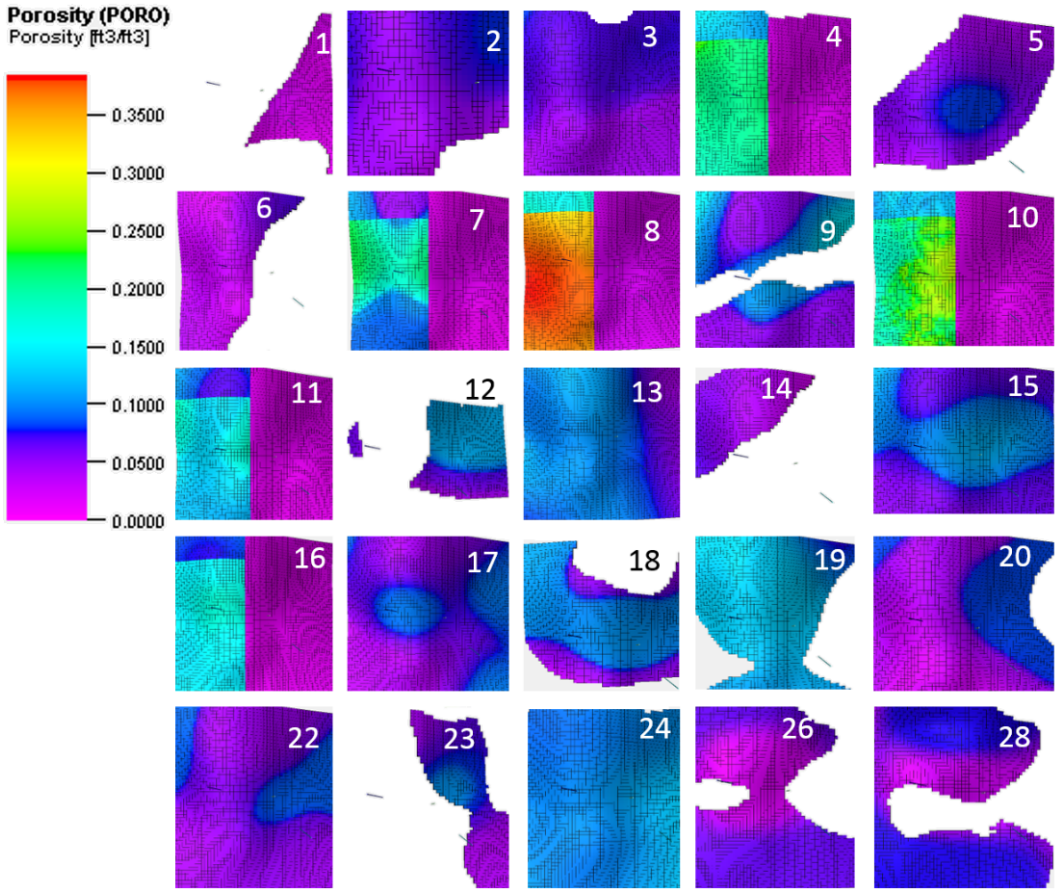

FIGURE 9.6: Porosity contrasts of the layers in the foam pilot model, shows a high contrast in the same layers with high permeability contrast in Figure 9.5.

Layers 4, 7, 8, 10, 11 and 16 were manually modified during history matching, with high contrasts in permeability and porosity (Sharma, 2017). The layers were altered in such a manner that the east region has a considerably low porosity and a high permeability, whereas the west region has a high porosity and a relatively high permeability. The reasons for these changes and the expected effect on reservoir performance was explain in section 7.3.2. Because layer 4, 8 and 16 have the highest average permeabilities ($K_{average}$) and porosities (ϕ_{average}) (Table 9.1), the injected fluids are expected to flow mainly in these layer.

TABLE 9.1: Maximum and average permeability and porosity for layer 4, 8 and 16

Layer	K_{max} (mD)	$K_{average}$ (mD)	ϕ_{max}	ϕ_{average}
4	19.6	13.7	0.20	0.09
8	108.0	76.2	0.37	0.15
16	12.6	8.9	0.15	0.06

Due to a high permeability in the east region of layer 4, 8 and 16, these layers were expected to receive more flow compared to other layers. To investigate, the vertical CO_2 sweep development is shown for a cross-section in section 9.2.1.

9.2.1 Vertical Sweep Development

To study the vertical CO_2 sweep development of injected CO_2 foam from L14G, the cross-section through L14G is examined (see Figure 9.7). Although producer L32 is not located parallel to L14G-L25, the cross-section is referred to as the L25-L14G-L32 cross-section, due to the assumption of a well established contact between L14G and L32. Because the vertical sweep pattern was relatively similar for SAG, extended SAG, WAG and the CO_2 reference case, only the vertical sweep for SAG is illustrated below.

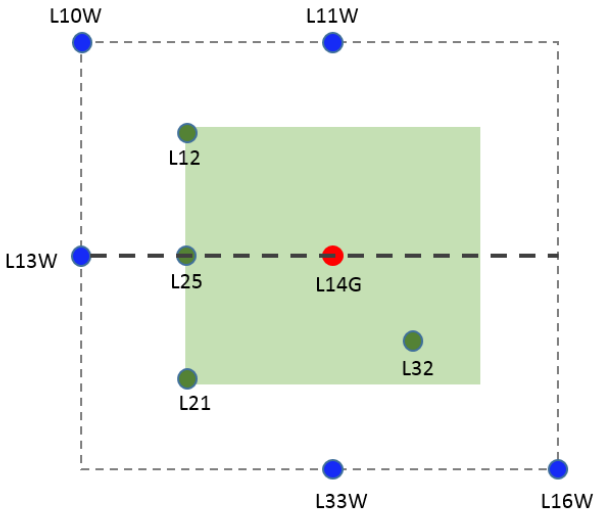

FIGURE 9.7: Location of the examined cross-section L25-L14G-L32, in the extended pilot area of the foam model.

The vertical CO_2 sweep along the cross-section, has been visualized by gas saturation. It was difficult to observe the change in saturation for vertical sweep due to the high gas saturation in the reservoir prior to foam injection.

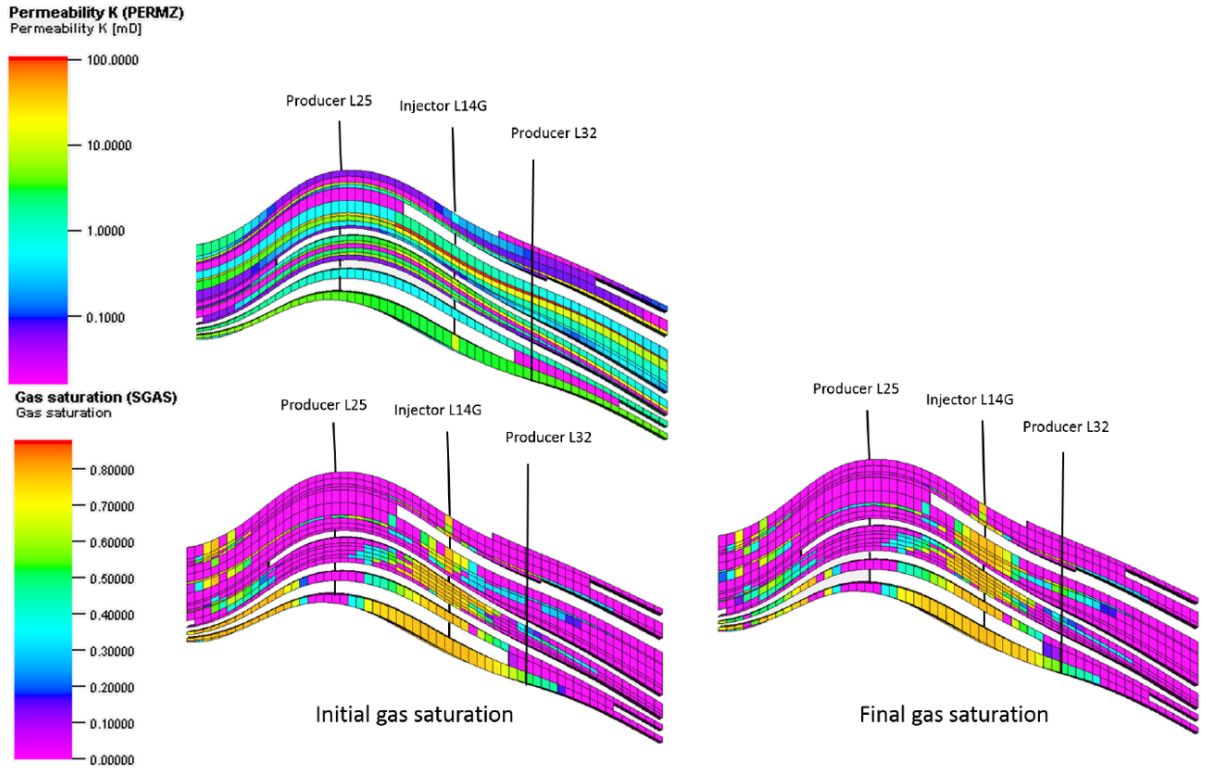

FIGURE 9.8: Vertical gas saturation sweep before (lower left) and after SAG (lower right), with the corresponding permeability distribution (upper left) for the cross-section L25-L14G-L32. Due to high gas saturation in the reservoir prior to foam injection, it is difficult to observe the change in gas sweep.

It was easier to observe a gas sweep pattern by visualizing the CO_2 tracer volume compared to gas saturation, as the tracer volume was initially zero. Figure 9.9 shows the final CO_2 sweep by CO_2 tracer volume, after SAG.

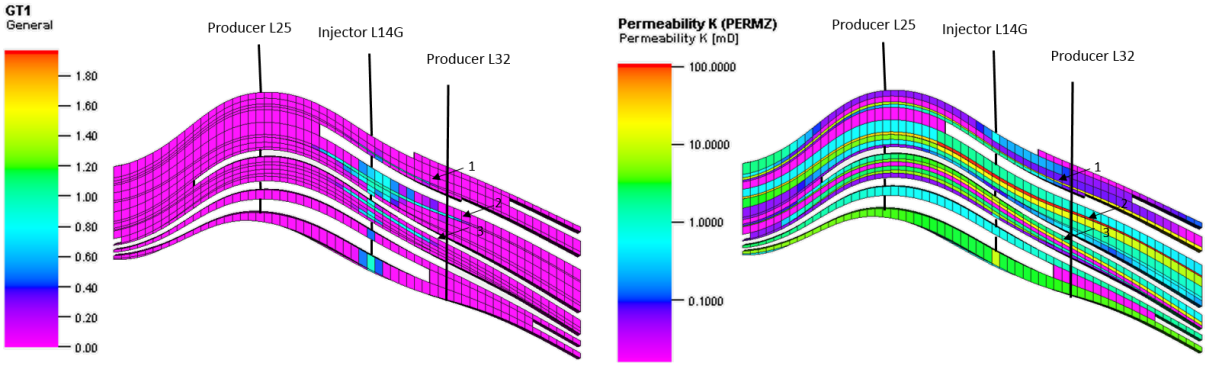

FIGURE 9.9: Vertical sweep efficiency of CO_2 after SAG, in terms of CO_2 tracer volume (left), with the corresponding permeability distribution (right). The legend shows the unit of CO_2 tracer volume for CO_2 tracer GT1, which is Mscf of CO_2.

The CO_2 injected from L14G (left cross-section in Figure 9.9) demonstrated three distinct thief zones for CO_2, which corresponds to layers 4, 8 and 16. This indicates that injected CO_2 foam preferred the high-permeability layers, which is expected, as high permeability allows for high initial gas saturation, which in turn lead to more rapid generation of foam compared

to low permeability layers with oil saturation that diminish foam stability. If SAG follows expectations and generate high quality foam in high-permeability layers 4, 8 and 16 was, any chase fluid should be diverted from these layers to layers of lower permeability.

To investigate if the chase water after SAG, was diverted from layer 4, 8 and 16 after foam generation, the areal CO_2 sweep development in the three layers is evaluated in section 9.2.2 for SAG, extended SAG, WAG and CO_2 reference case.

9.2.2 Areal Sweep Development

The areal CO_2 sweep development in layer 4, 8 and 16 is visualized before and after chase water injection for SAG, extended SAG, WAG and the CO_2 reference case, to verify if foam performance enables diversion of fluids from high-permeability layers to layers of lower permeability, and improves sweep efficiency. The CO_2 sweep development is evaluated in terms of gas saturation change and CO_2 tracer volume.

The change in gas saturation from initial conditions, to the completed injection of CO_2 and the completed chase water injection for the CO_2 reference case, WAG, SAG and extended SAG is shown in Figure 9.10. The location of the cross-section L25-L14G-L32 is shown in the initial gas sweep pattern for the CO_2 reference case, together with the current water injectors L13W, L33W and L11W that injected CO_2 during the CO_2 flood from 2013 to 2017. The observed gas saturation evaluation was relatively similar for layer 4, 8 and 16, only one layer is shown below. Because layer 8 had the largest sweep, this is shown below, whereas layer 4 and 16 are shown in Figure C.3 and Figure C.4 in Appendix C.2.

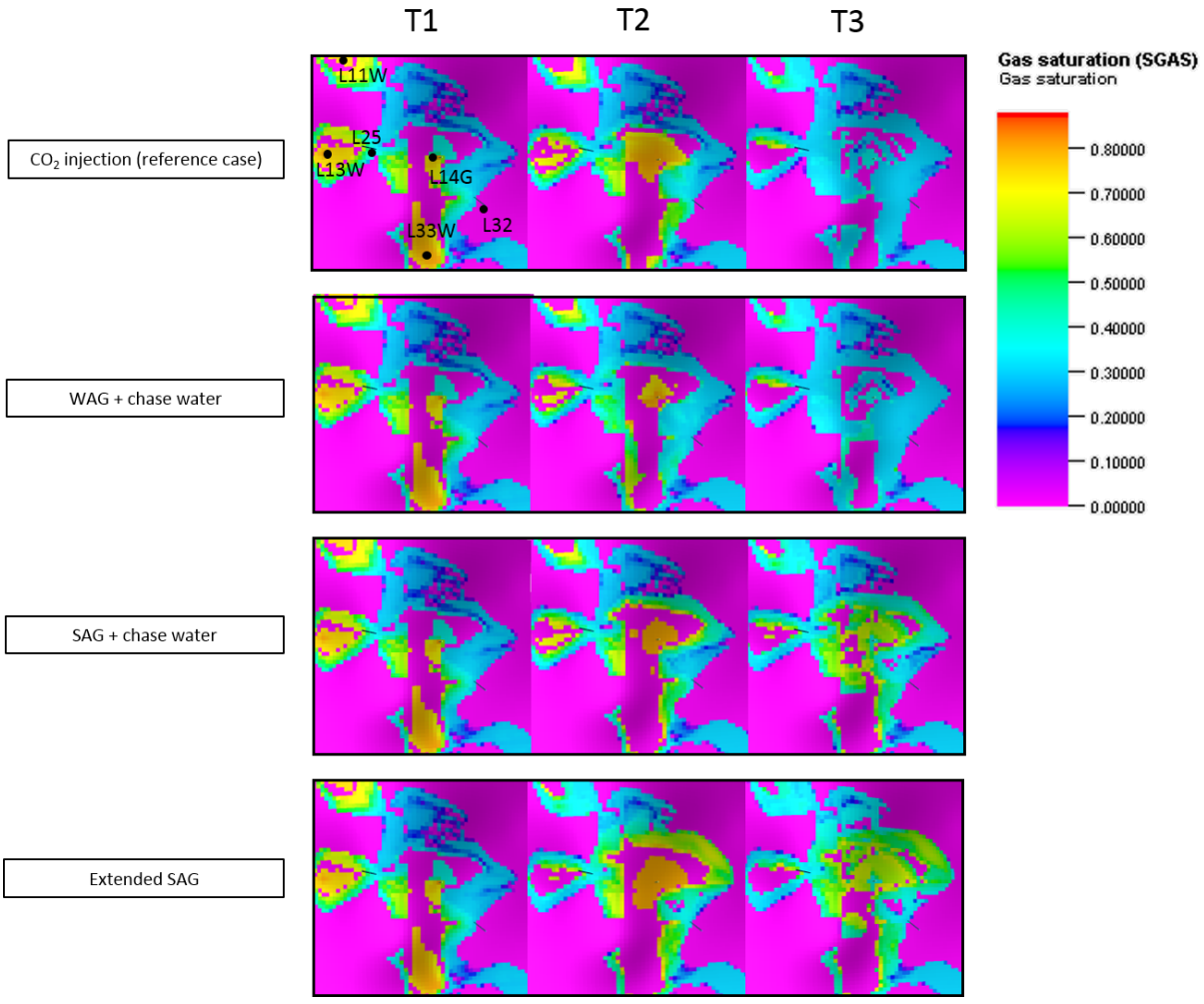

FIGURE 9.10: Gas saturation pattern at initial conditions (T1), after completed injection of CO_2 (T2) and after chase water injection (T3) for the CO_2 reference case, WAG, SAG and extended SAG, in layer 8.

The initial gas saturation, in vicinity of historic (2013-2017) gas injectors (L13W, L33W and L11W) and high permeability, was high in layer 8. The CO_2 reference case and the extended SAG injected most CO_2 in layer 8. The gas saturation decreased for all scenarios during chase water injection, however, the decrease was less for chase water injection after SAG and extended SAG. The gas saturation after chase water injection was higher for SAG and extended SAG, compared to the CO_2 reference case and WAG, which indicates strong foam generation in layer 8 during SAG and extended SAG, and a reduction of inflow of water during chase water injection. This corresponds to the gas saturation after chase water injection in layer 4 and 16 as well, though they did not receive as high gas saturation as layer 8, due to lower permeability. Layer 4 and 16 had a relatively similar gas saturation increase during the CO_2 reference case, SAG and extended SAG, and a higher gas saturation for SAG and extended SAG after chase water injection. The reduction of inflow of chase water indicates diversion of water from high-permeable layers so layers of lower permeability, due to foam generation.

Figure 9.11 shows the CO_2 sweep development in layer 8, in terms of CO_2 tracer volume (Mscf), which illustrates the sweep pattern from injection in L14G more evidently. This is also shown for layer 4 and 16 in Figure C.5 and Figure C.6 in Appendix C.1.

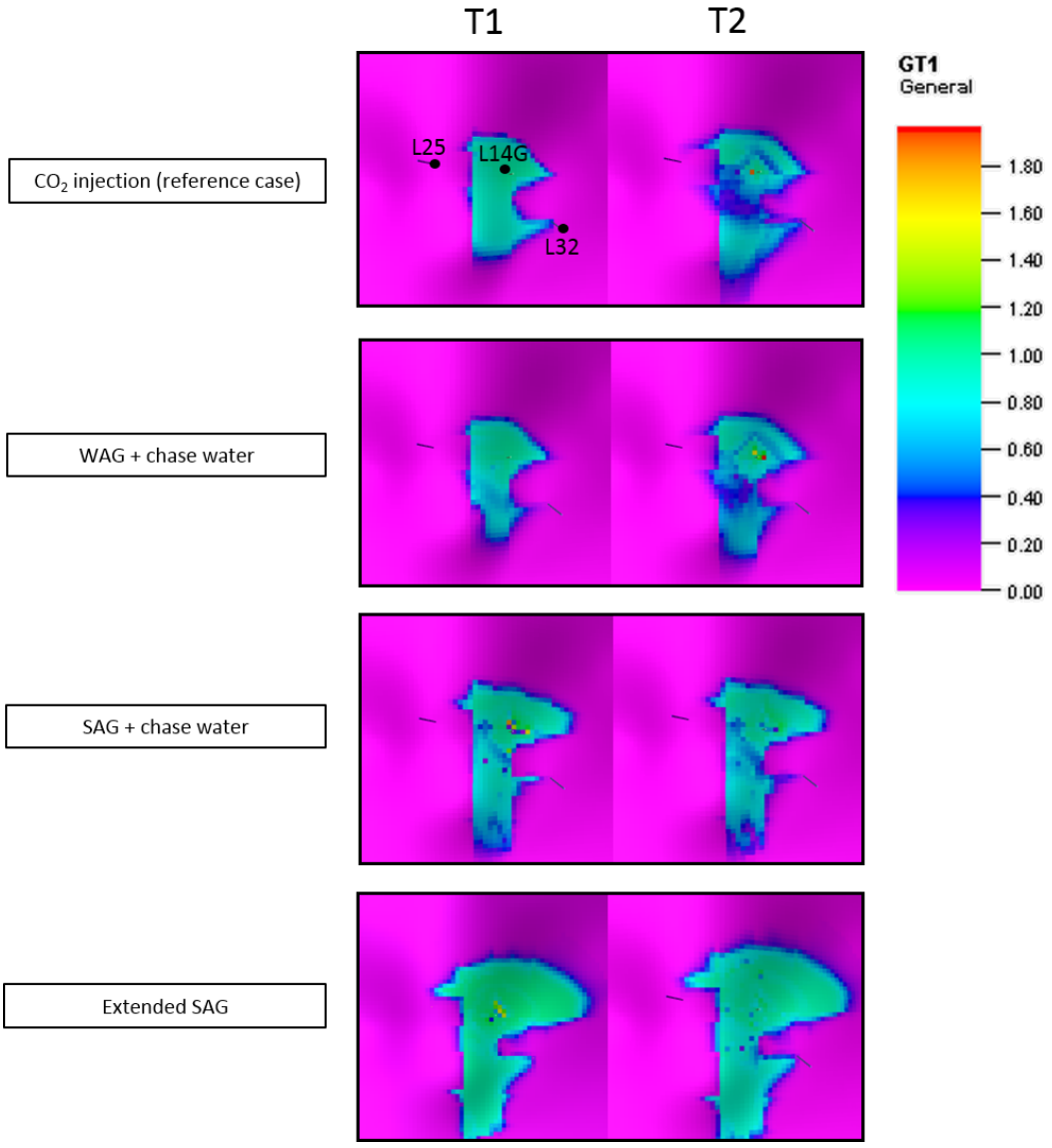

FIGURE 9.11: CO_2 sweep pattern after completed injection of CO_2 (T1) and after chase water injection (T2) for the CO_2 reference case, WAG, SAG and extended SAG, in layer 8. The legend represents the volume of CO_2 tracer in Mscf.

Most of the injected CO_2 during all scenarios swept a portion of the high-permeable region of layer 8 (east region). After completed CO_2 injection, CO_2 sweep was largest in size for SAG and extended SAG, compared to the CO_2 reference case and WAG. After chase water injection, the CO_2 volume decreased most during the CO_2 reference case and WAG (dark blue grid cells), compared to the CO_2 volume for SAG and extended SAG which was almost similar to the sweep before chase water. This corresponds to the diversion of chase water shown in Figure 9.10, where effective foam generation causes chase water to flow in layers of lower permeability. The same effect is also shown for layer 4 and layer 16 in Appendix C.2.

In summary, the 28 layer model has been evaluated in permeability and porosity properties, and CO_2 sweep development has been examined for SAG, extended SAG, WAG and the CO_2 reference case by vertical and areal sweep visualization. From gas saturation changes and increase in CO_2 volume in cross-section L25-L14G-L32, layer 4, 8 and 16 were identified as thief zones for CO_2 as expected. Areal sweep development in layer 8 had the highest gas saturation and corresponding CO_2 volume after completed CO_2 injection for SAG, extended SAG, WAG and the CO_2 reference case, compared to layer 4 and 16, due to the dominant permeability in the east region of layer 8. The areal CO_2 sweep development also revealed that foam performance during SAG and extended SAG diverted chase water from layer 4, 8 and 16 to layers of lower permeability.

To study the effect of foam performance in larger parts of the reservoir, the gas saturation and CO_2 sweep development is evaluated for different flow zones in section 9.3.

9.3 Gas Saturation Profiles for Main Flow Zones

This section presents an identification of flow zones in the field pilot model, with three main flow zones of high average permeability. Evaluation of gas saturation profiles for the three main flow zones quantifies the gas sweep during SAG, WAG and CO_2 reference case. Dynamic gas saturation profiles are also presented for different time intervals, to evaluate the development of gas saturation during the respective chase water injections.

Flow zone identifications shows a total of 6 flow zones in the field pilot model, where three main flow zones receive the majority of injected CO_2. Gas saturation profiles of the three main flow zones shows a similar gas saturation for SAG, extended SAG and CO_2 reference case after completed injection of CO_2, and a slightly lower gas saturation for WAG. Dynamic gas saturation profiles demonstrates a diversion of chase water from the three main flow zones after SAG and extended SAG, due to foam generation.

9.3.1 Flow zone identification

From the formation of horizontal fluid-in-place regions, described in section 7.4.2, there are 6 flow zones derived from the 28 stratigraphic layers. These are schematically shown for the cross-section L25-L14G-L32, in Figure 9.12. The corresponding layers of each flow zone are shown in section 7.4.2.

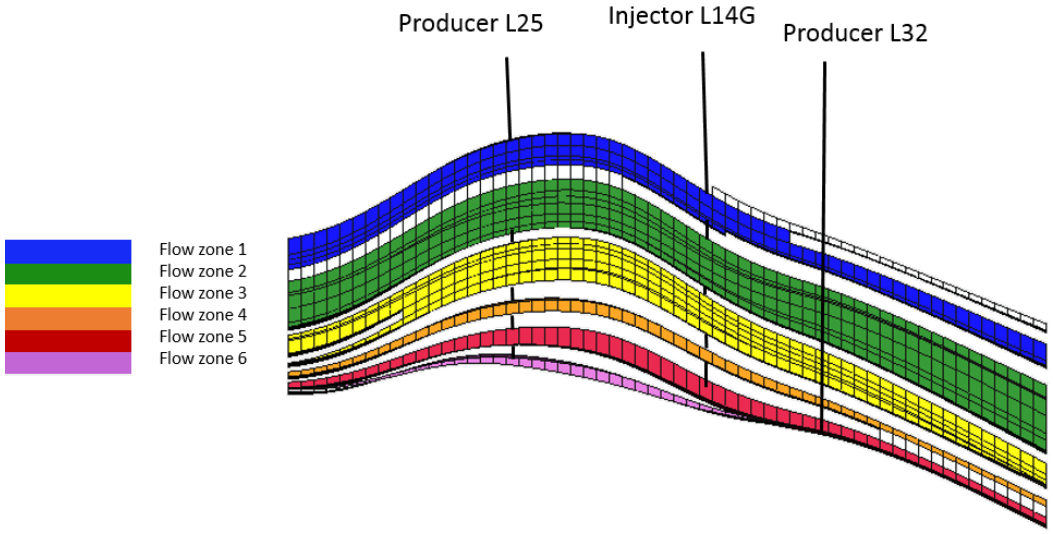

FIGURE 9.12: The 6 identified flow zones in the field pilot model, from the formation of fluid-in-place regions in section 7.4.2.

Table 7.4 illustrates the average properties of permeability in x-direction (K), pore volume (PV), hydrocarbon volume (HCPV) and porosity (ϕ) for the 6 flow zones.

TABLE 9.2: Properties of the defined flow zones in the foam model

Flow zone	K (mD)	PV (Mrb)	HCPV (Mrb)	ϕ (%)
1	3.5	539	404	0.07
2	13.4	1,286	801	0.09
3	3.9	2,730	1,192	0.08
4	2.1	1,114	426	0.07
5	5.8	2,161	1,093	0.10
6	1.3	90	39	0.03

Based on summary data of injection volume for each flow zone, a majority of CO_2 and CO_2 foam (93-95%) was injected into flow zone 2, 3 and 5 during SAG, WAG and the CO_2 reference case. Additionally, based on production data for each flow zone, 91-94% of the cumulative oil production was shown to originate from these main flow zones. Flow zone 2, 3 and 5 received most of the CO_2 was because they had the highest average permeability and porosity of the 6 defined flow zones, from Figure 9.2. Flow zone 2, 3 and 5 also had the highest hydrocarbon pore volume before injection, which explains why most of the oil production originated from these zones.

The flow zones that contribute to CO_2 sweep are evaluated further to investigate the dynamic CO_2 flow across the main parts of the pilot area.

9.3.2 Gas Saturation Profiles

The development of CO_2 sweep has been quantitatively evaluated in lateral directions, by saturation profiles, where the saturation of gas was quantified as a function of distance from injector L14G. Static gas saturation profiles are shown after completed injection of CO_2 for SAG, WAG and the CO_2 reference case and dynamic gas saturation profiles are shown during chase water injection after completed injection of CO_2. As the gas saturation profile for extended SAG was similar to gas saturation profiles for SAG, only the latter is presented.

Gas saturation profiles were created by introducing vertical fluid-in-place regions, as described in section 7.4.2. To evaluate the CO_2 sweep in 3D, saturation profiles were created for different depth intervals, restricted to the three main flow zones. Furthermore, boundary conditions were introduced to confine the lateral assessment of saturation to the selected pilot area, because the evaluation of saturation profiles is only necessary between the pilot injector and the producers. Figure 9.13 illustrate the vertical fluid-in-place regions incorporated to quantify the gas saturation for every 50 ft (x-direction) between L14G and L25. Identical regions were also incorporated on the east side of the pilot pattern to quantify gas saturation for every 50 ft (x-direction) between L14G and L32.

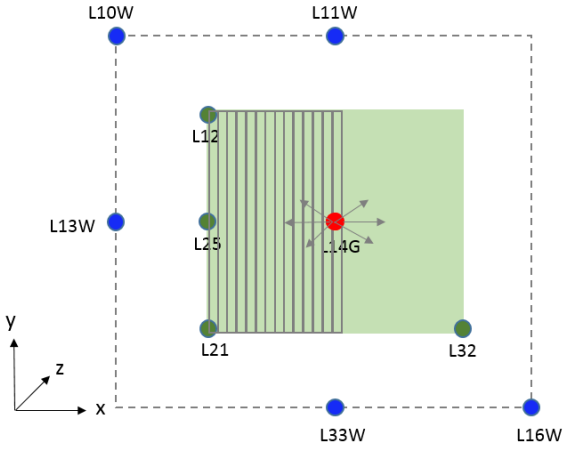

FIGURE 9.13: The figure shows the vertical fluid-in-place regions established between L14G and L25 in the pilot pattern (green shaded area). Identical regions were also incorporated in the east side of the pilot pattern. Each region represents 50 ft in x-direction.

9.3.3 Static Gas Saturation Profiles

The gas saturation profiles between L14G-L25 and L14G-L32 are shown for flow zone 2 (Figure 9.14), flow zone 3 (9.15) and flow zone 5 (9.16) after SAG, WAG and the CO_2 reference case, all without chase water. The saturation profiles are shown relatively to the initial gas saturation profile for each flow zone.

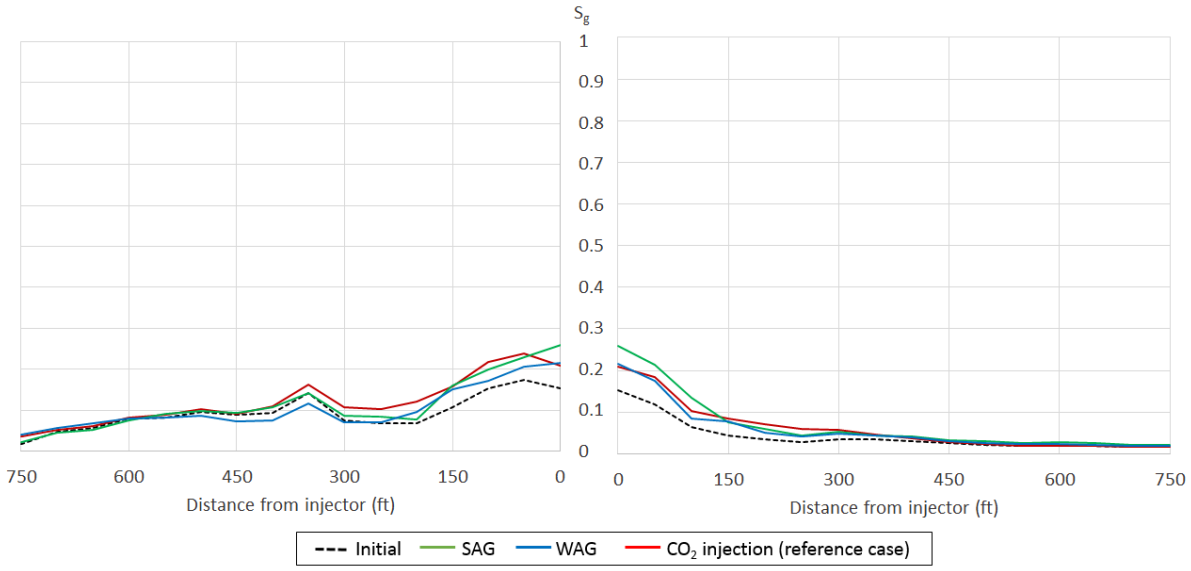

FIGURE 9.14: Gas saturation profiles for flow zone 2, between L14G-L25 (left image) and between L14G-L32 (right image) for SAG (green), WAG (blue) and the CO_2 reference case (red), relative to the initial gas saturation profile (black dotted line) in flow zone 2.

Gas saturation profiles for all injection strategies in flow zone 2, were similar to each other and to the initial profile. This indicates that injection strategies inject a similar amount of gas in flow zone 2 during CO_2 injection cycles. The profiles towards L25 (left image in Figure 9.14) and L32 (right image) were similar in that the saturations in the near well bore area initially decreased rapidly, with stagnating decrease over distance. All injection strategies approached the initial profile as distance from the injector increased, indicating that CO_2 did not propagate in depth of the reservoir in flow zone 2, but were rather trapped or chose pathways that lead to other flow zones. An increase in gas saturation was observed at 350 ft away from L14G, towards L25, which occurred for all profiles including the initial saturation profile. This indicates that gas saturations measured at 350 ft was influenced by the presence of grid cells with an initially high gas saturation.

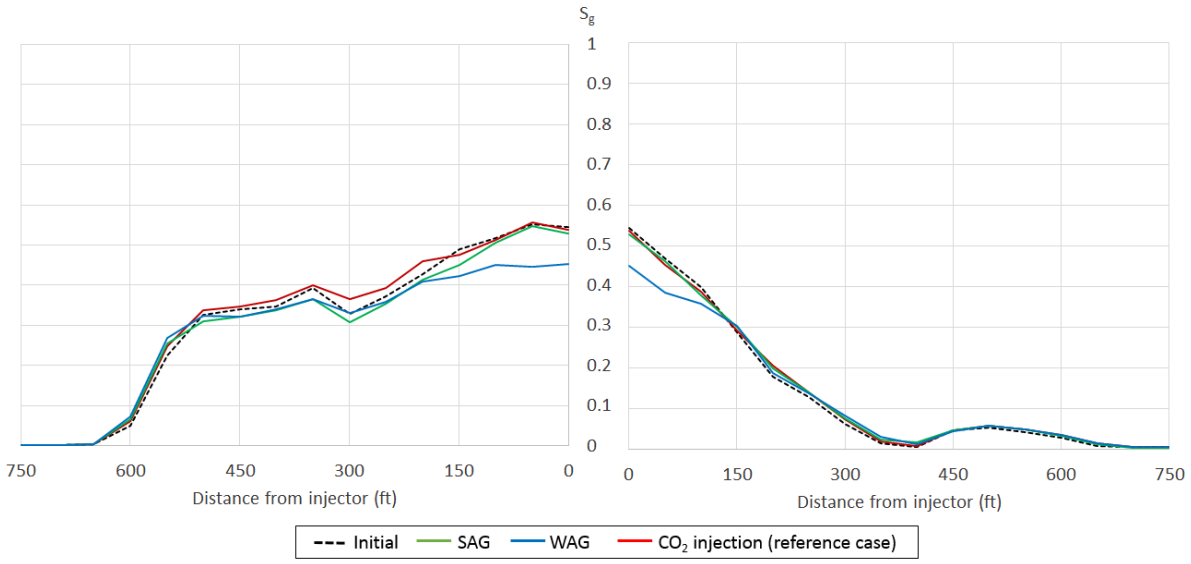

FIGURE 9.15: Gas saturation profiles for flow zone 3, shows higher gas saturation in flow zone 3 compared to the gas saturation in flow zone 2, for all injection strategies.

The gas saturation in flow zone 3 was higher than in flow zone 2, which may be explained by the pore volume for flow zone 3 (2,730 Mrb), which is more than twice as large as flow zone 2. The gas saturation profiles decreased more rapidly in saturation towards L32 than towards L25, which is due to an insignificant porosity in the east region of layer 16 in flow zone 3. As the gas saturation profiles in flow zone 2, the profiles for all cases in flow zone 3, were similar to each other and the initial profile. This indicates that the injection strategies injected an almost similar amount of gas in flow zone 3 during the CO_2 cycles.

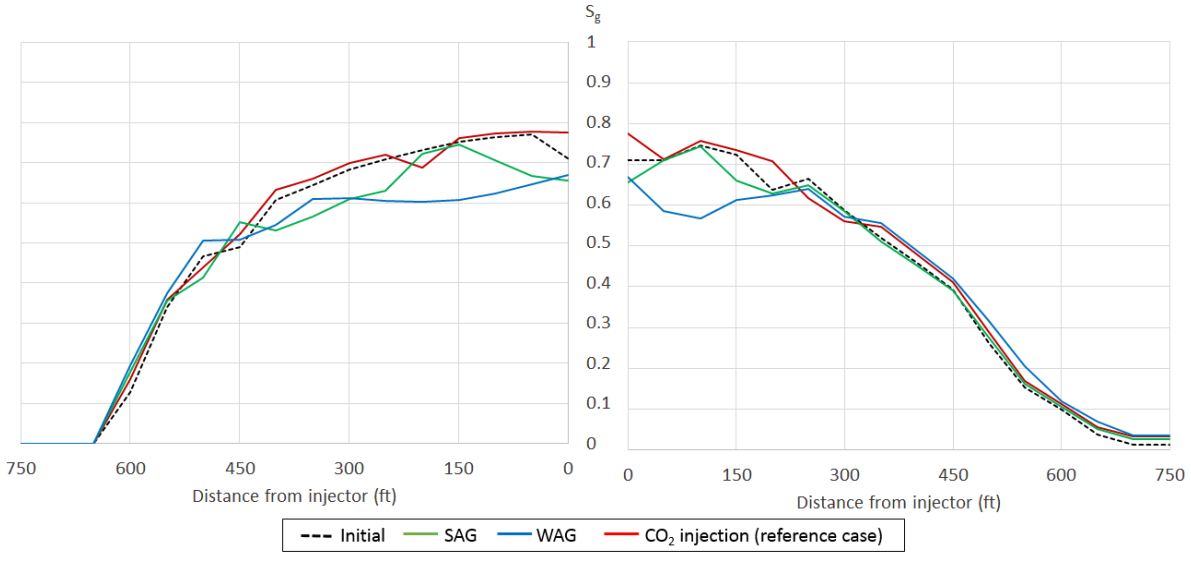

FIGURE 9.16: Gas saturation profiles for flow zone 5, shows that the highest gas saturation was achieved in flow zone 5, compared to flow zone 2 and 3, for all injection strategies.

The gas saturation in flow zone 5 was the highest compared to flow zone 2 and 3. The high saturation in flow zone 5, may be due to a relatively high pore volume (2161 Mrb). The profiles

towards L25 (left image in Figure 9.16) and L32 (right image) were similar, though the profile towards L32 experienced a more rapid decrease in saturation, after 300 ft into the formation. The gas saturations for SAG are lower than the than the initial saturations near the injector until 400 ft into the formation, indicating that SAG may have displaced some of the gas from flow zone 5. Similar as in flow zone 2 and 3, the injection strategies appeared to inject a close to equal amount of CO_2.

9.3.4 Dynamic Gas Saturation Profiles

Dynamic gas saturation profiles are also evaluated to consider the effect of chase water during SAG, WAG and the CO_2 reference case. Dynamic gas saturation profiles are evaluated for all three main flow zones. However, because flow zone 5 had the highest change in gas saturation during chase water injection, the dynamic gas saturations for flow zone 5 are presented below, whereas the profiles for flow zone 2 and 3 are included in Appendix C.3. As the change in saturation profiles were slightly higher between L14G and L25 compared the profiles between L14G and L32, the former was presented below, while the other is included in the Appendix.

The injection time for each slug and the chase water injection for SAG, WAG and the CO_2 reference case is repeated in Figure 9.17, to emphasize the time frame of each slug, which corresponds to the time interval between each gas saturation profile, shown below.

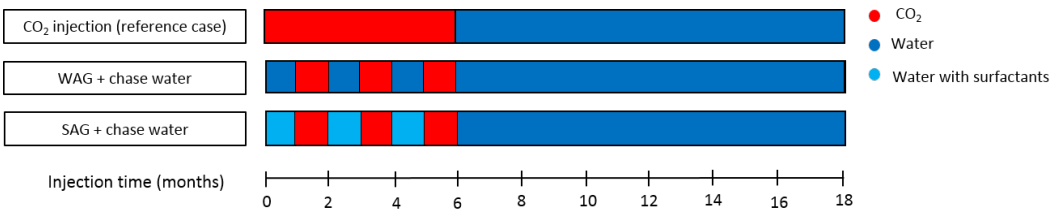

FIGURE 9.17: Injection times for each slug during SAG, WAG and the CO_2 reference case.

Figure 9.18 shows dynamic gas saturation profiles during the CO_2 reference case (+ chase water). Correspondingly, Figure 9.19 shows gas saturation profiles for each slug (each month) during WAG (+ chase water), and Figure 9.20 shows gas saturation profiles after each slug (each month) during SAG (+ chase water).

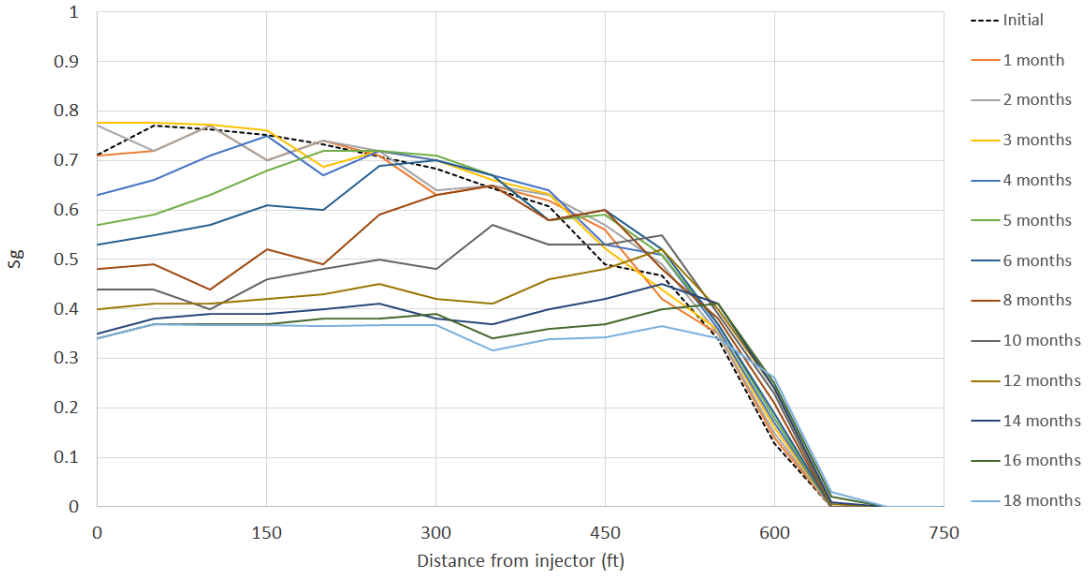

FIGURE 9.18: Dynamic gas saturation profiles between L14G and L25 in flow zone 5, during the CO_2 reference case (+ chase water).

The dynamic gas saturation profiles for the CO_2 reference case in flow zone 5 (Figure 9.18) were similar to the initial gas saturation profile in flow zone 5. During the 15 months chase water injection, the gas saturation decreased and the profiles gradually develop a plateau level in gas saturation from the injector to 400 ft into the formation. The level of the plateau decreased down to 0.36 during water injection and expanded in distance from the injector until 550 ft. The decreasing gas saturation profiles indicates that the chase water flowed in flow zone 5 and displaced gas further into the formation, which extended the length of the plateau. An equal trend was observed for flow zone 2 and flow zone 3. The reduction in gas saturation during chase water injection for the CO_2 reference case corresponds to the areal CO_2 sweep development in layer 4, 8 and 16, described in section 9.2.2.

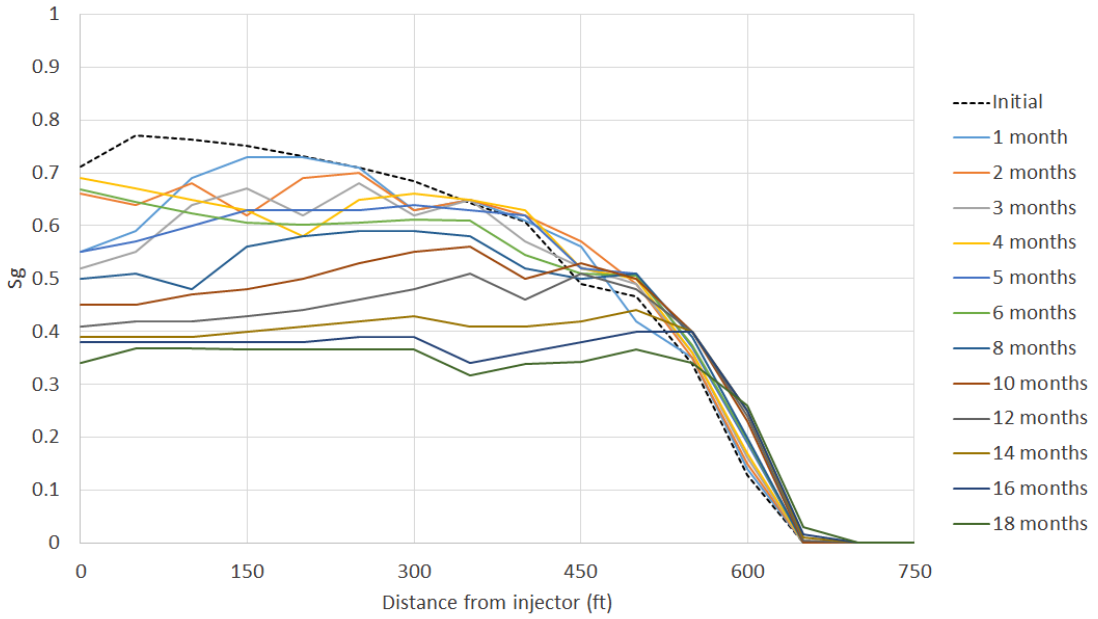

FIGURE 9.19: Dynamic gas saturation profiles in flow zone 5 during WAG (+chase water), which showed a similar change in gas saturation profiles during chase water injection relative to the CO_2 reference case.

The dynamic gas saturation profiles during WAG in flow zone 5 (Figure 9.19) developed a similar plateau level in gas saturation as the chase water injection in the CO_2 reference case. Ultimately, the plateau level attained the same gas saturation as the CO_2 reference case (0.36) 550 ft into the formation. The gas saturation profiles for WAG showed a similar development in flow zone 2 and flow zone 3. As for the CO_2 reference case, the decrease in the dynamic gas saturation profiles indicates that chase water was injected into flow zone 5 after WAG, and displaced the gas further into the formation, which in turn changed the CO_2 sweep corresponding to the visualization in layer 4, 8 and 16 in section 9.2.2.

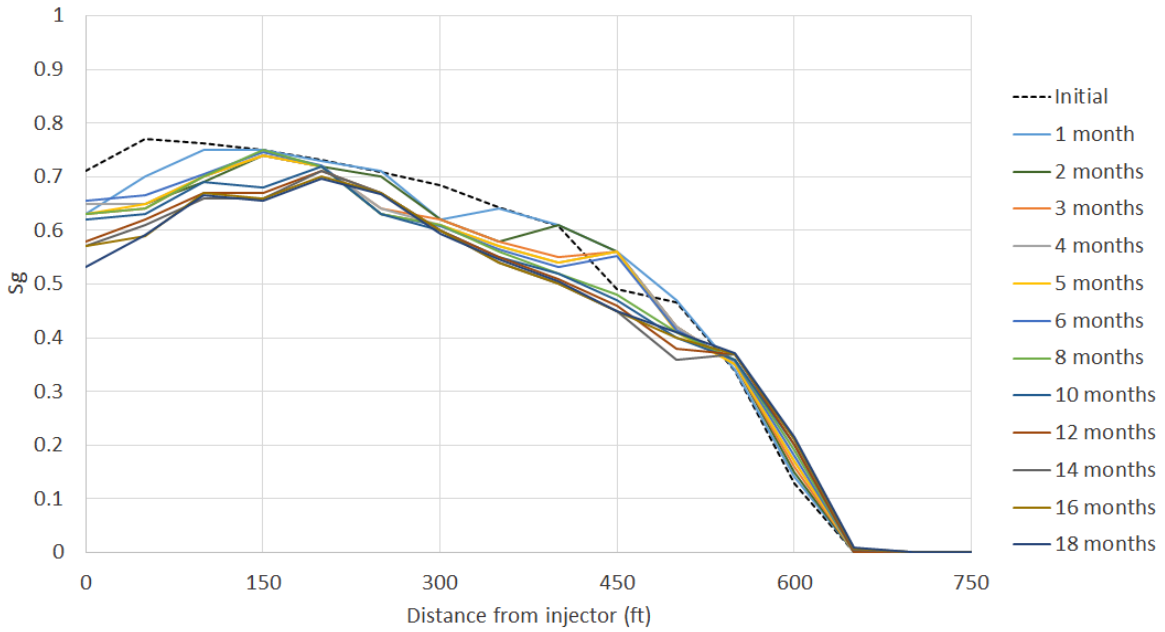

FIGURE 9.20: Dynamic gas saturation profiles in flow zone 5 during SAG (+chase water) shows a constant gas saturation profile during chase water in contrast to the gas saturation profiles during chase water injection after CO_2 reference case and WAG.

The dynamic gas saturation profiles during SAG and the following chase water injection in flow zone 5 (9.20) were similar. SAG and chase water injection in flow zone 2 and flow zone 3 also exhibited constant dynamic gas saturation profiles. This indicates that chase water did not enter flow zone 2, 3 or 5 after foam generation during SAG, in contrast to the CO_2 reference case and WAG. This also corresponds to the visualized areal sweep of CO_2 in layer 4, 8 and 16 from section 9.2.2. As SAG and WAG had identical injection strategies except for addition of surfactants, the large difference in dynamic gas saturation profiles demonstrates that CO_2 foam succeeded in forming high quality foam that blocked flow zone 2, 3 and 5 during SAG, and diverted water to other flow zones of lower permeability.

To summarize, this section has presented 6 identified flow zones that contribute to CO_2 sweep. Flow zone 2, 3 and 5 were evaluated as the main flow zones from a high percentage of injection volume in these zones and a high average permeability compared to the other flow zones. Gas saturation profiles for SAG, WAG and the CO_2 reference case were similar to each other and the initial profile for all three flow zones, which is due to the short injection period of only 3-6 months. The dynamic gas saturation profiles during chase water injection decreased after the CO_2 reference case and WAG, as water displaced some of the gas in the near well bore area. The chase water injection after SAG did not change the dynamic gas saturation profiles, which indicates that chase water did not enter the flow zones where SAG had been injected. A comparison of the chase water injection between SAG and WAG, distinctively showed higher gas saturation profiles during chase water injection for SAG, compared to WAG, as an effect of surfactants and foam generation. It indicates that strong foam is generated in the high-permeability flow zones 2, 3 and 5, which blocks the zones and divert chase water to flow zones

of lower permeability, which corresponds to the areal sweep development for SAG in section 9.2.2.

9.4 Sweep Efficiency Quantification

This section presents a quantified sweep efficiency of CO_2 and water for SAG, extended SAG, WAG, CO_2 reference case and a 3 cycle SAG with extended chase water injection. The sweep efficiencies are calculated after completed injection of CO_2 and after chase water injection.

Quantification of sweep efficiency essentially showed that SAG increased the water sweep efficiency by 15-20% compared to the CO_2 reference case and WAG, due to foam generation. At 0.85% PVI, SAG had a 9% higher CO_2 sweep efficiency compared to the CO_2 reference case and WAG, despite 135 MMscf less CO_2 injected. For an equal CO_2 utilization, the extended SAG increased CO_2 sweep efficiency by 18.6% and increased the water sweep efficiency by 38-45%.

Quantification of sweep efficiency of CO_2 and water, were estimated by the percentage of grid cells attaining a positive tracer volume, relative to the total number of grid cells in the model, described in section 7.2. In addition to a comparison between SAG, extended SAG, WAG and the CO_2 reference case, an extended chase water injection is tested for SAG, to evaluate any potential increase in sweep efficiency due to water, when the 3 cycle SAG achieves the same PVI as the WAG and CO_2 reference case.

The injection strategy of the various simulation cases is illustrated below as a function of injection time.

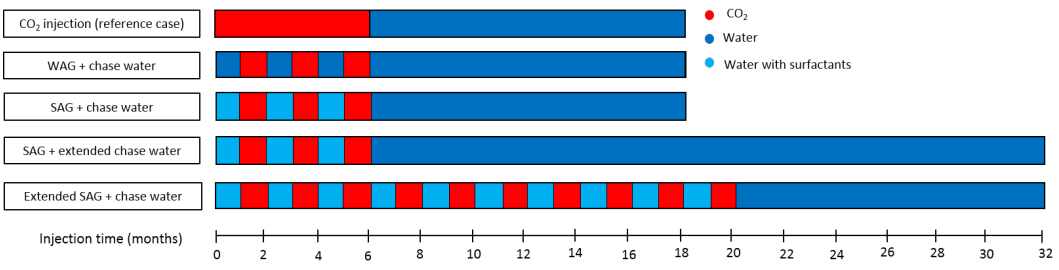

FIGURE 9.21: The timetable demonstrates the injection time of each water injection slug (blue), water injection slug with surfactant (light blue) and CO_2 injection slug (red color) during the CO_2 reference case, WAG, SAG, SAG with extended chase water and extended SAG.

The results of the estimated sweep efficiency for CO_2 and water are graphically shown as a function of PVI in Figure 9.22. The sweep efficiencies are also shown as a function of cycles in Figure 9.23.

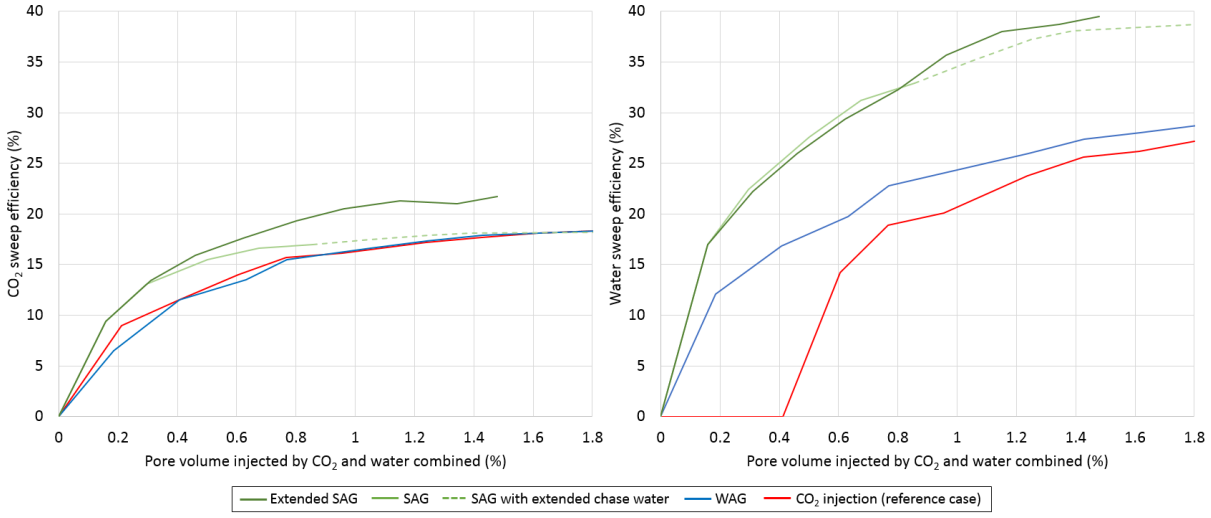

FIGURE 9.22: Estimated sweep efficiency of CO_2 (left) and water (right) for SAG (green), extended SAG (dark green), WAG (blue), CO_2 reference case (red) and SAG with extended chase water (dotted green), as a function of pore volume injected.

The CO_2 sweep efficiency (left image in Figure 9.22) for the CO_2 reference case, WAG and SAG with extended chase water approached an approximately equal sweep efficiency (18.3%) after completed chase water injection. The extended SAG had the highest CO_2 sweep efficiency of 21.7%. The increase in sweep efficiency for SAG and extended SAG followed a similar trend as the increase in oil production for different PVI, which indicates a strong dependency between incremental oil production and increased sweep efficiency during foam SAG and extended SAG. Similar to the oil production, the increase in CO_2 sweep efficiencydecreased after 0.3% PVI, due to foam destabilization during chase water injection, and a less injection volume of CO_2 compared to the other cases. The CO_2 sweep efficiency for SAG had a modest increase during extended chase water injection, due to CO_2 displacement of chase water. SAG and extended SAG had a significantly higher water sweep efficiency (right image in Figure 9.22, compared to WAG the CO_2 reference case.

FIGURE 9.23: CO_2 sweep efficiencies (red percent) and water sweep efficiencies (blue percent) after complete cycles and after chase water injection and the corresponding injection volume of CO_2 and water.

After complete CO_2 injection (left boxes in Figure 9.23), SAG reached a considerably smaller PVI than the other injection strategies, however, the water sweep efficiency was almost similar to WAG. The CO_2 sweep efficiency for SAG was also higher than the CO_2 reference case, despite a 135 MMscf less CO_2 injected, which indicates an efficient sweep increase due to foam generation. For an equal CO_2 volume injected, extended SAG had a CO_2 sweep efficiency of 19.3% which was 66% higher than the sweep of the CO_2 reference case and 29% higher than WAG, due to reduced CO_2 mobility and a more favorable mobility ratio between foam and oil, compared to WAG and the CO_2 reference case. At 0.085% PVI (mid boxes in Figure 9.23), after chase water injection for SAG, SAG had a 12% higher CO_2 sweep than the CO_2 reference case and WAG, despite a significantly lower amount of CO_2 injected. The water sweep efficiency for SAG at 0.085% was 15-20% higher than for WAG and the CO_2 reference case, which may have been due to the diversion of chase water from the three main flow zones of high permeability, to flow zones of lower permeability. After an extended chase water injection (right boxes in Figure 9.23), SAG reached the same PVI as the CO_2 reference case and WAG and reached an even higher water sweep efficiency. The CO_2 sweep efficiency for SAG at this PVI, was almost identical to WAG and the CO_2 reference case, despite foam destabilization during chase water injection and a small CO_2 injection volume. For an equal CO_2 volume injected, extended SAG had a CO_2 sweep efficiency of 21.7%, which was 18,6% higher than for the CO_2 reference case and WAG. The corresponding water sweep efficiency for extended SAG was 38-45% higher than the CO_2 reference case and WAG.

To summarize this section, the sweep efficiency quantification for SAG, extended SAG, WAG, CO_2 reference case and SAG with extended chase water have been evaluated. Due to similar increasing trends in oil production and sweep efficiency during SAG and extended SAG, the incremental oil recovery by foam performance show strong dependence to the increase in sweep efficiency. Similar to the oil production in Figure 8.12, the extended SAG provided the highest CO_2 and water sweep efficiency after CO_2 was injected for each injection strategy and after chase water injection. The 3 cycle SAG, also achieved a higher CO_2 sweep efficiency than the CO_2 reference case and WAG, despite a considerably less amount of CO_2 volume injected. This is mainly because the of CO_2 mobility was reduced during foam injection, which in turn improved the displacement efficiency of oil. The water sweep efficiency of SAG and extended SAG increased due to blocking of high-permeability zones during SAG, which diverted chase water to unswept zones of lower permeability. Conclusively, the results show that oil production is increased due to increased sweep efficiency by foam, which result in a smaller PVI required to reach the same oil production as for WAG and the CO_2 reference case.

To conclude, this chapter has presented an evaluation of sweep efficiency for a variety of SAG injection strategies, which are compared to the CO_2 reference case and WAG. Injection patterns for L14G have been investigated by streamline simulation and production data, with a further evaluation of CO_2 sweep pattern in high-permeable layers 4, 8 and 16. Additionally, sweep efficiency has been evaluated by gas saturation profiles and sweep efficiency quantification. Streamline simulation with TOF's, injection fractions and production identified an injection pattern between L14G-L25 and L14G-L32, which corresponded to well production data for L25 and L32. Evaluation of the 28 layer model, showed large contrasts in permeability and porosity in 6 modified layers, where gas channeling demonstrated high-permeability layers 4, 8 and 16 to be thief zones for CO_2 flow. Areal sweep pattern in the three high-permeability layers indicated a relatively similar gas saturation for SAG, extended SAG and the CO_2 reference case after completed injection of CO_2, and a diversion of chase water for SAG and extended SAG due to foam generation. After dividing the reservoir into flow zones and flow barriers, 6 flow zones where identified. Three main flow zones 2, 3, and 5 had a high average permeability and received a majority of the injected CO_2. These were further investigated through gas saturation profiles, which showed a similar gas saturation for SAG, extended SAG and CO_2 reference case in all three flow zone after completed CO_2 injection. Dynamic flow zones showed diversion of chase water from the main flow zones to flow zones of lower permeability. Quantification of sweep efficiency also demonstrated an increased sweep efficiency of water during chase water injection for SAG, as a result of diversion from high-permeability flow zones.

Part IV

Conclusions & Future work

10. Conclusions

Foam injection strategies have been evaluated and compared to CO_2 injection and WAG in a heterogeneous carbonate reservoir. An optimal foam injection strategy has been identified and the performance has been evaluated through four static performance indicators: cumulative oil production, GOR, degree of CO_2 recycling and a CO_2 utilization factor. Foam performance by SAG has been evaluated during an operation-time-limited scenario and a CO_2-limited scenario, compared to WAG and CO_2 injection. The influence of foam mobility control on sweep efficiency has also been investigated for a variety of SAG injections, through streamline simulation, CO_2 sweep patterns, dynamic gas saturation profiles and sweep efficiency quantification. The key findings from the evaluation of foam performance and sweep efficiency are listed below.

- From a range of different foam injection strategies, 3 cycle SAG with chase water was the optimal injection strategy based on a low CO_2 utilization factor for oil recovery. SAG reduced CO_2 utilization factor, GOR and CO_2 recycling, when compared to WAG and CO_2 injection.
- During an operation-time-limited scenario, SAG achieved a CO_2 utilization factor of 2.5 Mscf/STB compared to CO_2 injection (30.2 Mscf/STB) and WAG (6.9 Mscf/STB), and reduced the recycled volume by 129 MMscf relative to CO_2 injecton and 142 Mscf relative to WAG. For an equal pore volume injected, SAG increased the oil production by 54% compared to CO_2 injection and WAG due to reduced CO_2 mobility and increased sweep efficiency.
- During a CO_2-limited scenario where WAG, an extended SAG and a CO_2 reference case had an equal CO_2 utilization, the extended SAG produced 34,400 STB, compared to the CO_2 reference case (15,600 STB) and WAG (14,800 STB).
- The high-permeability layers 4, 8 and 16 were identified as thief zones for CO_2 flow in the 28 layer model, based on CO_2 sweep pattern. During SAG and extended SAG, chase water was diverted from the three thief zones to surrounding layers of lower permeability.
- The reservoir model was divided into 6 flow zones, where 3 main flow zones received 93-95% of the injected CO_2, due to a high average permeability. Dynamic gas saturation profiles for the 3 main flow zones demonstrated diversion of chase water to flow zones of lower permeability.
- Based on quantification of sweep efficiency, SAG contributed to a 15-20% increase in water sweep efficiency and 9% increase in CO_2 sweep efficiency, compared to CO_2 injection and WAG. For an equal CO_2 utilization, the extended SAG increased the CO_2 sweep efficiency by 18.6% compared to WAG and CO_2 injection.

11. Future Work

For future work it is proposed to look into improvement of weaknesses in the reservoir model and test additional injection scenarios and sensitivities, in addition to perform a cost-benefit analysis of the evaluated injection strategies.

- The reservoir model carries potential for improvements in the stratigraphic layering, where the modified layers from the history matched CO_2 model may be introduced to an enhanced grid resolution to allow a more detailed level of representation in permeability- and porosity contrasts. This must of course be balanced with computer efficiency.
- Hysteresis may be included in the three-phase relative permeabilities in the reservoir fluid model to investigate the effect of hysteresis on SAG injection and foam behavior. The three-phase relative permeabilities may also be investigated further as there are weaknesses associated with the choice of three-phase relative permeability by numerical simulation of WAG injection, and is considered as important for SAG injection as well.
- For further work it is also worth exploring the maximum oil saturation above which foam ceases to be effective in addition to the rate of change of mobility reduction due to oil saturation. This may include the effect of presence of oil on foam performance to improve imitation of foam behavior on field scale.
- Because CO_2 mobility reduction by foam depends on injection rate, it is relevant to explore the sensitivity of injection rate to balance foam generation and mobility reduction with optimal injectivity foam.
- An alternative injection scenario that has not been included in the evaluation of different injection strategies is a combination of SAG with a following WAG. This may introduce cost-savings surfactants compared to an extended SAG and reduce CO_2 utilization compared to chase CO_2.
- For further analysis of the evaluated injection strategies, it is beneficial to assess the cost of surfactant, CO_2 and operating costs with tax credit for EOR and storage in a cost-benefit analysis where net present value is calculated at a discount rate.

A. Appendix

A.1 Baseline Simulation model

The well control and injection strategies in the baseline field pilot model established by Sharma (2017) and Alcorn (2017), are described in this Appendix.

A.1.1 Well control

Initially, the field pilot model was set to start simulation from January 2018 and simulate injection for 18 months, as the field pilot is scheduled for an operation period of 18 months, consisting of 6 months of foam injection, followed by 12 months of chase fluid injection (Alcorn et al., 2017). Based on the latest well data from the field, the producers L12, L21, L25 and L32 were set to produce at a BHP target of 1000 psia by the WCONPROD keyword. The water injector E37W from the historical floods was shut, whereas water injectors L11W and L16W were set to inject water at an injection rate of 50 stb/day and 15 stb/day in the WCONINJE keyword. Similarly, gas injectors L10G, L13G and L33 were set to inject CO_2 solvent at an injection rate of 175 Mscf/day, 800 Mscf/day and 350 Mscf/day. The pilot injector L14G, which was defined as both a water injector (L14W) and a gas injector (L14G) to inject aqueous surfactant solution and CO_2 for foam generation, were set to inject surfactant solution at 600 stb/day and CO_2 solvent at 2000 Mscf/day. All injectors were also controlled by a BHP limit of 4400 psia to prevent the reservoir from reaching fraction pressure. Thus, if the BHP limit was reached, the injector would switch control mode and continue injection at a constant BHP target.

A.1.2 Baseline Foam injection strategies

The simulation work of this Thesis has been built upon baseline strategies for field pilot foam injection, established by Sharma (2017) and Alcorn (2017). Based on the success of 3 cycle WAG injections in East Seminole Field and operation feasibility, a 3 cycle SAG was preferred for foam injection in the pilot injector. For the 3 cycle SAG, each cycle consisted of a surfactant solution injection slug of 1 month, followed by a CO_2 injection slug of 1 month. Generally, simulators under-predict gas injectivity during SAG, because foam does not dry out in the near well bore area which occur in reality (Alcorn et al., 2018). Without the dry out effect, foam is excessively strong in mobility reduction during injection. This causes a high pressure during injection of surfactant solution and CO_2, which result in a low injection rate to avoid reaching fracture pressure. In an attempt to mitigate injectivity issues during SAG, a 6 cycle rapid SAG was also tested. For the 6 cycle rapid SAG, each cycle consists of a surfactant solution slug of 15 days, followed by a CO_2 slug of 15 days. Because the latter SAG case requires a more rapid

alternation of surfactant and CO_2 slugs, it is referred to as a rapid SAG. A case for co-injection of surfactant solution and CO_2 was also made, in addition to a CO_2 injection and WAG to compare the foam performance to normal CO_2 injection and WAG. The simulation cases in this Thesis, have been based on the different simulation cases created by Sharma (2017) and Alcorn (2017), but these have been modified to fit the cases for the evaluation of mobility control and sweep efficiency in this Thesis.

A.2 Data File for Foam Simulation

This Appendix include the data set of the field pilot model, that was used for the SAG simulation case. A description of the changes that were made to the data file for model and field operation modifications, is given in section 7.4. For reproduction of simulation results or modifications for future work, all data files created for simulation work in this Thesis are located at Z:\Resfys\FELLES\MASTERstudenter\2018\Stine Marie Kristiansen.

The red color of the keywords below indicates the start of a new section, whereas the blue color indicates comments.

RUNSPEC
NOECHO
TITLE
PILOT FOAM INJECTION
FIELD
OIL
GAS
WATER
COMPS
6 /
COMPW
2 /
START
1 MAR 2018 /
DIMENS
59 58 28 /
WELLDIMS
15 57 4 5 /
REGDIMS
2 5* 2 /
UNIFOUT
UNIFIN

```
NONNC
MESSAGES
6* 2* 1000000 1000000 /
UDQDIMS
10 10 5* 6 /
UDQPARAM
4* /
GRID
INCLUDE
'GRID.GRDECL' /
INCLUDE
'POROMODINTOLAYER16.GRDECL' /
INCLUDE
'PERMXMODINTOLAYER16.GRDECL' /
MINVALUE
PERMX 0.1 /
/
COPY
PERMX PERMY /
PERMX PERMZ /
/
MULTIPLY
PERMY 0.7 1 59 1 58 1 28 /
/
MULTIPLY
PERMZ 0.16 1 59 1 58 1 1 /
PERMZ 0.6 1 59 1 58 2 2 /
PERMZ 0.16 1 59 1 58 3 3 /
PERMZ 0.6 1 59 1 58 4 5 /
PERMZ 0.16 1 59 1 58 6 6 /
PERMZ 0.6 1 59 1 58 7 8 /
PERMZ 0.16 1 59 1 58 9 9 /
PERMZ 0.6 1 59 1 58 10 11 /
PERMZ 0.16 1 59 1 58 12 12 /
PERMZ 0.6 1 59 1 58 13 13 /
PERMZ 0.16 1 59 1 58 14 14 /
PERMZ 0.6 1 59 1 58 15 16 /
```

PERMZ 0.16 1 59 1 58 17 17 /

PERMZ 0.6 1 59 1 58 18 20 /

PERMZ 0.16 1 59 1 58 21 21 /

PERMZ 0.6 1 59 1 58 22 22 /

PERMZ 0.16 1 59 1 58 23 23 /

PERMZ 0.6 1 59 1 58 24 24 /

PERMZ 0.16 1 59 1 58 25 25 /

PERMZ 0.6 1 59 1 58 26 26 /

PERMZ 0.16 1 59 1 58 27 27 /

PERMZ 0.6 1 59 1 58 28 28 / /

GRIDFILE

0 1 /

INIT

MINPV

1 /

MINDZNET

0.05 /

EDIT

M1: PV AROUND L21 (21, 42)

MULTIPLY

PORV 7.5 17 25 38 46 4 4 /

PORV 7.5 17 25 38 46 7 7 /

PORV 7.5 17 25 38 46 8 8 /

PORV 7.5 17 25 38 46 10 10 /

PORV 7.5 17 25 38 46 11 11 /

PORV 7.5 17 25 38 46 16 16 /

/

M2: TRANSMISSIBILITY BARRIER L21 TO L14

MULTIPLY

TRANX 0.01 17 25 38 38 1 28 /

TRANX 0.01 25 25 38 46 1 28 /

TRANY 0.01 17 25 38 38 1 28 /

TRANY 0.01 25 25 38 46 1 28 /

/

M3: TRANSMISSIBILITY BARRIER L12 TO L14

MULTIPLY

TRANX 0.01 25 25 9 17 1 28 /

TRANY 0.01 25 25 9 17 1 28 /

/

M4: PV FROM L14 TO L32

MULTIPLY

PORV 5 34 59 30 38 4 4 /

PORV 5 34 59 30 38 7 7 /

PORV 5 34 59 30 38 8 8 /

PORV 5 34 59 30 38 10 10 /

PORV 5 34 59 30 38 11 11 /

PORV 5 34 59 30 38 16 16 /

/

M5: TRANSMISSIBILITY FROM L14 TO L32

MULTIPLY

TRANX 0.2 34 59 30 39 1 16 /

TRANY 0.2 34 59 30 39 1 16 /

/

M6: PV FROM L33 TO L32

MULTIPLY

PORV 5 34 59 40 54 4 4 /

PORV 5 34 59 40 54 7 7 /

PORV 5 34 59 40 54 8 8 /

PORV 5 34 59 40 54 10 10 /

PORV 5 34 59 40 54 11 11 /

PORV 5 34 59 40 54 16 16 /

/

M7: TRANSMISSIBILITY FROM L33 TO L32

MULTIPLY

TRANX 0.9 34 59 40 54 1 16 /

TRANY 0.9 34 59 40 54 1 16 /

/

M8: TRANSMISSIBILITY FROM L14 (33,29) TO L25(18,27)

MULTIPLY

TRANX 0.2 19 32 25 31 1 16 /

TRANY 0.2 19 32 25 31 1 16 /

/

MODIFICATIONS IN ROZ

R1: PV AROUND L25 (18, 27)

MULTIPLY

PORV 50 15 22 23 31 18 28 /

/

R2: TRANSMISSIBILITY AROUND L25 (18, 27)

MULTIPLY

TRANX 50 15 22 23 31 18 28 /

TRANY 50 15 22 23 31 18 28 /

/

R3: PV AROUND L12 (19, 12)

MULTIPLY

PORV 5 15 22 9 15 18 28 /

/

R4: TRANSMISSIBILITY AROUND L12 (19, 12)

MULTIPLY

TRANX 5 15 22 9 15 18 28 /

TRANY 5 15 22 9 15 18 28 /

/

R5: PV AROUND L32 (42, 39)

MULTIPLY

PORV 5 39 45 36 42 18 28 /

/

R6: TRANSMISSIBILITY AROUND L32 (42, 39)

MULTIPLY

TRANX 5 39 45 36 42 18 28 /

TRANY 5 39 45 36 42 18 28 /

/

R7: PV FROM L33 TO L32

MULTIPLY

PORV 0.1 33 42 40 54 18 28 /

/

R8: TRANSMISSIBILITY FROM L14 (33,29) TO L25 (18,27)

MULTIPLY

TRANX 1 23 32 30 39 18 28 /

TRANY 1 23 32 30 39 18 28 /

/

R9: PV BETWEEN L12 AND L10

MULTIPLY

PORV 0.1 1 19 1 11 18 28 /

/

R10: TRANSMISSBILBITY BETWEEN L12 AND L10

MULTIPLY

TRANX 0.5 1 19 1 11 18 28 /

TRANY 0.5 1 19 1 11 18 28 /

/

R11: TRANSMISSIBILITY FROM L13 (4, 28) TO L25 (18,27)

MULTIPLY

TRANX 1.5 5 14 25 30 18 28 /

TRANY 1.5 5 14 25 30 18 28 /

/

PROPS

NCOMPS

6 /

EOS

PR /

RTEMP

104 /

STCOND

60 14.696 /

CNAMES

CO2 N2C1 H2SC2C3 C4C5C6 PC1 PC2 /

TCRIT

547.6 340.6 610.9 827.1 1374.3 1324.7 /

PCRIT

1069.9 663.8 706.3 509.8 323.0 248.9 /

VCRIT

1.506 1.583 2.625 4.719 8.746 19.607 /

MW

44.01 16.29 36.19 70.01 148.24 374.21 /

ACF

0.2250 0.0086 0.1202 0.2278 0.4133 0.9618 /

OMEGAA

6*0.45723553 /

OMEGAB

6*0.077796074 /

SSHIFT

6*0 /

TBOIL

350.5 206.2 395.1 552.2 866.1 1368.1 /

PARACHOR

78.0 76.3 122.3 217.1 416.4 865.8 /

BIC

0.1029

0.1285 0.0029

0.1156 0.0136 0.0040

0.1001 0.0327 0.0164 0.0044

0.1146 0.0685 0.0447 0.0229 0.0075

/

PEDERSEN

PEDTUNER

0.5120 1.1240 0.9456 0.5832 0.01062 /

DENSITY

1* 62.4 1* /

PVTW

3400 1* 1.6E-6 0.75 /

ROCK

3400 10E-6 /

STONE

SWFN

0.100 0 0

0.200 0.00001 0

0.235 0.044 0

0.270 0.101 0

0.305 0.165 0

0.340 0.233 0

0.375 0.305 0

0.410 0.379 0

0.445 0.456 0

0.480 0.536 0

0.515 0.617 0

0.550 0.700 0

1.000 1 0 /

SGFN

0.000 0.000 0

0.300 0.000 0

0.340 0.036 0

0.380 0.073 0

0.420 0.109 0

0.460 0.145 0

0.500 0.182 0

0.617 0.288 0

0.733 0.394 0

0.850 0.500 0 /

SOF3

0 0 0

0.050 0 0

0.183 0 0.110

0.317 0 0.220

0.450 0 0.329

0.485 0.000002 0.358

0.520 0.00006 0.387

0.555 0.0005 0.416

0.590 0.002 0.445

0.625 0.006 0.474

0.660 0.015 0.502

0.695 0.033 0.531

0.730 0.065 0.560

0.765 0.118 0.589

0.800 0.199 0.618

0.900 0.700 0.700 /

TRACER

WT1 WATER /

GT1 CO2 /

/

WNAMES

WATER SURFACT /

MWW

18.015 1168.7 /

PREFW

3400 3400 /

DREFW

62.4 62.4 /

CREFW

1.6E-6 1.6E-6 /

VREFW

0.75 0.75

0 0 /

CWTYPE

1* SURFF /

FOAMFRM

192 /

FOAMFSW

0.304 84.3 /

FOAMFCN

9.0E-07 0.6 /

FOAMFSC

1e-3 0 1e-6 /

FOAMFST

0 0.0001616

3.54 0.0000418

/

REGIONS

INCLUDE

'FIPNUM.GRDECL' /

SOLUTION

INCLUDE

FOAMINITPRESS.GRDECL /

INCLUDE

FOAMINITSWAT.GRDECL /

INCLUDE

FOAMINITSGAS.GRDECL /

INCLUDE

FOAMINITXMF.GRDECL /

INCLUDE

FOAMINITYMF.GRDECL /

WMF

95816*1

95816*0

/

DATUM

2047 /

RPTRST

WT1 GT1 'BASIC=2' FLORES PRESSURE SGAS SOIL SWAT AMF XMF YMF ZMF /

TBLKWT1

95816*0 /

TBLKGT1

95816*0 /

SUMMARY

RPTONLY

INCLUDE

'SUMMARYCO2.INC' /

WTPTWT1

/

WTPTGT1

/

WTPTWT1

/

SCHEDULE

TUNING

1 7 0.5 0.5 2 /

/

RPTRST

WT1 GT1 'BASIC=2' FLORES PRESSURE SGAS SOIL SWAT AMF XMF YMF ZMF /

WELSPECS

L12 PROD 19 12 2047 OIL /

L21 PROD 21 42 2047 OIL /

L25 PROD 18 27 2047 OIL /

L32 PROD 42 39 2047 OIL /

E37W WINJ 2 57 2047 WATER /

L10W WINJ 7 2 2047 WATER /

L11W WINJ 32 2 2047 WATER /

L13W WINJ 4 28 2047 WATER /

L14W WINJ 33 29 2047 WATER /

L16W WINJ 58 55 2047 WATER /

L33W WINJ 32 55 2047 WATER /

L10G GINJ 7 2 2047 GAS /

L13G GINJ 4 28 2047 GAS /

L14G GINJ 33 29 2047 GAS /

L33G GINJ 32 55 2047 GAS /

/

FOR CONVERSION FROM GAS INJ TO WAT INJ

L13W 2* 1 28 OPEN 2* .725 1* 0 1* Z /

L14W 2* 1 28 OPEN 2* .725 1* 0 1* Z /

L12 2* 1 28 OPEN 2* .725 1* 0 1* Z /

L21 2* 1 28 OPEN 2* .725 1* 0 1* Z /

L25 2* 1 28 OPEN 2* .725 1* 0 1* Z /

L32 2* 1 28 OPEN 2* .725 1* 0 1* Z /

E37W 2* 1 16 OPEN 2* .725 1* 0 1* Z /

L10W 2* 1 19 OPEN 2* .725 1* 0 1* Z /

L11W 2* 1 16 OPEN 2* .725 1* 0 1* Z /

L16W 2* 1 11 OPEN 2* .725 1* 0 1* Z /

L33W 2* 1 28 OPEN 2* .725 1* 0 1* Z /

L10G 2* 1 28 OPEN 2* .725 1* 0 1* Z /

L13G 2* 1 28 OPEN 2* .725 1* 0 1* Z /

L14G 2* 1 28 OPEN 2* .725 1* -3 1* Z /

L33G 2* 1 28 OPEN 2* .725 1* 0 1* Z /

/

LAST LIQ PROD RATE: L12 - 200, L21 - 100, L25 - 600, L32 - 150

WCONPROD

L12 OPEN BHP 3* 200 1* 1000 /

L21 OPEN BHP 3* 100 1* 1000 /

L25 OPEN BHP 3* 600 1* 1000 /

L32 OPEN BHP 3* 150 1* 1000 / /

LAST INJ RATE : E37W, L10W, L13W, L14W - 0, L11W - 100, L16W - 60

WCONINJE

E37W WATER SHUT BHP 0 1* 4400 /

L10W WATER SHUT BHP 0 1* 4400 /

L11W WATER OPEN BHP 50 1* 4400 /

L13W WATER SHUT BHP 0 1* 4400 /

L14W WATER SHUT BHP 0 1* 4400 /

L16W WATER OPEN BHP 15 1* 4400 /

L33W WATER SHUT BHP 0 1* 4400 /

/

LAST INJ RATE: L10G - 700, L13G - 1600 ,L14G - 2000, L33G - 700

WCONINJE

L10G GAS OPEN BHP 175 1* 4400 /

L13G GAS OPEN BHP 800 1* 4400 /

L14G GAS OPEN BHP 2000 1* 4400 /

L33G GAS OPEN BHP 350 1* 4400 /

/

WELLSTRE

SOLVENT 1 0 0 0 0 0 /

/

WELLSTRW

WATONLY 1.0 0.0 /

WATSURF 0.9999 0.0001 /

/

WINJW

E37W STREAM WATONLY /

L10W STREAM WATONLY /

L11W STREAM WATONLY /

L13W STREAM WATONLY /

L16W STREAM WATONLY /

L33W STREAM WATONLY /

/

WINJGAS

L10G STREAM SOLVENT /

L13G STREAM SOLVENT /

L33G STREAM SOLVENT /

/

WINJW

L14W STREAM WATSURF /

/

WINJGAS

L14G STREAM SOLVENT /

/

WPIMULT

L12 0.75 /

L21 0.175 /

L25 1.2 /

L32 0.45 /

/

LAST RATE : L13W - 200

WCONINJE

L13W WATER OPEN BHP 25 1* 4400 /

L13G GAS SHUT BHP 0 1* 4400 /

L10W WATER OPEN BHP 25 1* 4400 /

L10G GAS SHUT BHP 0 1* 4400 /

L33W WATER OPEN BHP 25 1* 4400 /

L33G GAS SHUT BHP 0 1* 4400 /

/

BEGINNING OF SAG CYCLES

WELOPEN

L14G OPEN /

L14W SHUT /

/

TSTEP

1 /

WRFTPLT

'*' REPT REPT /

/

SURFACTANT SLUG nr. 1 30 DAYS

WELOPEN

L14G SHUT /

L14W OPEN /

/

WCONINJE

L14W WATER OPEN BHP 600 1* 4400 /

/

WINJW

L14W STREAM WATSURF /

/

WTRACER

L14W WT1 1 /

/

TSTEP

1

3*10

/

CO2 SLUG nr. 1 30 DAYS

WELOPEN

L14G OPEN /

```
L14W SHUT /
/
WCONINJE
L14G GAS OPEN BHP 2000 1* 4400 /
/
WTRACER
L14W WT1 0 /
L14G GT1 1 /
/
TSTEP
1
3*10
/
SURFACTANT SLUG nr. 2 30 DAYS
WELOPEN
L14G SHUT /
L14W OPEN /
/
WCONINJE
L14W WATER OPEN BHP 600 1* 4400 /
/
WINJW
L14W STREAM WATSURF /
/
WTRACER
L14G GT1 0 /
L14W WT1 1 /
/
TSTEP
1
3*10
/
CO2 SLUG nr. 2 30 DAYS
WELOPEN
L14G OPEN /
L14W SHUT /
/
WCONINJE
```

L14G GAS OPEN BHP 2000 1* 4400 /

/

WTRACER

L14W WT1 0 /

L14G GT1 1 /

/

TSTEP

1

3*10

/

SURFACTANT SLUG nr. 3 30 DAYS

WELOPEN

L14G SHUT /

L14W OPEN /

/

WCONINJE

L14W WATER OPEN BHP 600 1* 4400 /

/

WINJW

L14W STREAM WATSURF /

/

WTRACER

L14G GT1 0 /

L14W WT1 1 /

/

TSTEP

1

3*10

/

CO2 SLUG nr. 3 30 DAYS

WELOPEN

L14G OPEN /

L14W SHUT /

/

WCONINJE

L14G GAS OPEN BHP 2000 1* 4400 /

/

WTRACER

```
L14W WT1 0 /
L14G GT1 1 /
/
TSTEP
1
3*10
/
CHASE WATER 12 MONTHS
WELOPEN
L14G SHUT /
L14W OPEN /
/
WCONINJE
L14W WATER OPEN BHP 600 1* 4400 /
/
WINJW
L14W STREAM WATONLY /
/
WTRACER
L14G GT1 0 /
L14W WT1 1 /
/
TSTEP
1
12*30
/
```

A.3 Data Reprocessing and Visualization By Petrel E&P

This Appendix presents a detailed descrtion of the procedures that are performed for data visualization and reprosessing of simulation data in Petrel.

For data visualization purposes, Petrel has been imperative to evaluate the foam performance. Summary data from ECLIPSE such as injection and production rates, reservoir pressures and cumulative production has been visualized and evaluated by creating line plots in the "results charting and analysis window" in Petrel. Additionally, simulation grid results have been visualized and evaluated by 3D results analysis in the "3D window" in Petrel. The 3D result

analysis comprise of the requested output of grid properties, such as permeability, porosity, transmissibility and saturations.

For data reprocessing purposes, Petrel has been used for streamline simulation via Frontsim and quantification of sweep efficiency. By selecting Streamlines in the 3D result pane on the Simulation tab, Petrel generated flow patterns as streamlines using simulation results containing 3D flow properties at reservoir conditions. The streamlines were visualized time-of-flight, by going to the streamline folder in the Models pane in Petrel, and selecting the time-of-flight attribute. Injection and production fractions were also extracted after streamlines were generated. This was done by selecting Allocation tables in the Streamlines group of the 3D result pane on the Simulation tab. By choosing for example injection fraction, the table visualized the contribution of each injector to the volume of produced by a well, and correspondingly it visualized production fractions by requesting this.

For quantification of sweep efficiency during foam injection, CO_2 injection and WAG, was performed by the use of pseudo tracers in ECLIPSE and 3D simulation result conversion to grid properties in Petrel. The principally idea for calculating volumetric sweep efficiency (E_v) of injected CO_2 and subsequently for injected water, was to do calculate grid cells contacted by tracer in the reservoir over total number of grid cells in the reservoir. By expanding the Dynamic folder in the Simulation grid results group, in the Result pane in Petrel, and selecting the respective tracer for CO_2 and water, Petrel allowed conversion of 3D tracer simulation results to grid properties. The grid properties for tracer volume of each cell was created in the Model pane, which was further exported to Excel. Furthermore, an Excel formula was used to count the number of grid cells with a positive tracer volume, over the total number of grid cells.

B. Appendix

B.1 Foam Performance

An overview of the number of cycles injected at each pore volume, is shown for the evaluated drainage strategies in chapter 8.

Figure B.1 shows the percent of pore volume injected by CO_2 and water combined, after each water injection slug and CO_2 injection slug, for the reference case, WAG, SAG and extended SAG.

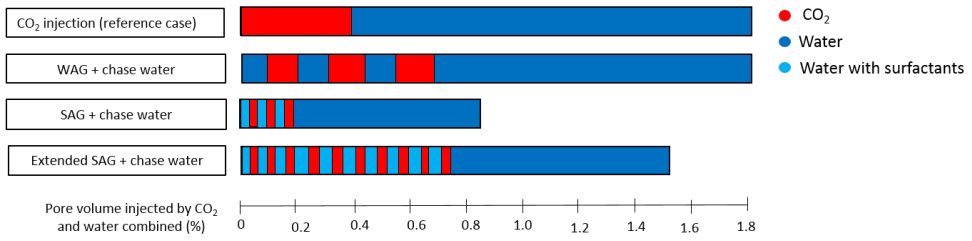

FIGURE B.1: Percent of pore volume injected by CO_2 and water after each injection slug of CO_2 and water during the reference case, WAG, SAG and extended SAG.

An overview of the percent of pore volume injected during each CO_2 cycles for the evaluated drainage strategies in chapter 8. Figure B.2 shows the percent of pore volume injected by CO_2 after each CO_2 injection slug for the reference case, WAG, SAG and extended SAG.

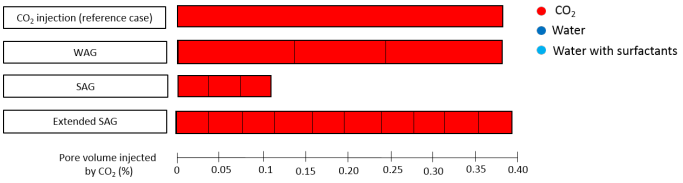

FIGURE B.2: The figure shows the percent of pore volume injected by CO_2 after each CO_2 injection slug for the reference case, WAG, SAG and extended SAG

C. Appendix

C.1 Well Production Data for Injection Pattern Identification

In addition to the cumulative oil production in producer L12, L21, L25 and L32, from Figure 9.4, the cumulative production of gas is shown in Figure C.1 and the cumulative production of water is shown in Figure C.2.

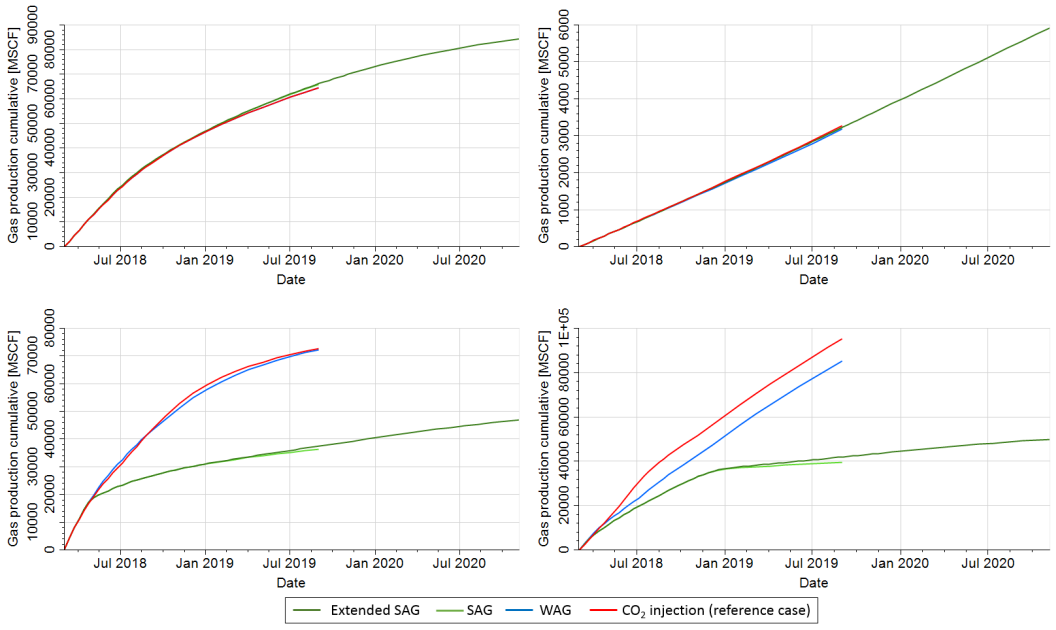

FIGURE C.1: Cumulative hydrocarbon gas production for producer L12, L21, L25 and L32.

Based on the gas production in Figure C.1, a response to the different drainage strategies, SAG, WAG and CO_2 injection, are shown in L25 and L32, similar to oil production in Figure 9.4. In contrast to the oil production, there is also a small and almost negligible response in gas production in L12 for different drainage strategies applied. Similar to the oil production, the gas production response, indicates a preferred pathway for injected CO_2 between L14G-L25 and L14G-L25.

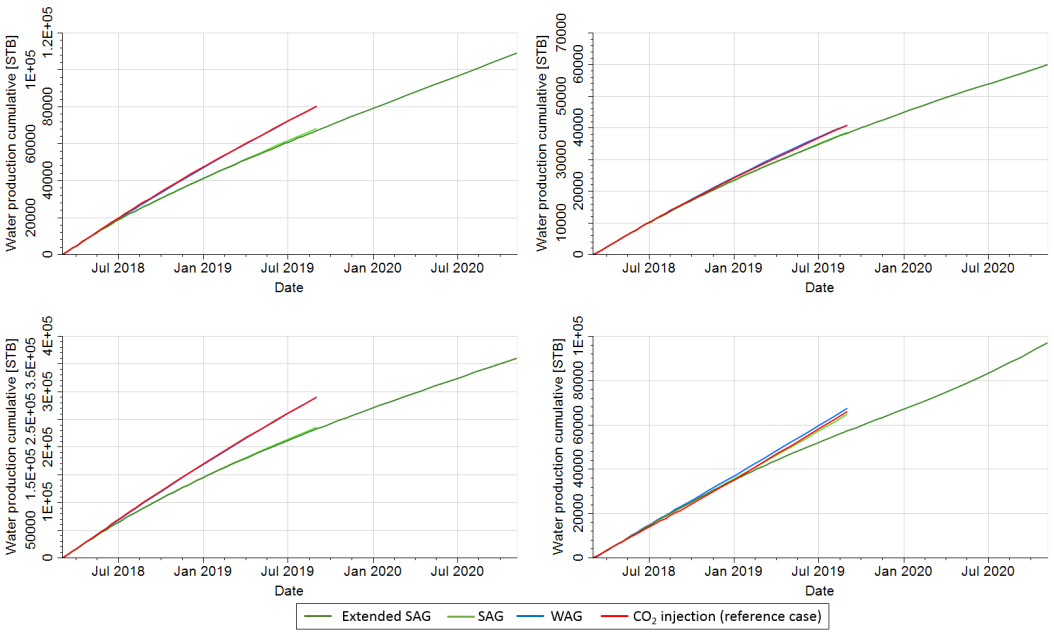

FIGURE C.2: Cumulative water production for all producer, showing a response to different drainage strategies in L12, L25 and L32.

Similar to the cumulative gas production, the water production also changes in producer L12, L25 and L32 for the different injection strategies. Compared to the insignificant change in gas production in L12 for different strategies, the change of water production in L12 is slightly higher. The change in water production in L25 and L32 on the other hand, is smaller, relative to the change in gas and oil production. The response of different injection scenarios, is almost negligible for water production in L32

C.2 Visualization of Areal CO_2 Sweep Pattern

The visualization of CO_2 sweep development is shown for layer 4 and 16 in the figures below, corresponding to the CO_2 sweep development in layer 8 from section 9.2.2.

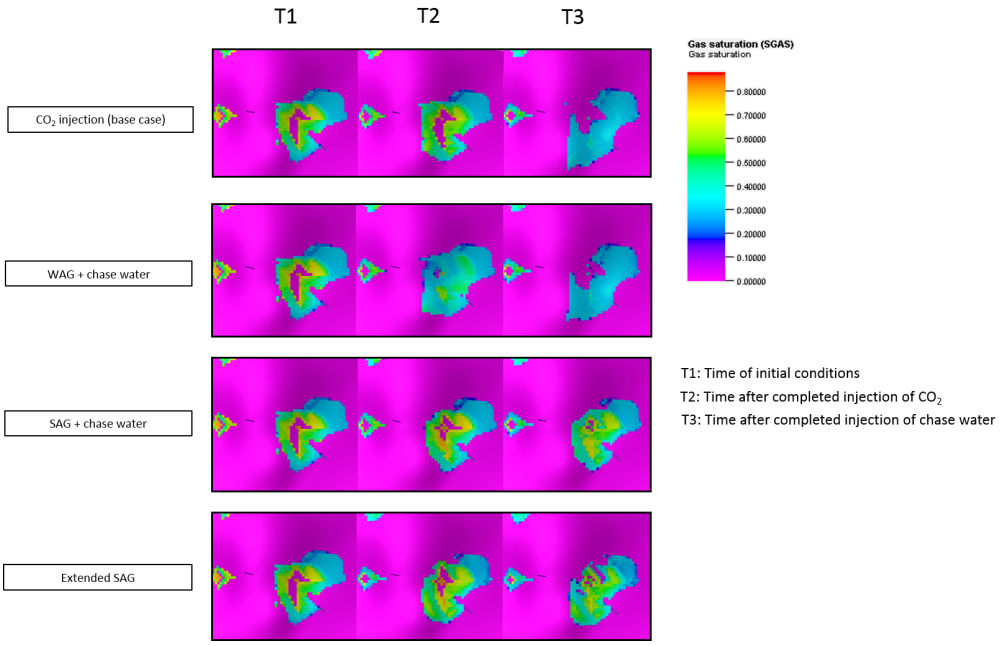

FIGURE C.3: Gas saturation pattern in layer 4 at initial conditions (T1), after completed CO_2 injection (T2) and after chase water injection (T3) for the CO_2 reference case, WAG, SAG and extended SAG.

After completed CO_2 injection, the gas saturation in layer 4 was similar for the reference case, SAG and extended SAG. After chase water injection, both the gas saturation decreased most for the CO_2 reference case and WAG. The gas sweep for SAG and extended SAG is insignificantly affected by chase water injection.

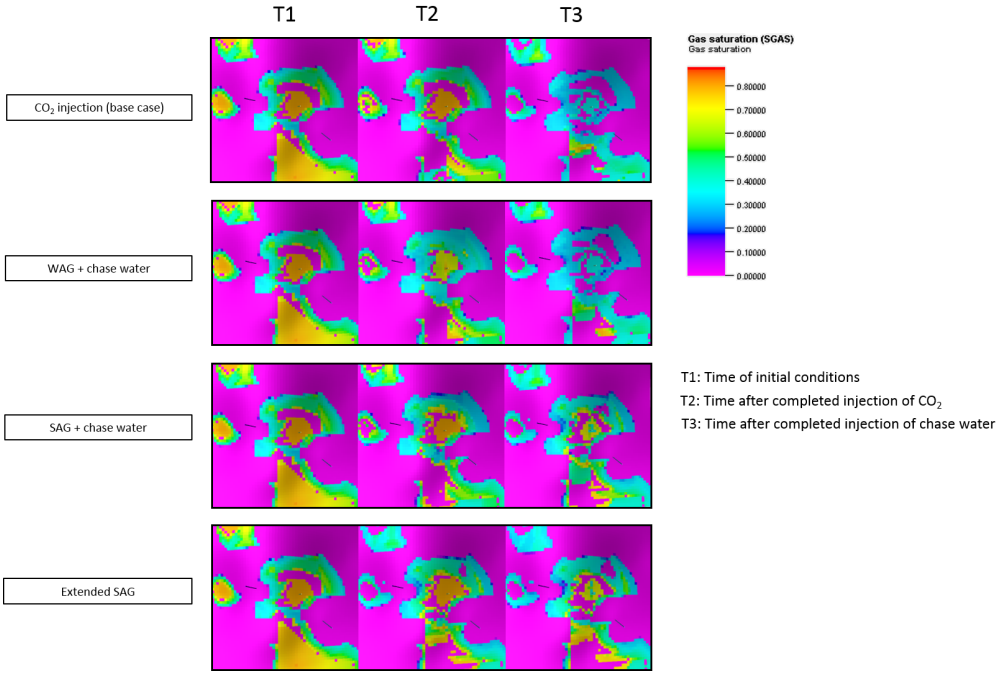

FIGURE C.4: Gas saturation pattern in layer 16, which shows a similar trend for all injection strategies, as in layer 4.

After completed CO_2 injection, the gas saturation decreased in layer 16, for all drainage strategies. After chase water injection, the gas sweep changed most for the CO_2 reference case and WAG.

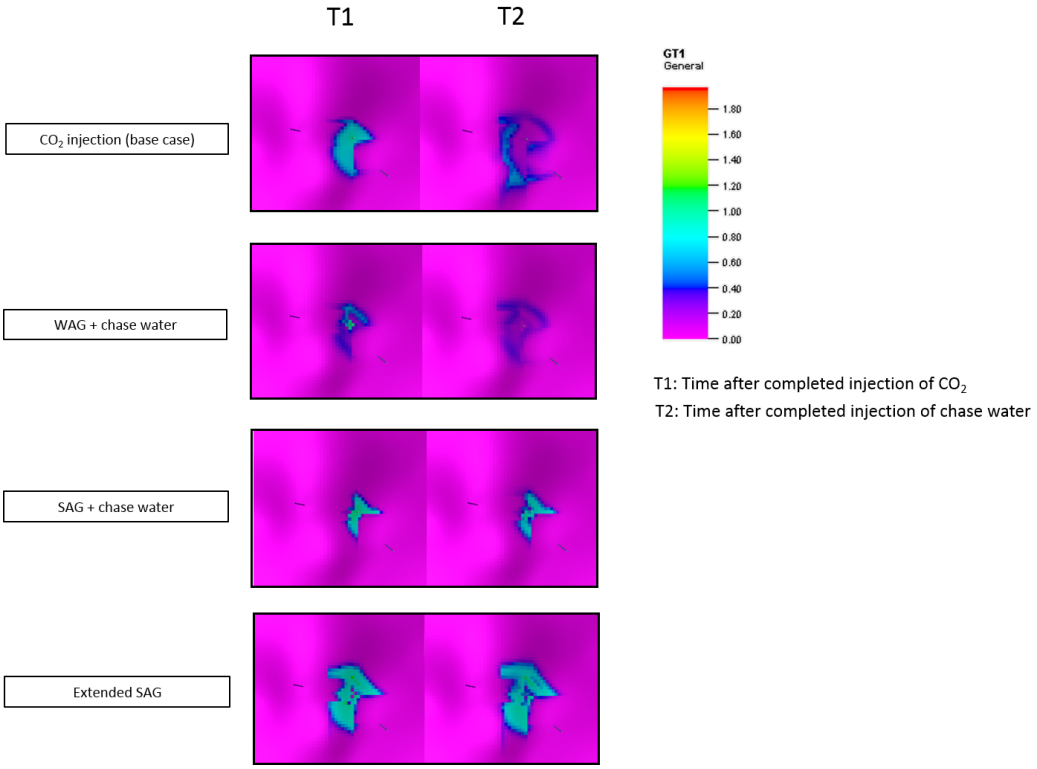

FIGURE C.5: CO_2 tracer volume in layer 4, after completed CO_2 injection (T1) and after chase water injection (T2) for the CO_2 base case, WAG, SAG and extended SAG.

After completed CO_2 injection, the CO_2 sweep was largest for the reference case, SAG and extended SAG. After chase water injection, the CO_2 sweep for the CO_2 reference case and WAG was changed, whereas the CO_2 sweep for SAG and extended SAG remained unchanged.

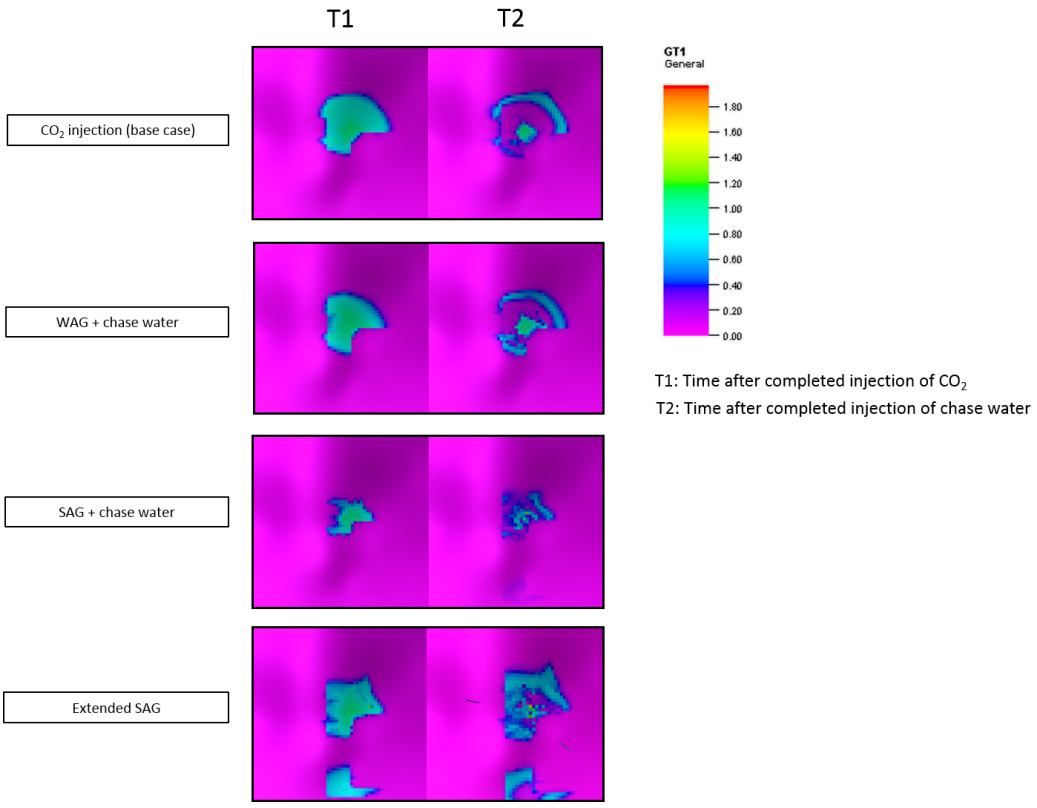

FIGURE C.6: CO_2 tracer volume in layer 16, which shows a similar trend as the CO_2 sweep development in layer 4.

After completed CO_2 injection, the CO_2 tracer volume increased most for the CO_2 reference case, WAG and extended SAG. The sweep pattern changed most for the CO_2 reference case, WAG and SAG after chase water injection.

C.3 Dynamic gas saturation profiles before and after chase water injection

Similar to the development in saturation profiles for flow zone 5, the saturation profiles for SAG, extended SAG, WAG and reference case, are shown below for flow zone 2 and 3. To evaluate the change in gas saturation as function of time, the gas saturation profiles are shown after the total injection of CO_2 and after the additional chase water injection.

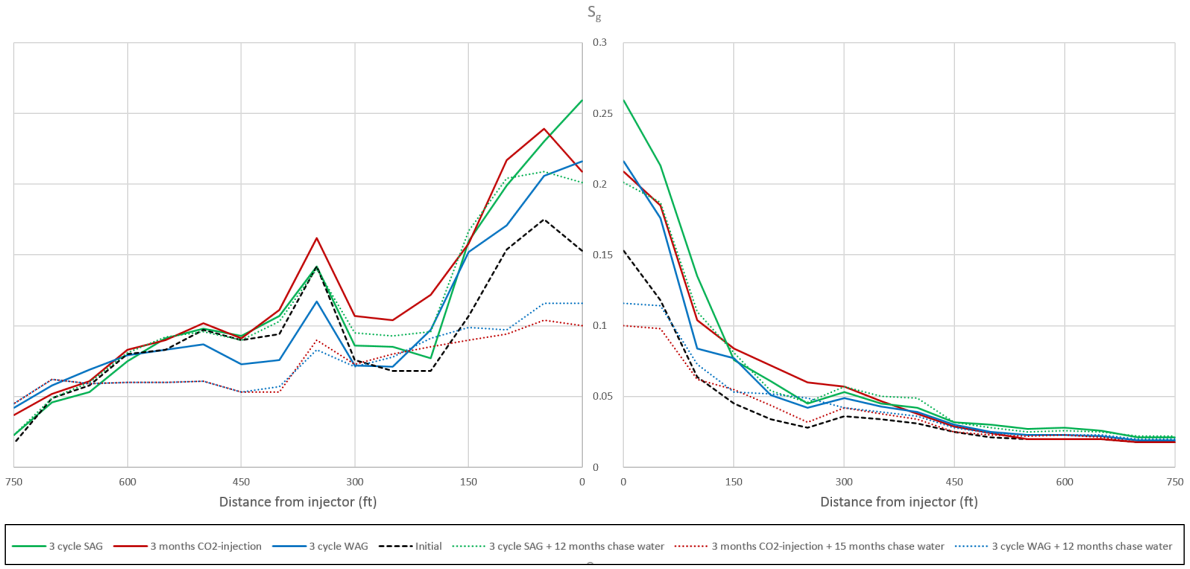

FIGURE C.7: Dynamic gas saturation profiles before (solid lines) and after chase water injection (dotted lines) in flow zone 2

The dynamic saturation profiles for gas in flow zone 2, shows a similar developing trend for the flow towards L25 and L32. The gas saturation profiles for the reference case and WAG decreased during chase water injection. whereas the gas saturation profiles during SAG were similar to the gas saturation profiles during after chase water injection.

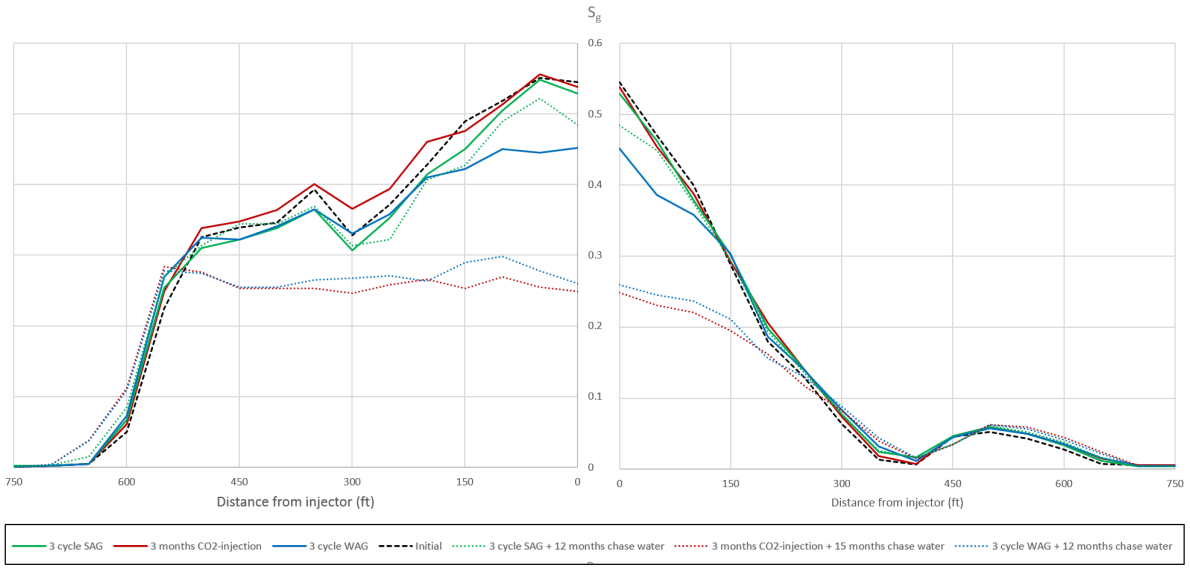

FIGURE C.8: Dynamic gas saturation profiles before (solid lines) and after chase water injection (dotted lines) in flow zone 3.

The saturation profiles for gas in flow zone 3, shows a similar developing trend for the flow towards L25 and L32. The gas saturation profiles for the reference case and WAG decreased during chase water injection. whereas the gas saturation profiles during SAG were similar to the gas saturation profiles during after chase water injection.

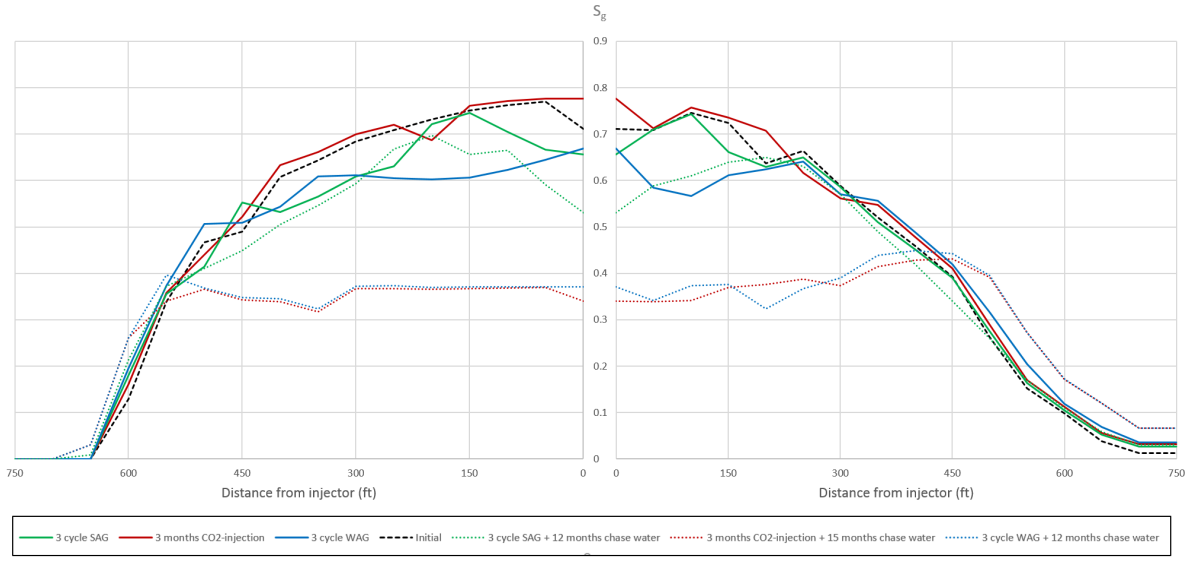

FIGURE C.9: Dynamic gas saturation profiles before (solid lines) and after chase water injection (dotted lines) in flow zone 5.

The saturation profiles for gas in flow zone 5, shows a similar developing trend for the flow towards L25 and L32. The gas saturation profiles for the reference case and WAG decreased during chase water injection. whereas the gas saturation profiles during SAG were similar to the gas saturation profiles during after chase water injection.

C.4 Sweep quantification as Function of Individual Injection Fluids

In an attempt to determine how much the individual injection fluids contributes to sweep efficiency, a quantification of the sweep efficiency of the four different cases is also carried out as a function of pore volume injected by CO_2 and as a function of pore volume injected by water. The results of this are graphically shown in Figure C.10.

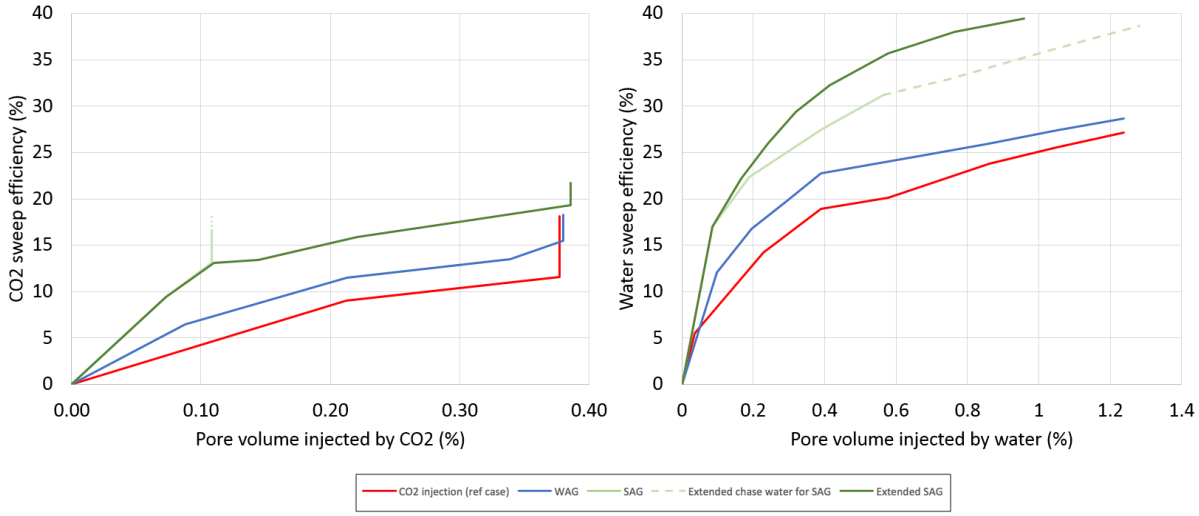

FIGURE C.10: Estimated sweep efficiency of CO_2 as function of pore volume injected by CO_2 and sweep efficiency of water as function of pore volume injected by water.

Primarily, Figure C.10 shows a gradual increase in CO_2 sweep for all the injection strategies during CO_2 injection, in addition to a further increase after CO_2 injection due to the chase water. The water sweep efficiency appears to have an effectively increase at the initial stage of water injection, for all the injection strategies. Further, the increase seems to gradually stagnates, particularly for the reference case and WAG.

The sweep efficiencies for the different scenarios are shown for particular pore volumes injected by CO_2, in Figure C.11. The first estimate at 0.11 PVI by CO_2, represents the sweep efficiency compared to the sweep after the last CO_2 injection slug of a 3 cycle SAG. The last estimate at 0.38 PVI by CO_2, represents the sweep efficiency compared to the sweep after the last CO_2 injection slug for the reference case and WAG.

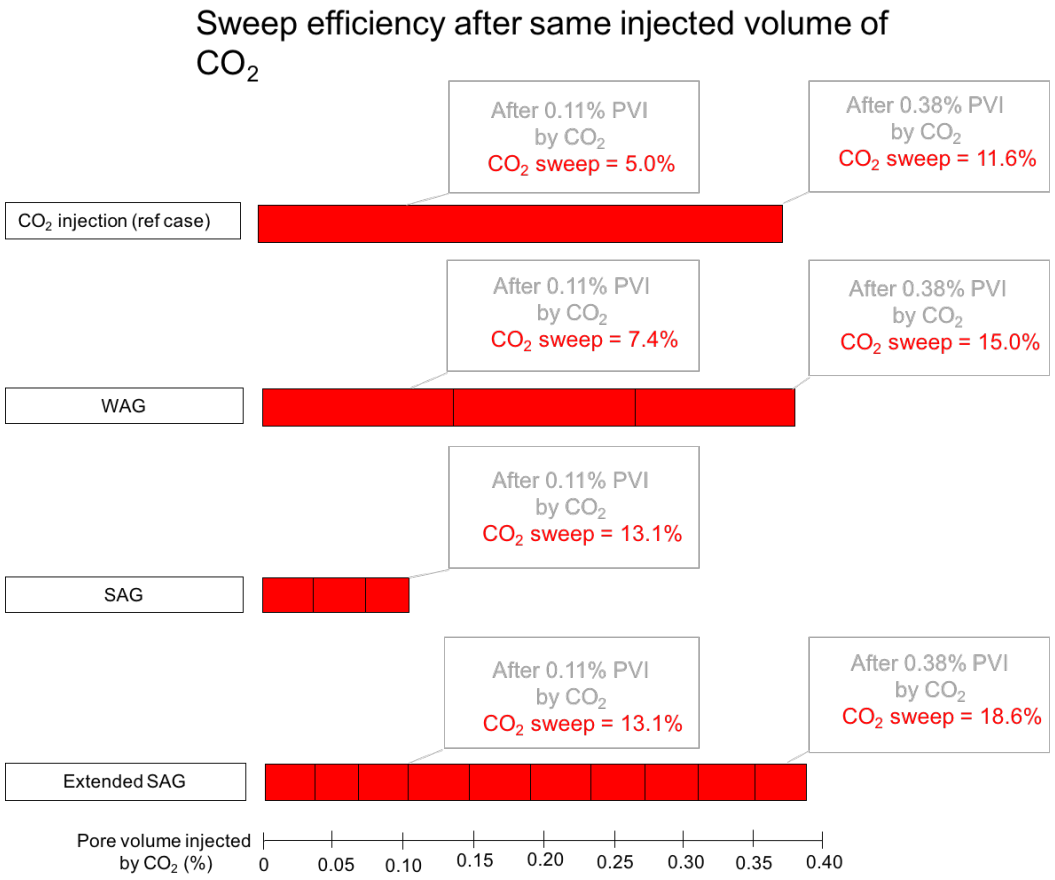

FIGURE C.11: Comparison of CO_2 sweep efficiencies after the last CO_2 injection slug for each scenario.

Based on Figure C.11, it is obvious that after 0.11% PVI by CO_2, SAG reaches the highest CO_2 sweep of 13.1%, compared to 5.0% and 7.4% for the reference case and WAG. Furthermore, at 0.38% PVI, the extended SAG achieves the highest CO_2 sweep of 18.6%, compared to 11.6% and 15.5% for the reference case and WAG.

D. Sensitivity Analysis

D.1 Grid Refinement

To test the sensitivity of grid resolution on sweep development and gas gravity segregation, the model grid was refined in z-direction, corresponding to a refinement of the thickness of each layers. This was done by introducing a local grid refinement (LGR) in ECLIPSE, which is explained in section 7.4.

Since the field pilot model is initialized with pressures, saturations and compositions from the history matched CO_2 flood model, the grid refinement had to be primarily conducted on the history matched CO_2 model, before the field pilot model was refined. The effect of LGR is shown for the history matched CO_2 flood model in Figure D.1.

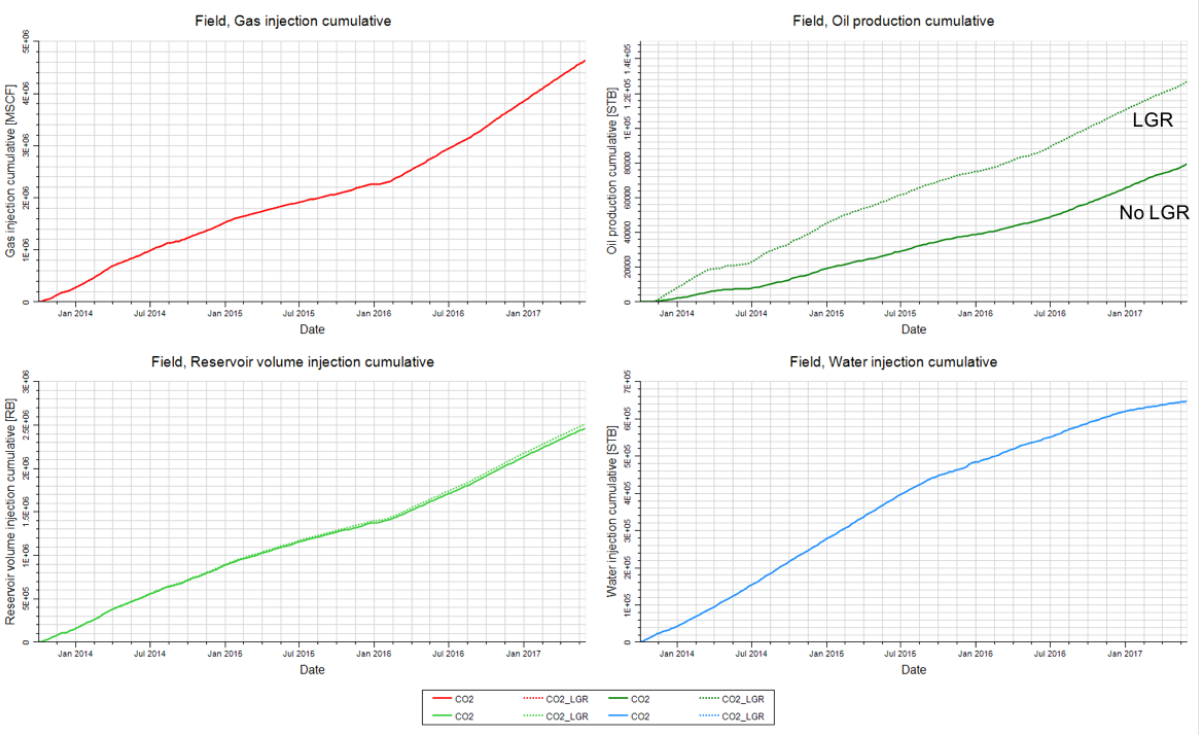

FIGURE D.1: Effect of LGR on oil production during the CO_2 flood in CO_2 flood model.

The grid refinement resulted in a higher cumulative oil production (upper right, Figure D.1) in the CO_2 model. Due to the increase in oil production volume, the initial oil saturation for field pilot model is lower. This reduces the oil recovery potential for the field pilot model, which is shown in Figure D.2.

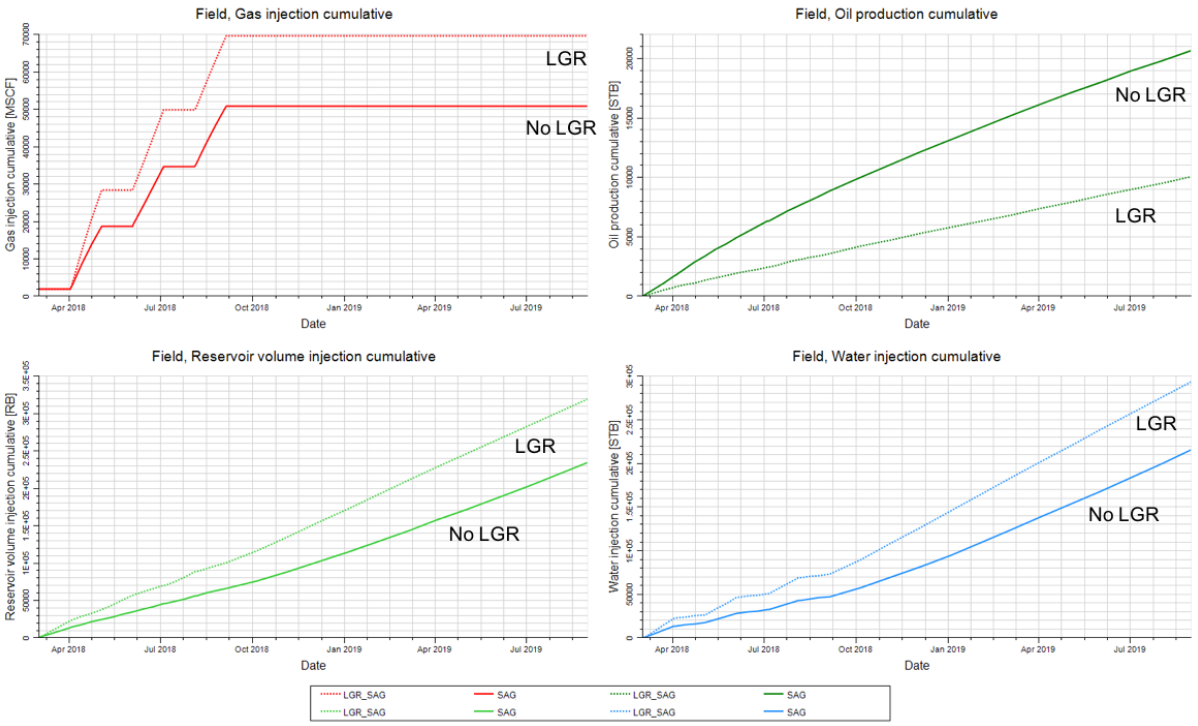

FIGURE D.2: Effect of LGR on SAG performance in the foam pilot model.

The cumulative gas injection, oil production, reservoir volume injection and water injection decreased as a combination of a lower initial oil saturation and an LGR. Due to the reduced initial saturation, it is difficult to evaluate the effect of LGR in the field pilot model. However, the vertical sweep pattern is visualized to illustrate the change after the LGR was performed. Figure D.3 shows the gas saturation sweep for SAG before and after grid refinement. Correspondingly, Figure D.4 shows the CO_2 sweep for SAG before and after grid refinement was performed.

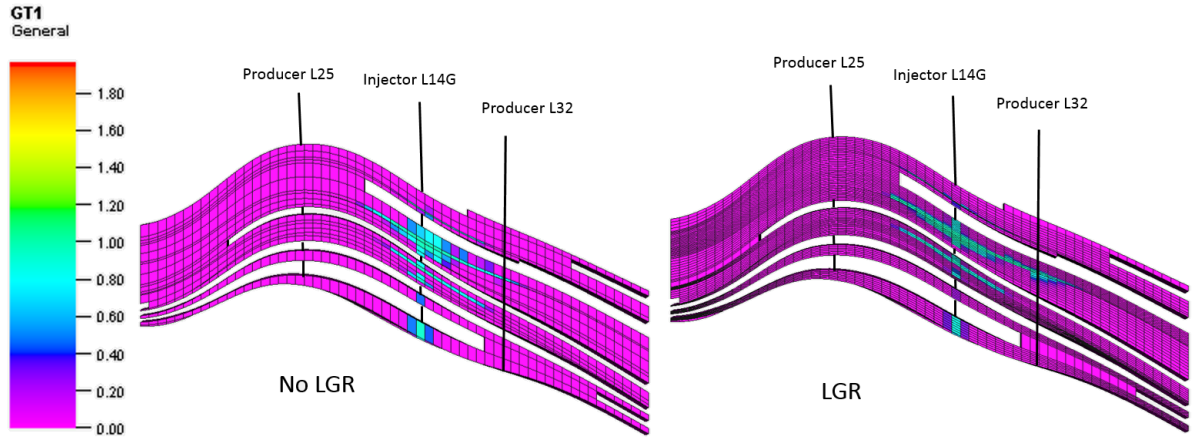

FIGURE D.3: Vertical gas saturation sweep during SAG.

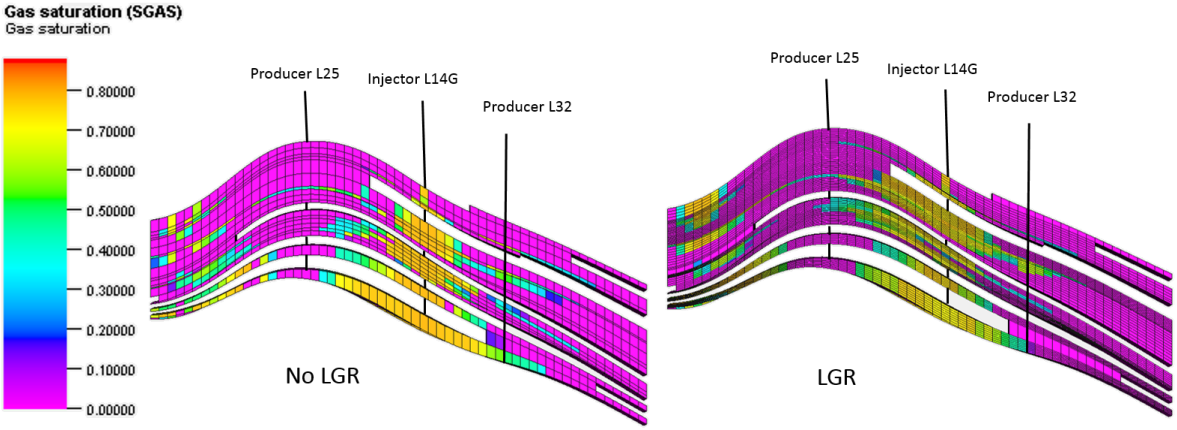

FIGURE D.4: Vertical CO_2 sweep during SAG, before and after grid refinement. The legend shows the volume of CO_2 tracer GT1 (Mscf)

Bibliography

Aarra, M. G., Skauge, A., and Martinsen, H. A. (2002). FAWAG: A Breakthrough for EOR in the North Sea. Society of Petroleum Engineers. *Paper presented at SPE Annual Technical Conference and Exhibition, 29 September-2 October, San Antonio, Texas*. 10.2118/77695-MS.

Alcorn, Z., Fredriksen, S. B., Sharma, M., Rognmo, A. U., Føyen, T. L., Fernø, M. A., and Graue, A. (2018). An integrated CO_2 Foam EOR Pilot Program with combined CCUS in an onshore Texas Heterogeneous Carbonate Field. *Paper presented at SPE Improved Oil Recovery Conference, Tulsa, Oklahoma, USA*. 10.2118/190204-MS.

Alcorn, Z. P. (2017). East Seminole CO_2 Foam Field Pilot Geologic Modeling Updates. Technical report, University of Bergen, Department of Physics and Technology.

Alcorn, Z. P., Fernø, M. A., and Graue, A. (2016). Workflow for Optimal Injection of CO_2 to Enhance Oil Recovery in Mature Oil Fields: A Preliminary Study for a Field Pilot Program. *Paper presented at SPE Bergen One Day Seminar, 20 April, Grieghallen, Bergen, Norway*. 10.2118/180029-MS.

Alcorn, Z. P., Sharma, M., B., F. S., Rognmo, A. U., Føyen, T. L., Fernø, M. A., and A., G. (2017). Co_2 foam field pilot project design. Technical report, University of Bergen, Department of Physics and Technology.

Ali, J. K. (1991). Evaluation of correlations for estimating the viscosities of hydrocarbon fluids. *Journal of Petroleum Science and Engineering*, Volume 5. 10.1016/0920-4105(91)90053-P.

Alimahomed, F., Haddad, E., Velez, E., Foster, R., Downing, T., Seth, C., Melzer, S., and W., D. (2018). The San Andres Play: Obervations and Challenges in Horizontal Wells on the Central Basin Platform, Permian Basin. *Paper presented at SPE Hydraulic Fracturing Technology Conference & Exhibition, The Woodlands, Texas, USA*. 10.2118/189865-MS.

Batycky, R. and Thiele, M. (1973). Estimation of Three-phase Relative Permeability and Residual Oil Data. *SPE Journal*. 10.2118/73-04-06.

Batycky, R. and Thiele, M. (2016). Mature Flood Surveillance Using Streamlines. *Journal of Petroleum Technology*, 68.

Bennion, D. and Bachu, S. (2010). Drainage and imbibition co2/brine relative permeability curves at reservoir conditions for carbonate formations. *SPE Journal*, SPE 134028.

Brooks, R. H. and Corey, A. T. (1964). Hydraulic properties of porous media. Technical Report Volume 3, Colorado State University.

Camber Energy, I. (2018). Breaking New Ground in Technically Familiar Areas. Camber Energy web site. https://www.camber.energy/operations/west-Texas.

Chang, S. H. and Grigg, R. B. (1999). Effects of Foam Quality and Flow Rate on CO_2-Foam Behavior at Reservoir Temperature and Pressure. *SPE Journal*, 10.2118/56856-PA.

Correia, M., Filho, J., Gaspar, A., and Schiozer, D. (2015). *UNISIM-II: Benchmark Case Proposal Based on a Carbonate Reservoir.* UNISIM-CEPETRO-Unicamp, https://www.unisim.cepetro.unicamp.

Dai, Z., Viswanathan, H., Xiao, T., Middleton, R., Pan, F., Ampomah, W., Yang, C., Jia, W., Lee, S. Y., Cather, M., Balch, R., and McPherson, B. (2017). CO_2 Sequestration and Enhanced Oil Recovery at Depleted Oil/Gas Reservoirs. *Energy Procedia.* 10.1016/j.egypro.2017.08.034.

Dostal, V., Driscoll, M. J., and Hejzlar, P. (2004). A Supercritical Carbon Dioxide Cycle for Next Generation Nuclear Reactors. Technical report, The MIT Centre for Advanced Nuclear Energy Systems, http://hdl.handle.net/1721.1/17746.

Encyclopedia, N. W. (2015). *Supercritical fluid.* http://www.newworldencyclopedia.org.

Enick, R. M. and Olsen, D. K. (2012). Mobility and Conformance Control for Carbon Dioxide Enhanced Oil Recovery via Thickeners, Foams, and Gels - A Detailed Literature Review of 40 Years of Research. Technical report, National Energy Technology Laboratory.

Ertekin, T., Abou-Kassem, J. H., and King, G. R. (2001). *Basic Applied Reservoir Simulation.* Society of Petroleum Engineers Inc.

Franc, J., Horgue, P., Guibert, R., and Debenest, G. (2016). Benchmark of different CFL conditions for IMPES. *Elsevier.*

Gajbhiye, R. N. and Kam, S. I. (2011). Characterization of foam flow in horizontal pipes by using two-flow-regime concept. *Chemical Engineering Science*, 66(8):1536–1549. 10.1016/j.ces.2010.12.012.

Gray, T. J. (1989). Development study East Seminole San Andres Field Gaines County, Texas. Technical report, Mobil Exploration & Producing U.S. Inc. Midland Division.

Grigg, R. B., Svec, R. K., and Ferguson, D. J. (2002). Improving CO_2 Efficiency for Recovering Oil in Heterogeneous Reservoirs. Technical report, New Mexico Petroleum Recovery Research Center.

Hægland, H., Dahle, H. K., Eigestad, T., Lie, K. A., and Aavatsmark, I. (2007). Improved streamlines and time-of-flight for streamline simulation on irregular grids. *Advances in Water Resources*, volume 30. 10.1016/j.advwatres.2006.09.002.

Holstein, E. D. (2007). Vol 5: Reservoir Engineering and Petrophysics. In *Petroleum Engineering Handbook.*

Honarpou, M. M., Nagarajan, N. R., Grijalba, A. C., Valle, M., and Adesoye, K. (2010). Rock-Fluid Characterization for Miscible CO_2 injection: Residual Oil Zone, Seminole Field, Permian Basin. *Paper presented at SPE Annual Technical Conference and Exhibition, Florence, Italy.* 10.2118/133089-MS.

IPPC (2014). Climate Change 2014 Synthesis Report Summary for Policy Makers. Technical report, Intergovernmental Panel on Climate Change.

Irlam, L. (2017). Global Costs of Carbon Capture and Storage. Technical report, Glocal CCS Institute.

Jian, G., Puerto, M. C., Wehowsky, A., Dong, P., Johnston, K. P., Hirasaki, G. J., and Biswal, S. L. (2016). Static Adsorption of an Ethoxylated Nonionic Surfactant on Carbonate Minerals. *Langmuir*.

Kamali, F., Hussain, F., and Cinar, Y. (2014). A Laboratory and Numerical Simulation Study of Co-optimizing CO_2 Storage and CO_2 EOR. *Paper presented at SPE Asia Pacific Oil & Gas Conference and Exhibition, Adelaide, Australia*, 10.2118/171520-MS.

Kloet, M. B., Renkema, W. J., and Rossen, W. R. (2009). Optimal Design Criteria for SAG Foam Processes in Heterogeneous Reservoirs. *Paper presented at EUROPEC/EAGE Conference and Exhibition, Amsterdam, The Netherlands*. 10.2118/121581-MS.

Kovscek, A. R. (2010). Modeling Foam Displacement With the Local-Equilibrium Approximation: Theory and Experimental Verification. *SPE Journal*. 10.2118/116735-PA.

Kulkarni, M. and Rao, D. N. (2004). Experimental Investigation of Various Methods of Tertiary Gas injection. *Journal of Petroleum Science and Engineering*. https://doi.org/10.2118/90589-MS.

Marcondes, F., Maliska, C. R., and Zambaldi, M. C. (2009). A Comparative Study of Implicit and Explicit Methods Using Unstructured Voronoi Meshes in Petroleum Reservoir Simulation. *Journal of the Brazilian Society of Mechanical Science*, 10.1590/S1678-58782009000400010.

Martel, M., Hebert, A., Lefebvr, R., Glinas, P., and Gabriel, U. (2004). Displacement and sweep efficiencies in a DNAPL recovery test using micellar and polymer solutions injected in a five-spot pattern. *Journal of Contaminant Hydrology*, 75:Pages 1–29. 10.1016/j.jconhyd.2004.03.007.

Mukherjee, J., Nguyen, G. P., Scherlin, J. M., Vanderwal, P. G., and Rozowski, P. (2016). CO_2 Foam Pilot in Salt Creek Field, Natrona County, WY: Phase III: Analysis of Pilot Performance. *SPE Journal*. Paper presented at SPE Improved Oil Recovery, Tula, Oaklahoma, USA.

Mulligan, C. M. (2007). Chapter 15 - Rhamnolipid Biosurfactants: Solubility and Environmental Issues. *Thermodynamics, Solubility and Environmental Issues*, pages 279–298. 10.1016/B978-044452707-3/50017-3.

Nguyen, V. D., Adragna, P. A., and Lafon, P. (2014). Predicting the Effects of Material and Process Parameters on Springback by Fem Numerical Simulation in Sheet Metal Forming. hal-01166691.

Norris, S. O., Scherlin, J. M., Mukherjee, J., Vanderwal, P. G., Abbas, S., and Nguyen, G. P. (2014). CO_2 Foam Pilot in Salt Creek Field, Natrona County, WY: Phase II: Diagnostic Testing and Initial Results. *Paper presented at SPE Annual Technical Conference and Exhibition, Amsterdam, The Netherlands*. 10.2118/170729-MS.

OECD/IEA (2017). Tracking Clean Energy Progress 2017. Technical report, International Energy Agency.

Patil, P., Knight, T., Katiyar, A., Vanderwal, P., Scherlin, J., Rozowski, P., and Nguyen, Q. P. (2018). CO2 Foam Field Pilot Test in Sandstone Reservoir: Complete Analysis of Foam Pilot Response. *Paper presented at SPE Improved Oil Recovery Conference, Tulsa, Oklahoma, USA*. 10.2118/190312-MS.

Pham, V. and Halland, E. (2016). Perspective of CO_2 for Storage and Enhanced Oil Recovery in Norwegian North Sea. Technical report, Norwegian Petroleum Directorate.

Ren, G. and Nguyen, Q. P. (2017). Understanding aqueous foam with novel CO_2-soluble surfactants for controlling CO_2 vertical sweep in sandstone reservoirs. *Springer*.

Rocha, P. S., Riberiro, A. L. C., Menezes, P. R. F., Costa, P. U. O., Rodrigues, E. A., and Costa, G. M. N. (2006). Determination of CO_2 Minimum Miscibility Pressure using Solubility Parameter. Technical report, University of Salvador.

Rognmo, A. U., Fredriksen, S. B., Alcorn, Z. P., Sharma, M., Føyen, T., Eide, Ø., Graue, A., and Fernø, M. A. (2018). Pore-to-Core EOR Upscaling for CO_2-foam for CCUS. Paper presented at SPE EUROPEC featured at the 80th EAGE Annual Conference and Exhibition. SPE-190869-MS.

Rossen, W., Ocampo-Florez, A. A., Restrepo, A., Cifuentes, H. D., and Marin, J. (2014). Long-Time Diversion in SAG Foam Enhanced Oil Recovery From Field Data. *Paper presented at SPE Annual Technical Conference and Exhibition, Amsterdam, The Netherlands*. 10.2118/170809-MS.

Saulnier, J. B. and Varella, M. D. (2013). *Global Change, Energy Issues and Regulation Policies*. Springer Dordrecht HeildelBerg New York London.

Schlumberger (2009). *ECLIPSE Convergence*. Schlumberger.

Schlumberger (2014). *Blackoil Reservoir Simulation Training and Excercise Guide*. Schlumberger.

Schlumberger (2016). *ECLIPSE Industry-Reference Reservoir Simulator Technical Description*. Schlumberger.

Schramm, L. and Wassmuth, F. (1994). *Foams: Fundamentals and Applications in the Petroleum Industry*. American Chemical Society. 10.1021/ba-1994-0242.ch001.

Shahverdi, H., Sohrabi, M., Fatemi, M., and Jamiolahmady, M. (2011). Three-phase relative permeability and hysteresis effect during WAG process in mixed wet and low IFT systems. *SPE Journal*.

Sharma, M. (2017). East Seminole Simulation Study. Technical report, National IOR Centre of Norway at the University of Stavanger.

Sheng, J. J. (2013). *Enhanced Oil Recovery Field Case Studies*. Gulf Professional Publishing, Elsevier.

Sorbie, K. S. and Van Dijke, M. I. J. (2005). Fundamentals of Three-Phase Flow in Porous Media of Heterogeneous Wettability. Technical report, Institue of Petroleum Engineering, Heriot-Watt University, Edinburgh, Scotland, UK.

Stone, H. L. (1970). Probability model for estimating three-phase relative permeability. *SPE Journal*. 10.2118/2116-PA.

Tang, C. M. (2015). Permian Basin area, Texas, United States. *Encyclopædia Britannica, inc.* https://www.britannica.com/place/Permian-Basin.

Thiele, M., Batycky, R., and Fenwick, D. (2010). Streamline Simulation for Modern Reservoir-Engineering Workflows. *Journal of Petroleum Technology*. 10.2118/118608-MS.

Ursin, L. (2018). Ekspertintervjuet: Den kronglete karbonfangsten. *Energi og Klima*.

Zanganeh, M. N. and Rossen, W. R. (2013). Optimization of Foam Enhanced Oil Recovery: Balancing Sweep and Injectivity. *SPE Journal*, 10.2118/163109-PA.